



Kgwadi, Monageng (2017) *Low-cost antennas and systems for next generation wireless communications*. PhD thesis.

<http://theses.gla.ac.uk/8396/>

Copyright and moral rights for this work are retained by the author

A copy can be downloaded for personal non-commercial research or study, without prior permission or charge

This work cannot be reproduced or quoted extensively from without first obtaining permission in writing from the author

The content must not be changed in any way or sold commercially in any format or medium without the formal permission of the author

When referring to this work, full bibliographic details including the author, title, awarding institution and date of the thesis must be given

Enlighten:Theses
<http://theses.gla.ac.uk/>
theses@gla.ac.uk

Low-cost Antennas and Systems for Next Generation Wireless Communications



Monageng Kgwadi

School of Engineering
University of Glasgow

Submitted in fulfilment of the requirements for the degree of

Doctor of Philosophy

April, 2017

©Kgwadi, 2017

Abstract

This work presents a study of low-cost antennas and communication systems to support the burgeoning demand for bandwidth in the next generation wireless communications and networks (5G) and/or Internet of Things (IoT). The work was divided into three different fields all aimed at low-cost solutions of enabling next generation networks (5G) and IoT.

The first part of the study involves study of low-cost fabrication of antennas and radio frequency (RF) guided wave structures up to 10 GHz using the thermal transfer printing (TTP) technique on renewable, light weight, flexible and low-cost substrates. The thermal transfer printing method for electronics was characterised from DC to 10 GHz and benchmarked for performance against inkjet printing technique which is an established technique for printed electronics. TTP achieved similar or better read range to inkjet printed radio frequency identification (RFID) antennas that were used in this study. Applications of the TTP method in IoT taking advantage of its speed and low cost were demonstrated by; producing on-demand antennas and/or rapid prototyping electronic designs, using off the shelf components to build a frequency agile antenna, and an ultra wideband antenna (UWB) for low power short range communications.

The second part involves design and optimisation of a multi-port driven (MPD) slot-ring antenna for purposes of integration with resonant tunnelling diode (RTD) oscillators for millimetre-wave communications. The optimised structure managed airside radiation without the use of bulky lenses and achieved directivity of 10.8 dBi. The concept of the slot-ring with a backing ground plane was experimentally verified by a fabricated antenna for 5 GHz operation showing the expected performance.

The third part is an experimental study of modulating RTD oscillators to determine and improve achievable modulation bandwidth to meet 5G demands. Wireless transceiver systems at 28-40 GHz and 240 GHz were build using combinations of horn antennas, quasi-optical Schottky barrier diode detectors and some off-line signal processing. The modulation bandwidth of the oscillators were found to be limited to

300 Mbps and 16 Mbps for the 28-40 GHz oscillators and 220-300 GHz oscillators respectively due to oscillators being optimised for high power output instead of high modulation rates. Recommendations are made to improve the modulation data rate of these oscillators in order to meet the 5G data rate targets.

Acknowledgements

I would like to thank my supervisors Dr. Edward Wasige, Dr. Anthony Kelly and Dr. Timothy D. Drysdale for their excellent support and guidance throughout my study program making it a valuable and enjoyable experience. I would also like to thank Professor John Briggs and the Glasgow Center for International Development (GCID) for the work, financial support and affording me the opportunity to study at University of Glasgow.

I would like to thank Dr. Clement Vouch for his technical support and training with the operation of the anechoic chamber and antenna measurements. I would like to thank Mr. Francesco Mirando for microscope imaging and access to the James Watt Nanofabrication Centre instruments. I would also like to thank Dr. Afesomh Ofiare for training and technical assistance with RF measurements. I would also extend my gratitude to Dr. Scott Watson for help with experimental set ups. I will also like to thank Dr. Khalid Alharbi and Dr. Jue Wang for availing their oscillators used in this Thesis. I would also like to thank the technical services staff at the University of Glasgow electronics workshop for fabrication of antennas.

I would like to thank the collaborating team at Tampere University with RFID tags measurements and providing the inkjet tags used for benchmarking performance. I would like to thank Flexcon and IIMAK for the supply/donation of the substrates and conductive thermal transfer ribbons respectively. I would like to thank Mr. Byron Alderman and Teratech Components for loaning us the Schottky barrier diode detector used in the wireless communications experiments.

Finally I would like to thank my family and girlfriend Ms. Ciara McBride for all of their support.

Preface

The work presented in this Thesis has culminated in the following publications:

I. Peer reviewed journals:

1. **Kgwadi, M.**, Rizwan, M., Kuttty, A. A., Virkki, J., Ukkonen, L., Drysdale, T. D., “Performance Comparison of Inkjet and Thermal Transfer Printed Passive Ultra-high-frequency Radio-frequency Identification Tags’, *IET Microwaves, Antennas and Propagation*, 2016, 10, (14), p. 1507-1514, DOI: 10.1049/iet-map.2016.0331 IET Digital Library, <http://digital-library.theiet.org/content/journals/10.1049/iet-map.2016.0331>
2. **Kgwadi, M.**, and Drysdale, T.D., “Diode-switched Thermal-Transfer Printed Antenna on Flexible Substrate”, *Electronics Letters*, 2016, DOI: 10.1049/el.2015.3060 IET Digital Library, <http://digital-library.theiet.org/content/journals/10.1049/el.2015.3060>
3. M. Rizwan, A. Adhur Kuttty, **M. Kgwadi**, T. D. Drysdale, L. Sydanheimo, L. Ukkonen, J. Virkki, “Possibilities of Fabricating Copper-based RFID Tags with Photonic-sintered Inkjet Printing and Thermal Transfer Printing,” in *IEEE Antennas and Wireless Propagation Letters* , vol.PP, no.99, pp.1-1 doi: 10.1109/LAWP.2017.2682319

II. International conference proceedings:

1. **Kgwadi, M.** and T. D. Drysdale, “Characterisation of Flexible, Thermal Transfer Printed UWB Antenna Under Static Bending,” *Antennas and Propagation Conference (LAPC)*, Loughborough, 2017. *accepted for publication.*
2. **Kgwadi, M.**, Allarbi, K., Wang, J., Wasige, E.; “Slot-Ring Multiport Driven Antenna with Improved Airside Radiation for Terahertz Communications,” *European Microwave Week (EuMC)*, London, 3-7 October 2016.

3. M. Rizwan, A. A. Kutty, **M. Kgwadi**, T. D. Drysdale, L. Sydänheimo, L. Ukkonen, J.Virkki, “Characterization of Nanoparticle Inks on a Novel Polyester-Based Substrate for Manufacturing of Passive UHF RFID Tags,” *WE-A5.1A.2 IEEE APS/URSI*, June 26 July 1, Farjardo, Puerto Rico, 2016
4. M. Rizwan, A. A. Kutty, **M. Kgwadi**, T. Drysdale, L. Ukkonen and J.Virkki, “Comparitive Study of Inkjet and Thermal Printing for Fabrication of Passive UHF RFID Tags,” *10th EuCAP*, Davos, Switzerland 10-15 April 2016
5. M. Rizwan, A. A. Kutty, **M. Kgwadi**, T. Drysdale, L. Ukkonen and J.Virkki, “Reliability Study of Flexible Inkjet And Thermal Printed RFID Antennas in High Humidity Conditions,” *10th EuCAP*, Davos, Switzerland 10-15 April 2016
6. Alharbi, K.H.; Ofiare, A.; **Kgwadi, M.**; Khalid, A.; Wasige, E., “Bow-tie antenna for terahertz resonant tunnelling diode based oscillators on high dielectric constant substrate,” *in Ph.D. Research in Microelectronics and Electronics (PRIME)*, 2015 11th Conference on , vol., no., pp.168-171, June 29 2015-July 2 2015 doi: 10.1109/PRIME.2015.7251361
7. **Kgwadi, M.**; Vourch, C.J.; Harrison, D.J.; Drysdale, T.D., “On-demand printing of antennas for TV white-space communications,” *Antennas and Propagation Conference (LAPC)*, 2014 Loughborough , pp.553-556, 10-11 Nov. 2014 doi: 10.1109/LAPC.2014.6996448
8. **Kgwadi, M.** and T. D. Drysdale, “Parametric study of broadband tunable helix antenna matching,” *Antennas and Propagation Conference (LAPC)*, 2014 Loughborough , 2014, pp. 128-131. doi: 10.1109/LAPC.2014.6996337

Contents

Abstract	i
Acknowledgements	iii
Preface	iv
Contents	vi
List of Figures	ix
List of Tables	xiv
Nomenclature	xv
1 Introduction	1
1.1 Motivation	2
1.1.1 Low-cost microwave printed electronics	3
1.1.2 Millimetre-wave communications	4
1.2 Aim and scope	5
1.3 Thesis outline	6
2 Background	7
2.1 Antennas and figures of merit	7
2.1.1 Antenna definition	7
2.1.2 Key antenna figures of merit	8
2.1.3 Common antennas	14
2.1.4 Multi-port driven antennas	16
2.2 Low-cost printed antennas	21
2.2.1 Thermal transfer printing method	24
2.3 Millimetre-wave communications	26

2.4	Chapter summary	32
3	Methods	33
3.1	Antenna design and simulation tools	33
3.1.1	Finite-difference time domain method	34
3.1.2	Antenna design tools	38
3.2	Antenna fabrication	38
3.2.1	Printed antennas	39
3.2.2	Photolithography process	40
3.3	Antenna measurement tools	40
3.4	Chapter summary	42
4	Characterisation & Performance Evaluation of TTP	43
4.1	Characterisation of thermal transfer printed traces	43
4.1.1	Physical characterisation	44
4.1.2	Electrical characterisation	46
4.2	Performance Comparison with Inkjet using RFID tags	50
4.2.1	Inkjet printing	50
4.2.2	RFID antenna designs	53
4.2.3	Simulation and measurement results	54
4.3	Chapter summary	59
5	Application of TTP in IoT	61
5.1	On-demand printing of antennas	61
5.1.1	Antenna design	62
5.1.2	Simulation results and measurements	63
5.1.3	Gain improvement	65
5.2	Low-cost reconfigurable antenna on flexible substrate	66
5.2.1	Antenna design and implementation	67
5.2.2	Simulation results and measurements	69
5.3	Compact ultra-wideband antenna on flexible substrate	72
5.3.1	Compact UWB antenna design	73
5.3.2	Experimental results	73
5.4	Chapter summary	76
6	Integrated Slot-ring MPD Antenna	77
6.1	Analysis of slot-ring antenna	77

6.2	Slot-ring multiport driven antenna on electrically thick substrate	79
6.3	Air-side radiation improvement	81
6.4	Optimisation of modified slot-ring MPD	81
6.5	Experimental validation of modified slot-ring antenna	85
6.6	Chapter summary	88
7	RTD Wireless Communications Systems	90
7.1	Resonant tunnelling diode oscillators	90
7.2	Oscillator characterisation	92
7.3	Modulation bandwidth characterisation	94
7.3.1	Amplitude modulation experiments	94
7.3.2	ON-OFF keying modulation	96
7.4	Wireless communications using RTD oscillators	100
7.4.1	K-band communications	101
7.4.2	G-band communications	102
7.5	Chapter summary	105
8	Conclusions and Future Work	106
8.1	Conclusions	106
8.2	Future Work	107
8.2.1	Thermal transfer printed antennas and electronics	108
8.2.2	Integrated slot-ring antenna	111
8.2.3	High datarate millimetre-wave communications using RTD oscillators	112
	Bibliography	114

List of Figures

1.1	Possible 5G networks scenario showing the range of frequencies and their likely deployment.	2
2.1	Snapshot of electric field distribution in the near-field of a dipole antenna	8
2.2	Spherical coordinate system for defining an antennas radiation pattern	9
2.3	Half power beam width angle of an antenna	10
2.4	Typical antenna reflection coefficient	12
2.5	Propagation of a generic wave (a) and a trace of the electric field vector showing elliptical polarisation (b).	13
2.6	Half wavelength dipole antenna and its radiation pattern	15
2.7	Microstrip-fed patch antenna and its radiation pattern	15
2.8	Circular horn antenna and its radiation pattern	16
2.9	Illustration of an MPD antenna; (a) wire geometry of an 8-source MPD and (b) fabrication schematic of an 8-source MPD on silicon	17
2.10	Current distribution from one source on the spoke and ring structure.	17
2.11	Far-field electric field of an MPD as a function of g	20
2.12	A slot-ring multi-port driven antenna on silicon substrate with backside radiation	21
2.13	Applications of printed large-area electronics	22
2.14	Low cost printing techniques for electronics	23
2.15	Schematic of the thermal transfer printing process.	25
2.16	Schematic showing operation and photograph of a Zebra S4M thermal printer	26
2.17	Average sea-level millimetre-wave atmospheric attenuation	27

2.18	Simplified epitaxial structure of a resonant tunnelling diode	29
2.19	Conduction band profile of an TRD at different bias voltages and I-V curve	29
2.20	An RTD oscillator circuit showing the RTD small signal model, inductor (L) and load (R_L)	30
2.21	Antennas integrated into RTD oscillator circuits;	31
2.22	Antenna with improved airside radiation suitable for integration with RTDs	31
2.23	Power combining using two individually biased RTD oscillator circuits	32
3.1	Field position on a cubic unit cell	35
3.2	Typical antenna simulation scenario	38
3.3	NSI 2000 near-field spherical scanner antenna measurement system	41
3.4	Microwave absorber reflections at normal incidence	41
4.1	Microscope images of printed traces on THERMLfilm substrate	44
4.2	Thermal transfer printing resolution test with a copper CTTR	45
4.3	Microscope images of printed traces on THERMLfilm substrate showing the morphology of the edges	46
4.4	AFM images showing the surface roughness of thermal-transfer printed traces on THERMLfilm	46
4.5	Photographs of the fabricated CPW lines with SMA connectors.	48
4.6	Microscope images of printed traces on THERMLfilm substrate	49
4.7	Physical characteristics of inkjet printed traces. Microscope image of inkjet trace on THERMLfilm	51
4.8	Schematics of the RFID tags	53
4.9	Simulated read ranges for RFID antennas	56
4.10	Measured theoretical reading range of tag design 1 fabricated by inkjet and thermal transfer printing methods [61]	57
4.11	Measured theoretical reading range of tag design 2 fabricated by inkjet and thermal transfer printing methods [61]	58
4.12	Measured theoretical reading range of tag design 3 fabricated by inkjet and thermal transfer printing methods [61]	58

5.1	Monopole antenna geometry;(a) schematic and (b) photograph of printed antenna	63
5.2	Measured and simulated reflection coefficient of antenna	64
5.3	Polar plot of normalised measured radiation pattern in horizontal and vertical planes.	64
5.4	The initial and improved monopole antennas	65
5.5	Far-field patterns of the initial and improved monopole antennas	66
5.6	Schematic (a) and picture (b) of the fabricated reconfigurable Seirpenski antenna	68
5.7	Plots of S_{11} parameter for the (a) simulated and (b) measured antennas, for the diodes ON and OFF. With the diodes OFF, operation is at 2.4 GHz and ON at 800 MHz	69
5.8	Simulated normalised current densities in the ON and OFF states	70
5.9	Simulated and measured radiation patterns in the ON and OFF states	71
5.10	A compact ultra-wideband monopole (a) schematic (all dimensions in mm) and (b) TTP printed antennas with SMA connectors under varying degrees of mechanical bending scenarios.	73
5.11	Return losses of the printed antenna under different mechanical flexing conditions.	74
5.12	Normalised simulated and measured far-field (E-plane) radiation pattern for the compact UWB monopole under different static mechanical flexing conditions at select frequencies in the IEEE 802.15.3a band; (a) 3.0 GHz,(b) 4.5 GHz, (c) 6.0 GHz, (d) 7.5 GHz, (e) 9.0 GHz, and (f)10.5 GHz.	75
6.1	Electric field distribution of the first resonance in an annular slot-ring antenna.	78
6.2	Radiation pattern of a MPD slot-ring on an electrically thick substrate	80
6.3	MPD slot-ring with backing ground plane for improved air-side radiation	82
6.4	Simulated electric field time evolution showing the circularly polarised travelling wave within the modified slot-ring MPD at consecutive time steps	83

6.5	Simulated maximum directivity versus the size of the outer ground plane	84
6.6	Simulated normalised maximum directivity versus the size of the outer ground plane	84
6.7	Simulated front-to-back ratio versus the size of the outer ground plane	85
6.8	Input impedance versus the ground size	85
6.9	Fabricated slot ring antenna for 5 GHz operation	86
6.10	Return loss	87
6.11	Simulated and measured normalised far-field radiation pattern of the 5 GHz slot ring antenna	87
6.12	Simulated axial ratio of the slot-ring antenna at 5 GHz (a) and axial ratio as a function of frequency at boresight (b).	88
7.1	Oscillator topology 1 microscope picture oscillator and circuit schematic including the bias network and load.	91
7.2	Oscillator topology 2 microscope picture oscillator and circuit schematic including the bias network and load.	92
7.3	Frequency of oscillation and output power as a function of bias voltage for the 43 GHz oscillator.	93
7.4	Frequency of oscillation and output power as a function of bias voltage for the 238 GHz oscillator.	94
7.5	Amplitude modulation of a voltage-controlled oscillator.	95
7.6	Experiment set up for modulation bandwidth determination.	95
7.7	Frequency domain output (a) mixed signal showing carrier at 43 GHz oscillator and sidebands and (b) sideband separation from carrier as a function of modulation frequency.	96
7.8	Modulation bandwidth of 43 GHz oscillator.	96
7.9	ON/OFF keying of an RTD oscillator.	97
7.10	OOK modulated signal from the 33 GHz oscillator (a) and the demodulated baseband signal (b) at 100 Mbps.	98
7.11	Bit transitions of the oscillator during On/Off Keying	99
7.12	Eye diagrams of the recovered data at select frequencies	100
7.13	Modulation bandwidth experiment using a Schottky barrier diode detector.	101

7.14	Demodulated baseband eye diagrams at selected datarates (a) 2 Mbps, (b) 8 Mbps (c) 10 Mbps, and (d) 15 Mbps.	101
7.15	OOK modulation experimental set up for the 33 GHz oscillator	102
7.16	Eye diagrams of the demodulated baseband signal trans- mitted wireless at 33 GHz	103
7.17	Schematic of air 240 GHz communications experimental set up using a quasi-optical Schottky barrier diode detector	103
7.18	Air 240 GHz communications experimental set up using a quasi-optical Schottky barrier diode detector	104
7.19	Eye diagrams of the low-pass filtered quasi-optical SBD detector output at selected datarates	104
8.1	Multi-layer and double sided printing; (a) sheet resistance improvement from multilayer thermal transfer printing and (b) misalignment of successive prints	109
8.2	Multilayer and double-sided thermal transfer printing in a high volume roll-to-roll manufacturing scenario	110
8.3	Integrated slot-ring antenna with four individually biased and mutually locking oscillators	111
8.4	Expected modulation bandwidth limits for topology 1 ocsillators	113
8.5	Phase noise of 43 GHz oscillator in free running and locked conditions	113

List of Tables

3.1	Metallograph ribbon : key parameters	39
3.2	Zebra S4M printer settings for THERLfilm	39
4.1	Inkjet Printing Key Parameters [61].	51
4.2	Key physical and DC characteristics of inkjet and TTP	52
4.3	Measured Theoretical Read Range	59
7.1	Summary of RTD oscillators key circuit components.	92

Nomenclature

Acronyms

5G	Fifth generation of mobile networks
AFM	Atomic force microscope
AM	Amplitude modulation
AUT	Antenna under test
ANSI	American national standards institute
CPW	Co-planar waveguide
CTTR	Conductive thermal transfer ribbon
DC	Direct current
FEM	Finite element method
FDTD	Finite difference time domain
FPGA	Field programmable gate array
HAN	Home area network
IEEE	Institute of electrical and electronics engineers
IET	Institution of Engineering and Technology
IIMAK	International Imaging materials Inc.
IoT	Internet of things
ISM	Industrial, scientific and medical
ITU	International telecommunications union
LAE	Large-area electronics
LMDS	Local multipoint distribution systems
LOS	Line-of-sight
M2M	Machine to machine
MMIC	Monolithic microwave integrated circuits
mmWave (mmW)	Millimetre wave
MOM	Method of moments

MPD	Multi-port driven
NDR	Negative differential resistance
NF2FF	Nearfield to farfield
NRZ	Non-return to zero
NSI	Nearfield Systems Inc.
OOK	On/Off keying
PCB	Printed circuit board
PML	Perfectly matched layer
PRBS	Pseudo random bit sequence
RF	Radio frequency
RFID	Radio frequency identification
RMS	Root-mean square
RTD	Resonant tunnelling diode
SBD	Schottky barrier diode
SLOT	Short load open through
SMA	Sub-miniature version A
THz	Terahertz
TTP	Thermal transfer printing
TVWS	Television white spaces
UHF	Ultra-high frequency
UWB	Ultra wideband
VCO	Voltage-controlled oscillator
VDI	Virginia Diodes Inc.
VNA	Vectored network analyzer
WLAN	Wireless local area network
WPAN	Wireless personal area network

Symbols

c	Speed of light in vacuum
ϵ_r	Relative dielectric constant
Γ	Reflection coefficient
η	Efficiency
InP	Indium phosphide
\square	Square

Chapter 1

Introduction

Envisaged as the next evolutionary stage of the Internet, the Internet of Things (IoT) will consist of an estimated tens of billions communicating devices operating in diverse applications including but not limited to; health care, smart cities, personal area networks, smart homes, supply chain management, and smart grids [1–4]. It is estimated that the IoT will be a US\$ 1.3 trillion business for mobile network providers by 2020 [4] and is expected to be accommodated in the next generation of mobile networks (commonly known as fifth generation or 5G). The dominating demands for 5G networks are high capacity, low latency and highly mobile data communications which need to be met before 2020 when 5G is expected to be at deployment phase. The current unlicensed communications bands like the industrial, scientific and medical (ISM) radio bands are already experiencing over-subscription due to the large number of users and devices [5–7]. Meanwhile the current licensed mobile communications bands are limited in bandwidth and cannot accommodate the increasing subscribers/devices and the high datarates envisaged (tens of gigabit per second) for 5G. Although there are efforts to improve spectral efficiency in the current ISM bands to accommodate more users [8,9], it is reasonable to expect the problem to be further exacerbated by ubiquitous computing and IoT [10] with wireless communication demands anticipated to increase up to 1000 times by 2020 [11]. Thus, to accommodate the expected large number of devices and the envisaged datarates for the IoT and 5G, alternative communication channels are being explored.

A number of candidates have been identified to accommodate the next generation of communication devices. Figure 1.1 illustrates a possible 5G frequency deployment scenario showing the use of the radio spectrum from low frequencies (300 MHz) in the left all the way to high frequencies (300 GHz) to the right of the figure. In

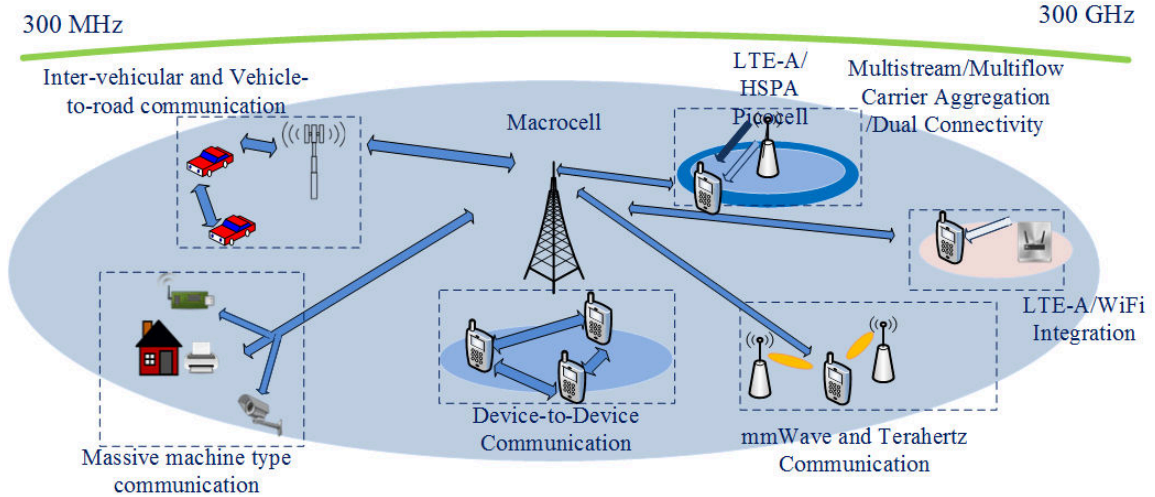


Figure 1.1: Possible 5G networks scenario showing the range of frequencies and their likely deployment [12].

particular, the migration of television broadcasting to digital terrestrial broadcast has freed up some spectrum in Ultra-High Frequency (UHF) band ideal for radio frequency identification (RFID) which is expected to contribute significant number of devices in IoT in a wide range of applications. Opportunistic use of the bands between television channels known as TV white space (TVWS) have been investigated for use in IoT applications where co-existence with incumbent licensed users is proposed [13]. The millimetre-wave (30-300 GHz) band has also been investigated for short-range communication [14] and pico-cell services [15] and put forward as a candidate to accommodate high capacity and high datarate communications commensurate with the 5G demands. Above 300 GHz, the submillimetre-wave (300 GHz -3 THz) band is largely unregulated and ideal for short range high data-rate communications and has received a lot of attention by both industry and academia to develop terahertz and sub-terahertz communications [16, 17] and imaging.

1.1 Motivation

Pervasive adoption of IoT will be dependant on low unit cost for each device [18], as such, low-cost solutions are attractive. Planar antennas are attractive because their low profile and low weight make them easy to integrate unobtrusively into compact user electronics such as tablets, wearable electronics, etc. Moreover, their compatibility with monolithic microwave integrated circuits (MMIC) makes them attractive and potentially cheaper to develop communications systems and subsystems in very

large scale integration (VLSI) or application specific integrated circuits (ASICs). This thesis presents a study of low cost planar antennas and communication systems for use in the next generation communicating devices.

1.1.1 Low-cost microwave printed electronics

In order to keep the unit costs of IoT devices there has been a drive to develop low-cost, flexible and lightweight electronics. This has led to high interest in low-cost manufacturing of electronics by both academia and industry [2, 3, 19] to support/enable pervasive computing and IoT applications. As a result, a number of inexpensive techniques for printing electronics have recently been a subject of research. Such methods focus on additive manufacturing of electronics on cheap and renewable substrates [20] as opposed to subtractive methods on semiconductor substrates. In so doing, material waste and the use of environmentally harmful chemicals are minimised, further reducing the cost of production and negative environmental impact. Rapid, large scale production of electronics is also desirable to produce vast numbers of devices for IoT. Hence roll-to-roll compatibility of these methods is important to allow large scale and rapid manufacture of electronics. These low-cost electronics fabrication methods include methods such as inkjet printing (e.g. of antennas [21], frequency selective surfaces [22], UHF passive components [23, 24], sensors and circuits [25]), gravure printing (e.g. transistors [26], and high resolution interconnects [27]), and screen printing (e.g. of electronic circuits [28] and passive sensors [29]). These techniques are well known and widely used approaches to depositing inks containing conductive particles or flakes typically metallic (or carbon nanotubes [30]), which then requires sintering to achieve the maximum conductivity.

Newer developments from time to time emerge, potentially offering improved processing methods that are faster, more convenient and lower costs. Such a development is the introduction of metal ribbons for thermal transfer printing (TTP). TTP is a roll-to-roll compatible printing method that offers low-cost and fast printing of metallic traces. TTP traces unlike inkjet and screen printing does not require a sintering step therefore avoiding costs associated with acquiring and operating sintering facilities. TTP achieves print speeds of up to 20 cm/s and since there is no waiting time associated with sintering, TTP allows on-demand and rapid manufacture and/or prototyping of electronics. In this thesis, the TTP method is studied as a viable alternative to the established printing techniques of electronics for IoT applications. The

TTP method is characterised and benchmarked against inkjet printing which is an established and pervasive printing method for electronics. Then, applications of the TTP method for manufacturing of electronics in the IoT are also studied exploiting its advantages.

1.1.2 Millimetre-wave communications

The millimetre and submillimetre-wave bands have largely unregulated spectrum that can be used for short-range high data-rate communications [31]. At these frequencies, electromagnetic waves have short propagation distances due to atmospheric attenuation [32]. This property makes the millimeter wave band particularly attractive for short-range communications allowing for frequency re-use and thus accommodating large number of users/devices meeting the high capacity requirements for 5G networks. Pico cells and home area networks (HAN) have been shown to have the potential of up to 70% cost reductions for operators [33]. However, there are some technical obstacles that need to be overcome to realise millimeter wave communications including the development standards, building transceiver systems, developing compact millimetre-wave radio sources and efficient millimetre-wave antennas [34] among others. Therefore, a lot of work is currently being done by both industry and academia to develop millimetre and sub-millimetre wave communications and it remains an area of active research [16, 17, 35, 36].

Resonant tunnelling diodes (RTDs) have been demonstrated to work as compact sources at room temperatures in the terahertz and millimetre wave bands [37, 38]. RTDs therefore have the potential to make millimetre-wave communications feasible with compact sources that can be integrated into consumer electronics, addressing the problem of lack of millimetre-wave and terahertz sources. However, the low power output of RTD-based oscillators (<1 mW) necessitates efficient and directive antennas to achieve communication over reasonable communication distances (tens of metres) to compensate for the high atmospheric attenuation. Planar antennas are usually favoured because of their relative ease of manufacture and integration with monolithic microwave integrated circuit (MMIC) processes. However, at the millimeter-wave frequencies they suffer from low efficiency due to the excitation of substrate modes as the substrate gets electrically large [39]. In most cases the thickness of the substrates can not be made thin due to manufacturing process and packaging constraints. Therefore there is a need to develop efficient antennas for integration with

RTDs to realise millimetre-wave communications. In this thesis, a multi-port driven slot-ring antenna is investigated for integration with RTD oscillators. The main objective being to work towards developing a transceiver system in the millimetre-wave bands for short range, high data-rate communications. In particular, the slot-ring multi-port driven antenna is studied for the purposes of integration with RTD oscillators.

RTD oscillators that have been developed and optimised for high radio frequency (RF) output are studied for millimetre-wave communications. These oscillators have the potential to support high data rates wireless communications that can meet the 5G targets (approximately several tens of gigabit per second data rates). In this Thesis such oscillators are characterised for modulation bandwidth, determining the limiting factors and developing solutions to maximise the achievable data rates. Wireless communication systems are built for the lower band (30 GHz) and upper band (300 GHz) of the millimetre-wave band.

1.2 Aim and scope

The aim of this Thesis is to realise low cost communication solutions to enable IoT devices to communicate. The main objectives are;

1. Demonstrate the thermal transfer printing method as a viable electronics fabrication method for IoT devices on renewable substrates up to 10 GHz,
2. Characterise and benchmark the performance of the thermal transfer printing method to inkjet printing, which is an established method of printing electronics,
3. Study and optimise the multi-port driven slot-ring antenna for purposes of integration with resonant tunnelling diode oscillators with emphasis on airside radiation,
4. Characterise and determine the modulation bandwidth of the high power resonant tunnelling diode oscillators to improve the achievable data transmission rates towards 5G targets.
5. Build wireless transceiver systems in the millimetre-wave band using RTD oscillators for ubiquitous communications applications.

1.3 Thesis outline

This Thesis is organised as follows, Chapter 2 provides the background on antennas, their key figures of merit important for design and performance evaluation. Common antenna types are also discussed along with typical application scenarios. Multi-port driven antennas are introduced as well as a slot-ring antenna which is studied subsequently for integration with RTD oscillator. Low cost printing techniques for large area electronics and antennas are also presented including the thermal transfer printing method. Millimetre-wave communications are discussed as an enabler for 5G networks. Chapter 3 presents the methods, tools and equipment used throughout this Thesis highlighting their benefits and limitations. In Chapter 4, the thermal transfer printing method is characterised and benchmarked to incumbent printing techniques for low-cost printed electronics. Applications of the thermal transfer printing method in the IoT is demonstrated in Chapter 5 exploiting the advantages of the technology. Chapter 6 presents a study and optimisation of a slot-ring multi-port driven antenna for the purposes of integration with resonant tunnelling diode oscillators and experimental verification. Chapter 7 presents experimental studies of direct modulation of resonant tunnelling diode oscillators for wireless data communications with the purpose of improving the achievable data rates to meet 5G targets. Wireless communications systems at 30 GHz and 300 GHz are built demonstrating the feasibility of using RTD oscillators as an enabling technology for ubiquitous communications for 5G. Conclusions and future work are finally discussed in Chapter 8.

Chapter 2

Background

This Chapter provides background on antennas, their operation and key performance metrics used to evaluate antennas in this Thesis. Common antenna types and applications are discussed as well including a multi-port driven slot-ring antenna. Low cost printing methods commonly used for large-area electronics are discussed together with the thermal transfer printing method which is a new technique for producing printed electronics. Millimetre-wave and resonant tunnelling diode based communications are also discussed subsequently including the antenna design for millimetre wave antenna design. Chapter conclusions are then subsequently drawn.

2.1 Antennas and figures of merit

This Section provides the definition for antennas and their key figures of merit commonly used for design and performance evaluation. The theory of operating mechanism of multi-port driven ring and its complementary structure of slot-ring are also discussed.

2.1.1 Antenna definition

An antenna is defined as a component designed to receive or radiate electromagnetic waves by the Institute of electrical and electronics engineers' (IEEE) terms of definition [40]. Antennas are therefore interfaces for sending and receiving wireless signals and as such, critical components in wireless communication systems. Radiation in antennas is achieved by acceleration (or deceleration) of charge [41]. Figure 2.1 shows a snapshot of the electric field distribution around an ideal half-wavelength dipole. On

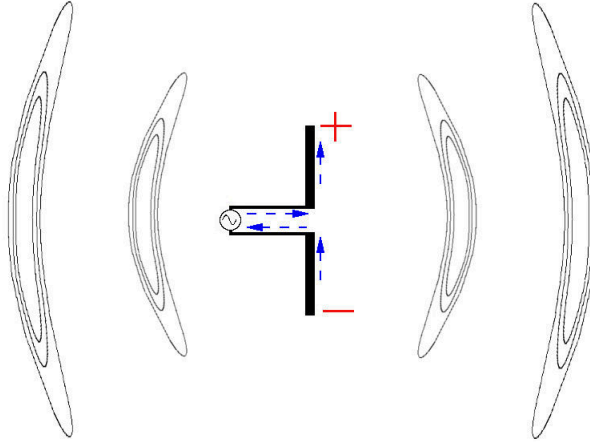


Figure 2.1: Snapshot of electric field distribution in the near-field of a dipole antenna

a peak positive cycle, an accumulation of charge occurs on the upper half of the dipole inducing an instantaneous positive charge. The lower half meanwhile experiences a deficit of charge resulting in an instantaneous negative charge. The instantaneous current is also shown by the dotted arrows along the dipole. The time-varying source creates an oscillation of charge back and fourth between the two halves of the dipole that results in the radiation as shown in Figure 2.1. An antenna has two regions of interest, the near-field and the far-field regions. The area within a distance $d < \frac{2D^2}{\lambda}$ of an antenna forms the near-field (Fresnel region) with λ as the wavelength and D as the radius of a sphere that encloses the antenna determined by the physical size of the antenna. In the near-field region the radiation pattern is dependant on the distance from the antenna whereas the radiation pattern is independent of the distance from the antenna in far-field region. The antennas studied in this Thesis are designed to operate in the far-field region, therefore only the far-field characteristics are discussed.

2.1.2 Key antenna figures of merit

The following are the most common figures of merit used to specify designs and evaluate antenna performance.

Radiation pattern

The far-field radiation pattern of an antenna gives the spatial distribution of the radiated electromagnetic energy by the antenna. It is represented by the relative intensity measured along the azimuth (ϕ) and elevation (θ) angles around the antenna

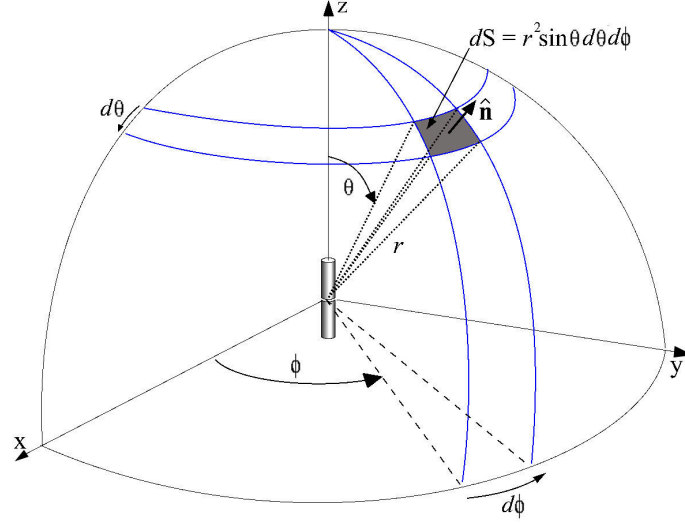


Figure 2.2: Spherical coordinate system for defining an antenna's radiation pattern

under test (AUT) as shown in Figure 2.2. Spherical coordinates as shown in Figure 2.2 are commonly used to formulate and describe antenna radiation characteristics. A complete representation of radiation patterns is a volumetric measurement of intensity on a surface of a sphere, often normalised to the highest intensity. A more concise representation of the radiation pattern is often given as the spatial distribution of energy along special values of azimuth and elevation angles known as the E-plane and H-plane. For linearly polarised antennas as the dipole in Figure 2.2, the electric field is along the z-axis and thus the z-x plane is referred to as the E-plane at $\phi = 0^\circ$. The magnetic field is orthogonal to the electric field and thus the x-y plane is known as the H-field at $\theta = 90^\circ$. The E-plane and H-plane are often enough to give a good overview of the radiation pattern of an antenna and thus used to describe radiation patterns in the rest of this Thesis.

Directivity

The radiation intensity $I(\phi, \theta)$ is defined as the power radiated by an antenna per unit solid angle $d\Omega = r^2 \sin\theta d\theta d\phi$ on a surface at a distance r from the antenna. The average intensity I_{ave} is the total power intensity averaged in all directions (ideal isotropic antenna) given by;

$$I_{ave} = \frac{\int_0^{2\pi} \int_0^\pi I(\phi, \theta) d\Omega}{4\pi} \quad (2.1)$$

The directivity of an antenna is then defined as the ratio of the radiation intensity in a given direction to that of an ideal omnidirectional antenna.

$$D(\phi, \theta) = \frac{I(\phi, \theta)}{I_{ave}}, \quad (2.2)$$

where $I(\phi, \theta)$ is the radiation intensity in a particular (ϕ, θ) direction. It is common to state the maximum directivity value at a particular direction for brevity. Antenna directivity is typically reported with reference to an ideal isotropic antenna denoted dBi and gives a measure of how directional an antenna is. An omnidirectional antenna will have a directivity of 0 dBi, and highly directive antenna will have high value (up to 40 dBi) of directivity.

Half power beam width

The half power beam width (HPBW) gives the angle at which power intensity drops to half of the maximum intensity as shown in Figure 2.3. The maximum directivity stated along with the half power beam width is often used to describe the radiation pattern since it gives in a concise manner the distribution of the radiated power in the far field. A narrow HPBW angle denotes a directional antenna, while a wider angle signifies an non-directional antenna. A value of 360° denotes an omnidirectional antenna.

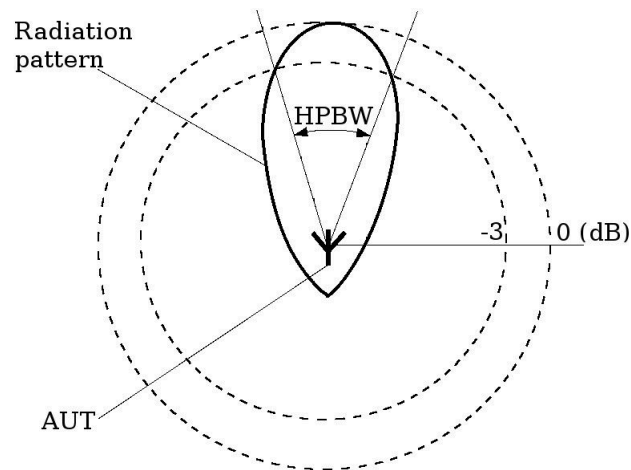


Figure 2.3: Half power beam width angle of an antenna

Gain

The gain of an antenna is the directivity adjusted for losses. That is;

$$G(\phi, \theta) = \eta D(\phi, \theta), \quad (2.3)$$

where D is the directivity and η is the efficiency. Antenna gain is typically reported with reference to an ideal isotropic antenna denoted dBi.

Efficiency

The radiation efficiency of an antenna is the ratio of the radiated power to the total power supplied to the antenna. That is;

$$\eta = \frac{P_{rad}}{P_{tot}} = \frac{P_{rad}}{P_{rad} + P_{loss}} \quad (2.4)$$

where P_{rad} is the radiated power, P_{tot} is the total power supplied, and P_{loss} is the total power losses due to; mismatch between antenna and transmission line, and material losses (e.g. metal, dielectric).

Return Loss/Reflection Coefficient

The return loss (RL) of an antenna gives a measure of losses that arise from impedance mismatch between the transmission line and the antenna. It is expressed as a ratio of the incident power to the reflected power in decibels (dB) by;

$$RL = 10 \log_{10} \left(\frac{P_i}{P_r} \right), \quad (2.5)$$

where P_i and P_r are the incident power and reflected power respectively. For maximum power transfer, the transmission line impedance and the antenna input impedance should be equal, which results zero insertion losses. In some texts the return loss is expressed as reflection coefficient (Γ) or s_{11} which is given by;

$$\Gamma = \frac{Z_L - Z_o}{Z_L + Z_o} \quad (2.6)$$

where Z_L is the impedance of the antenna and Z_o is the impedance of the transmission line. The return loss and reflection coefficient are related by;

$$RL = -20 \log_{10} (|\Gamma|) \quad (2.7)$$

Ideally the return loss have to be as small as possible at the desired frequency. This is often achieved by the use of matching networks between the transmission line and antenna. For practical purposes, the acceptable level of the reflected power is at most a tenth of the incident power (-10 dB).

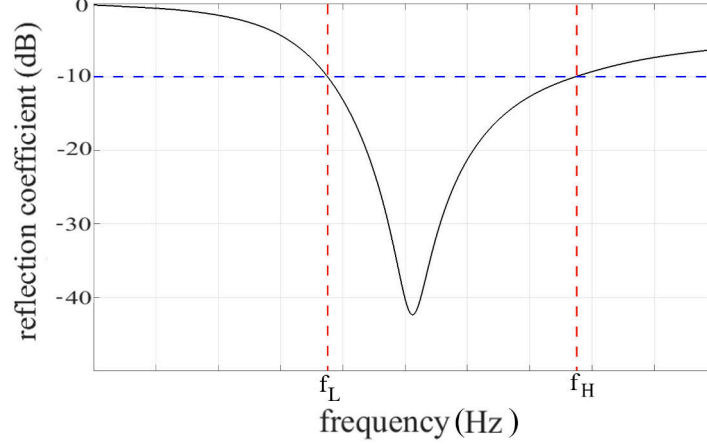


Figure 2.4: Typical antenna reflection coefficient

Impedance bandwidth

The impedance bandwidth of an antenna gives the range of frequencies over which an antenna efficiently radiates. It is normally expressed as the range of frequencies that an antenna has lower than -10 dB return losses as shown in Figure 2.4. Fractional bandwidth is another parameter that gives a measure of the bandwidth of an antenna and is given by;

$$BW(\%) = \frac{f_H - f_L}{f_H + f_L} \times 200 \quad (2.8)$$

A higher value of fractional bandwidth signifies wideband operation while a small value means the antenna is narrowband. Antennas with a fractional bandwidth higher than 20% are commonly referred to as ultra-wideband (UWB) [42].

Polarisation

Polarisation characterises the time-varying magnitude and orientation of the electric field of an electro-magnetic wave as it propagates in space. The instantaneous electric field of an electro-magnetic wave propagating in the z direction can be represented by;

$$E(z, t) = E_x \cos(\omega t + kz + \phi_x) \hat{\mathbf{u}}_x + E_y \cos(\omega t + kz + \phi_y) \hat{\mathbf{u}}_y \quad (2.9)$$

where E_x and E_y are the maximum magnitudes of the x and y components respectively, k is the phase constant, ω is the angular velocity and ϕ_x and ϕ_y are the phase delay in x and y directions respectively.

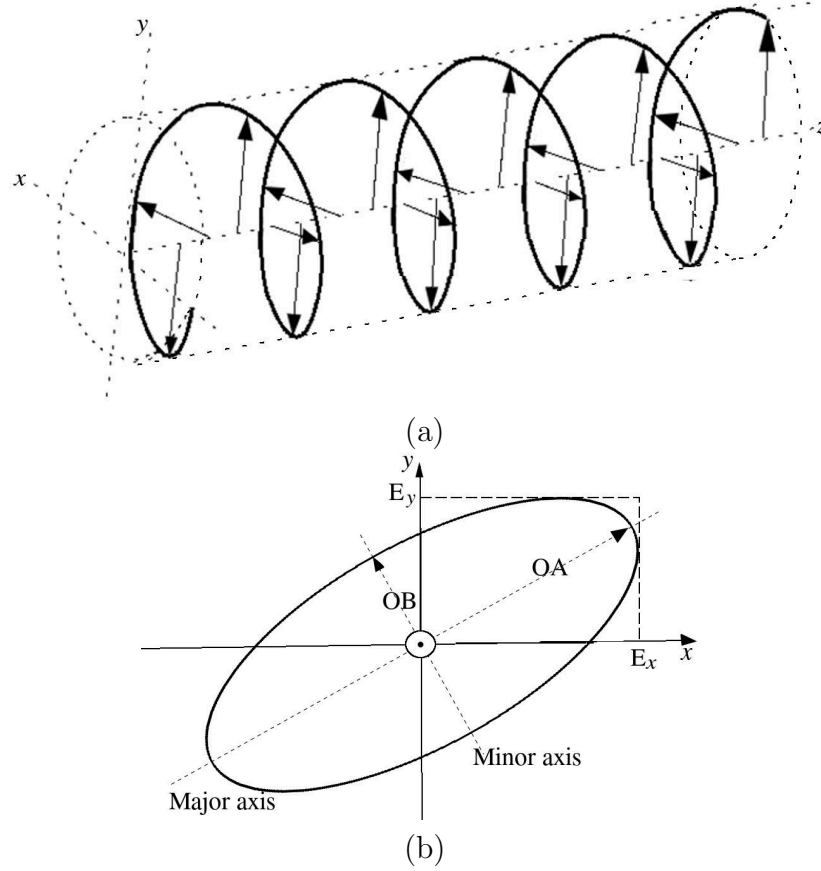


Figure 2.5: Propagation of a generic wave (a) and a trace of the electric field vector showing elliptical polarisation (b).

Figure 2.5(a) shows the propagation of a generic wave described by Equation 2.9 with non-zero E_x and E_y . A vectorial representation of an electric field described by Equation 2.9 with non-zero E_x and E_y in space in general terms traces out an ellipse on the plane perpendicular to the direction of travel as shown in Figure 2.5(b) as the wave propagates in the z direction. In particular, the trace is elliptical when two conditions are met; when the phase difference between the x and y components is an odd multiple of $\pi/2$ and the magnitudes are not equal or when the phase difference of the two components is not a multiple of $\pi/2$ irrespective of their magnitudes.

For the case $E_x \neq 0$ and $E_y \neq 0$ and the phase difference between the x and y components equals an integer multiple of π i.e.;

$$\Delta\phi = \phi_x - \phi_y = n\pi, \quad n = 0, 1, 2, 3, \dots \quad (2.10)$$

the vector traces a line in the x - y plane and the wave is said to have linear polarisation. If either $E_x = 0$ or $E_y = 0$, the wave will also have linear polarisation. An antenna that radiates a linearly polarised wave is also said to be linearly polarised.

If the phase difference between the x and y components equals $\pi/2$ and the $E_x = E_y$ the vector traces a circle and the wave is said to have circular polarisation. An antenna that radiates a circularly polarised wave is thus said to be circularly polarised. Circular polarisation is thus a special case for elliptical polarisation.

Axial ratio (AR) is a parameter that describes the ratio of the main axis to the minor axis of the ellipse traced by the electric field vector shown in Figure 2.5(b). The axial ratio in decibels is given by;

$$AR_{dB} = 20 \log_{10} \left(\frac{AB}{OB} \right) \quad (2.11)$$

For a circular polarised wave, the axial ratio is 0 dB for linearly polarised waves the axial ratio is infinite. The axial ratio of circularly polarised antennas is usually reported as a function of frequency or elevation angle to describe the variation of the polarisation with frequency or direction.

A circularly polarised wave can rotate in a clockwise or counter-clockwise direction. A wave that rotate in clockwise direction is said to have right hand circular polarisation (RHCP) while one that rotates in the counter-clockwise direction is said to have left hand circular polarisation (LHCP).

2.1.3 Common antennas

Antennas can be categorised by the mechanism they achieve radiation (i.e. resonant or travelling wave), their construction (i.e. wire, planar or aperture) or radiation characteristics (i.e. omnidirectional or directive). An exhaustive description of antennas is beyond the scope of this Thesis and can be found in antenna design handbooks [41]. Some common antennas are discussed subsequently along with typical applications.

Dipole antenna

A dipole antenna is simple wire antenna constructed by two quarter-wavelength wires placed end-to-end with an excitation source placed between them as shown in Figure 2.1. The radiation pattern of a dipole is omnidirectional and makes it ideal for applications where the location of the communicating devices is unknown or not fixed for example mobile ad-hoc networks. The gain of a dipole made of an ideal conductor is 2.15 dBi, and is often used as a reference for antenna gain (dBd) instead of an isotropic antenna (dBi). The gain relative to a dipole and isotropic antenna are

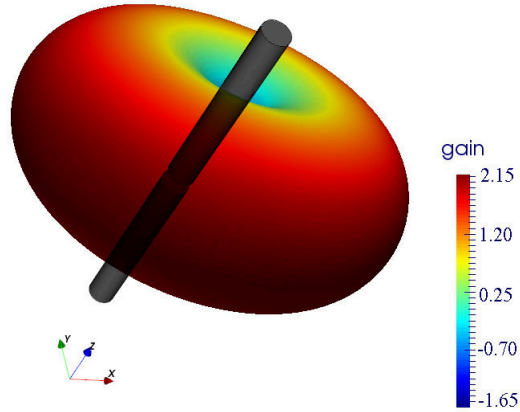


Figure 2.6: Half wavelength dipole antenna and its radiation pattern

related by $G_{dBd} = G_{dBi} - 2.15$.

Patch antenna

A patch antenna is an example of a low-profile antenna formed by a rectangular metal patch printed on top of a dielectric with a backing ground plane as shown in Figure 2.7. The dimensions of the patch determine the resonant frequency and the width of the patch is a half-wavelength of the design frequency. Patch antenna are omnidirectional with a gain of around 6 dBi and commonly used in mobile communications where the transmitter and receiver relative positions are not known and can change over time.

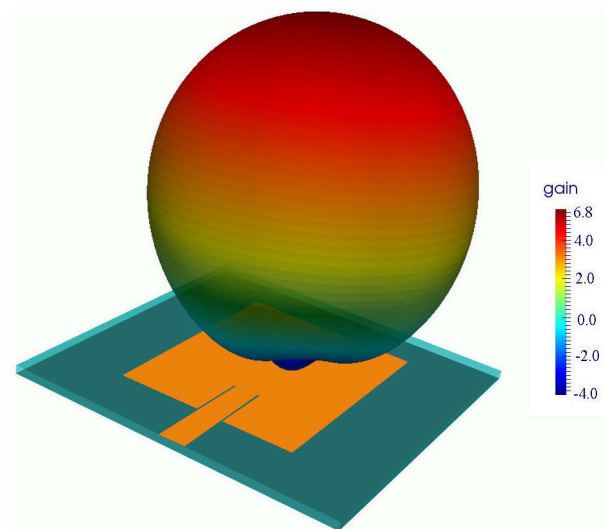


Figure 2.7: Microstrip-fed patch antenna and its radiation pattern

Horn antennas

A horn antenna is an example of a travelling wave formed by flared ends of a waveguide to form a gradual transition from waveguide to air as shown in Figure 2.8. Horn antennas are highly directional and have gains up to 30 dBi. They are ideal for applications where the position of the transmitter and receiver are known and fixed.

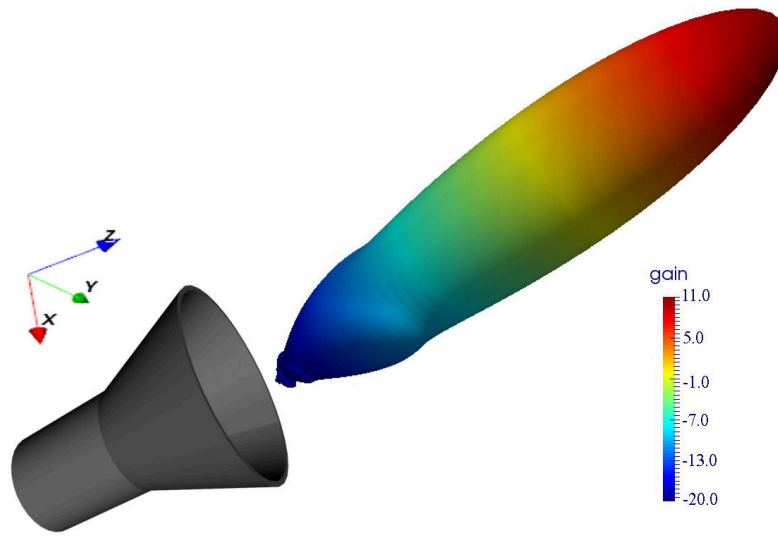


Figure 2.8: Circular horn antenna and its radiation pattern

2.1.4 Multi-port driven antennas

Multi-port driven (MPD) radiators offer the possibility to obtain high radiation efficiency even with low input impedance antennas and power combining by the antenna [43]. The integration of sources and the antenna reduces losses associated with transmission lines and impedance matching networks which at millimetre and sub-millimetre bands are significant. An eight source multi-port driven radiator designed for 155 GHz operation implemented using a conductor ring with a wheel and spoke geometry on a quarter-wavelength thick silicon substrate with a reported gain of 4.4 dBi, 9.71 dBi maximum directivity and 30% efficiency was described in [43].

An eight source wheel and spoke MPD radiator is shown in Figure 2.9(a). Each of the driving ports is a controlled phase current source with a value I_s . Two assumptions are required for analysis; 1) the current distribution on a wire terminated by a short circuit has a sinusoid distribution and 2) there is no coupling between the

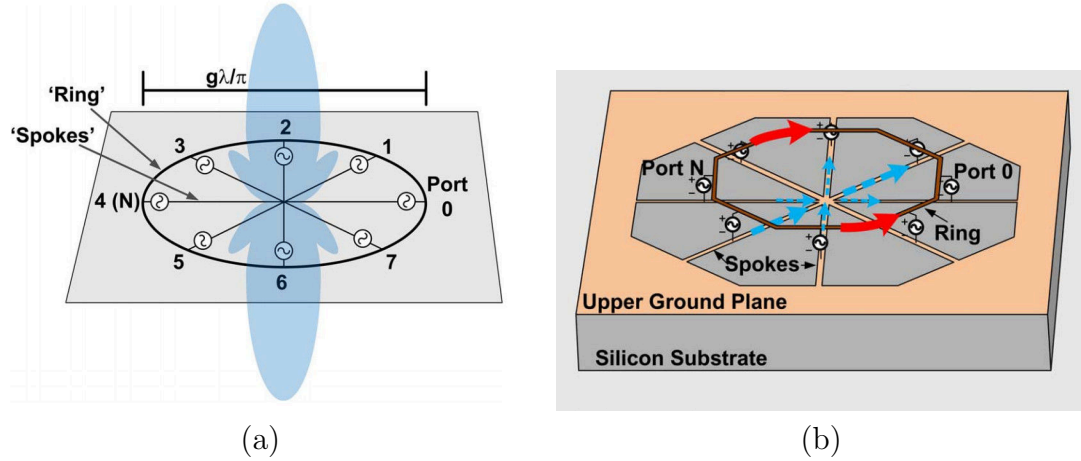


Figure 2.9: Illustration of an MPD antenna; (a) wire geometry of an 8-source MPD and (b) fabrication schematic of an 8-source MPD on silicon [43].

ring and spokes or between the individual spokes. Analysis of the structure using the superposition theorem considers the ring and the spokes separately. When a current I_s is injected at port 0 it splits in two and propagates along the two halves of the ring towards port 4. A standing wave is generated along the ring with current maximums at $\phi = \pi/2$ and $\phi = 3\pi/2$ due to the differential symmetry of the structure as shown in Figure 2.10. The far-field electric field can be calculated from the current distribution along the structure.

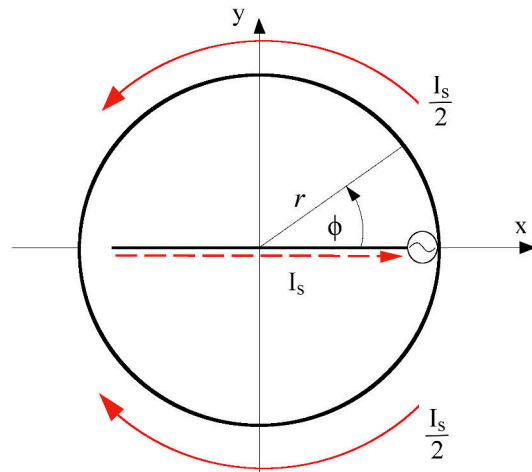


Figure 2.10: Current distribution from one source on the spoke and ring structure.

Due to the symmetry of the structure, the y-component of the current along ring cancels out. Only the x-component of the current on the ring that add coherently and contribute to the far-field electric field. To get the far-field electrical field, it

is only necessary to integrate the x-component of the current in one quadrant and multiply it by 4 due to the two planes of symmetry. The current distribution along the quarter of the ring is a sinusoid with the maximum occurring at $\phi = \pi/2$ and can be expressed as:

$$I_q = I_{max} \cos(\beta l) \quad (2.12)$$

Where I_{max} is the maximum current that appears at $\phi = \pi/2$, $\beta = 2\pi/\lambda$ is the propagation constant and $l = r(\pi/2 - \phi)$ is the length of wire from $\phi = \pi/2$ where I_{max} occurs. Define a parameter $g = 2\pi r/\lambda$ as the ratio of the circumference of the ring to the wavelength where r is the radius of the ring. Thus $l = (\pi/2 - \phi)g\lambda/(2\pi)$ and the current along the quarter length can be expressed as:

$$I_q = I_{max} \cos[g(\pi/2 - \phi)] \quad (2.13)$$

The x-component of the current I_{q_x} is given by:

$$I_{q_x} = -I_{max} \cos(g\phi') \cos(\phi') \hat{\mathbf{u}}_x \quad (2.14)$$

where $\phi' = (\pi/2 - \phi)$.

The far-field electric field due to currents on a plane perpendicular to a point of observation at a distance R_o is given by [41]:

$$\mathbf{E} = \frac{-j\omega\mu}{4\pi} \frac{e^{-jkR_o}}{R_o} \int_C \mathbf{I} dl \quad (2.15)$$

where $k = \omega\sqrt{\mu\epsilon}$, with ω as the angular frequency of the time harmonic signal, while μ and ϵ are the permeability and permittivity of the medium respectively. Substituting 2.14 into 2.15, the far-field electric field due to the currents on one quarter of the ring can be expressed as:

$$\mathbf{E}_x = -I_{max} \frac{jcg\mu}{8\pi^2} \frac{e^{-jkR_o}}{R_o} \int_0^{\pi/2} \cos(g\phi') \cos(\phi') d\phi' \hat{\mathbf{u}}_x \quad (2.16)$$

Using equation (2.11) and equating $I_q = I_s/2$ at $\phi = 0$ (i.e. $I_{max} = \frac{I_s}{2\cos(g\pi/2)}$), the solution to the integral 2.16 is:

$$\mathbf{E}_x = -I_s \frac{jc\mu}{16\pi^2} \frac{e^{-jkR_o}}{R_o} \frac{g}{g^2 - 1} \hat{\mathbf{u}}_x \quad (2.17)$$

Thus the total electric field due to the four quadrants of the ring is therefore;

$$\mathbf{E}_x^r = 4\mathbf{E}_x = -I_s \frac{jc\mu e^{-jkR_o}}{4\pi^2} \frac{g}{R_o} \frac{1}{g^2 - 1} \hat{\mathbf{u}}_x \quad (2.18)$$

Similarly, the far-field electric field contribution of the currents on the spoke can be determined. The current distribution on the spoke is assumed to be sinusoidal with a maximum at the center and zero at the floating end. Thus the current along the spoke can I_{sp} can be expressed as;

$$I_{sp} = I_{max}^s \cos\left(\frac{2\pi}{\lambda} x\right) \hat{\mathbf{u}}_x \quad (2.19)$$

$$\mathbf{E}_x^s = \frac{-j\omega\mu e^{-jkR_o}}{4\pi} \frac{1}{R_o} \int_{-\frac{g\lambda}{2\pi}}^{\frac{g\lambda}{2\pi}} I_{max}^s \cos\left(\frac{2\pi}{\lambda} x\right) dx \hat{\mathbf{u}}_x \quad (2.20)$$

The solution to the integral is then:

$$\mathbf{E}_x^s = -I_{max}^s \frac{jc\mu e^{-jkR_o}}{4\pi^2} \frac{1}{R_o} \sin(g) \hat{\mathbf{u}}_x \quad (2.21)$$

At $x = r$ the current along the spoke is equal to the current injected by the source I_s , thus 2.19 can be rearranged as,

$$I_{max}^s = \frac{I_s}{\cos\left(\frac{2\pi r}{\lambda}\right)} = \frac{I_s}{\cos(g)} \quad (2.22)$$

Substituting back into 2.21 yields

$$\mathbf{E}_x^s = -I_s \frac{jc\mu e^{-jkR_o}}{4\pi^2} \frac{1}{R_o} \tan(g) \hat{\mathbf{u}}_x \quad (2.23)$$

The total far-field electric field is given by:

$$\mathbf{E}_0 = \mathbf{E}_x^s + \mathbf{E}_x^r = -I_s \frac{jc\mu e^{-jkR_o}}{4\pi^2} \frac{1}{R_o} \left[\frac{g}{g^2 - 1} + \tan(g) \right] \hat{\mathbf{u}}_x \quad (2.24)$$

For a source located at an arbitrary angle ϕ_i along the structure, the far-field electric field contribution \mathbf{E}_i can be expressed as

$$\mathbf{E}_i = E_0 [\cos(\phi_i) \hat{\mathbf{u}}_x + j\sin(\phi_i) \hat{\mathbf{u}}_y] \quad (2.25)$$

where

$$E_0 = -I_s \frac{jc\mu e^{-jkR_o}}{4\pi^2} \frac{1}{R_o} \left[\frac{g}{g^2 - 1} + \tan(g) \right] \quad (2.26)$$

The total electric field due to N identical sources (with current I_s) along the structure is given by,

$$\mathbf{E}_{\text{Tot}} = \sum_{i=1}^N \mathbf{E}_i = -NI_s \frac{jc\mu e^{-jkR_o}}{4\pi^2 R_o} \left[\frac{g}{g^2 - 1} + \tan(g) \right] (\cos(\phi_i)\hat{\mathbf{u}}_x + j\sin(\phi_i)\hat{\mathbf{u}}_y), \quad (2.27)$$

From Equation 2.27, the far-field electric field is directly proportional to the number of sources on the structure, thus power combining can be achieved using multiple sources. To obtain a rotating far-field electric field $N \geq 2$ and the sources have to be phased such that currents injected into the structure add constructively. That is, the phase difference between adjacent sources along the ring must equal the propagation delay the wave travels between them.

Equation 2.27 shows that a key parameter of an MPD ring antenna is g which determines if the currents on the ring and spokes to add up coherently and radiate effectively or destructively resulting in no radiation. When the terms $\frac{g}{(g^2-1)}$ and $\tan(g)$ have the same sign, constructive interference occurs and result in a non-zero far-field electric field as shown by Figure 2.11. This condition is met in the range $1 < g < \pi/2$ which is a design guideline for effective radiation for an MPD ring antenna.

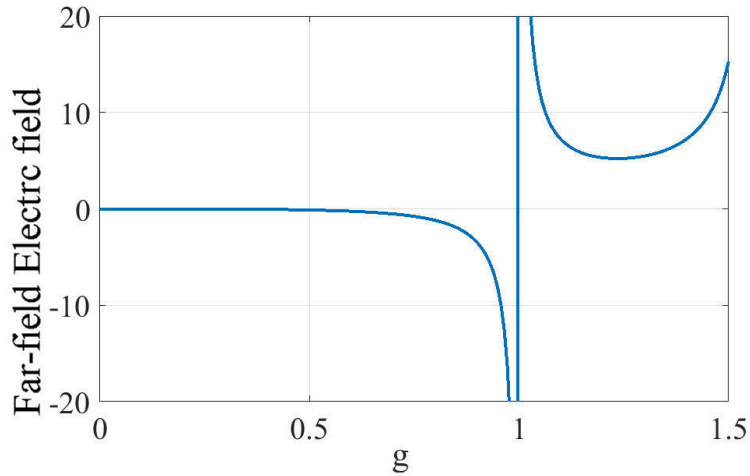


Figure 2.11: Far-field electric field of an MPD as a function of g .

The spoke and ring design shown in Figure 2.9 features a multi-layered structure with the spokes on a lower level and ring on a plane above the spokes, and two ground planes. A fabrication challenge with the spoke and ring MPD antenna is to route the tracks to the driven points along the ring. This necessitates the use of multiple metal layers which equates to more fabrication steps and costs. A complementary structure

of the MPD ring antenna is a slot-ring and is presented in [44] which is a more straightforward ring slot with integrated sources at desired points along the slot-ring. The slot-ring is particularly interesting due to the relatively less complicated fabrication procedure compared to the ring MPD since it requires less metallisation layers and hence fewer fabrication steps and masks. A drawback of the slot-ring MPD however, is the backside radiation as shown in Figure 2.12. In this Thesis, the slot-ring MPD antenna is studied with the objective of improving its radiation characteristics for the purposes of integrating with RTD oscillators for millimetre wave communications which is envisaged as an enabler for 5G networks.

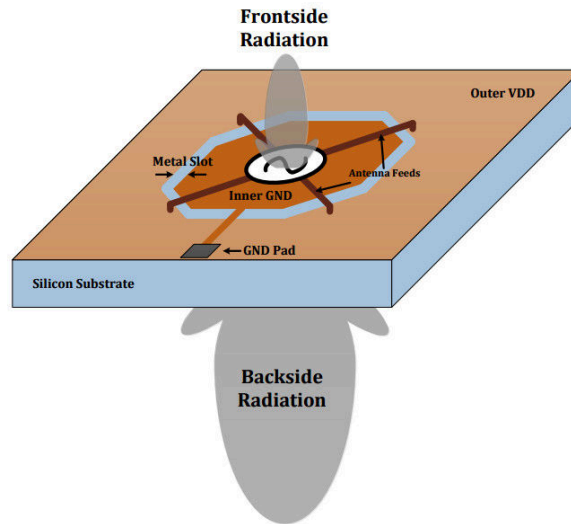


Figure 2.12: A slot-ring multi-port driven antenna on silicon substrate with backside radiation [44].

2.2 Low-cost printed antennas

In recent years, conventional printing techniques have been used to fabricate low-cost electronics on a wide range of substrates. The areas of application for printed electronics include, but are not limited to; antennas [21], sensors and circuits [25, 28], large and flexible displays [45], and photo-voltaic cells [46] some of which are shown in Figure 2.13. These printing methods are primarily additive procedures, thus reduce material waste compared to conventional silicon based techniques which are mainly subtractive methods. This makes them cost-effective for large-area electronics and potentially more environmentally friendly since they avoid the use of etching chemicals. Moreover, these printing techniques do not require the use of expensive

controlled environments (i.e. clean rooms), thus avoiding the costs associated with acquiring and operating such facilities.

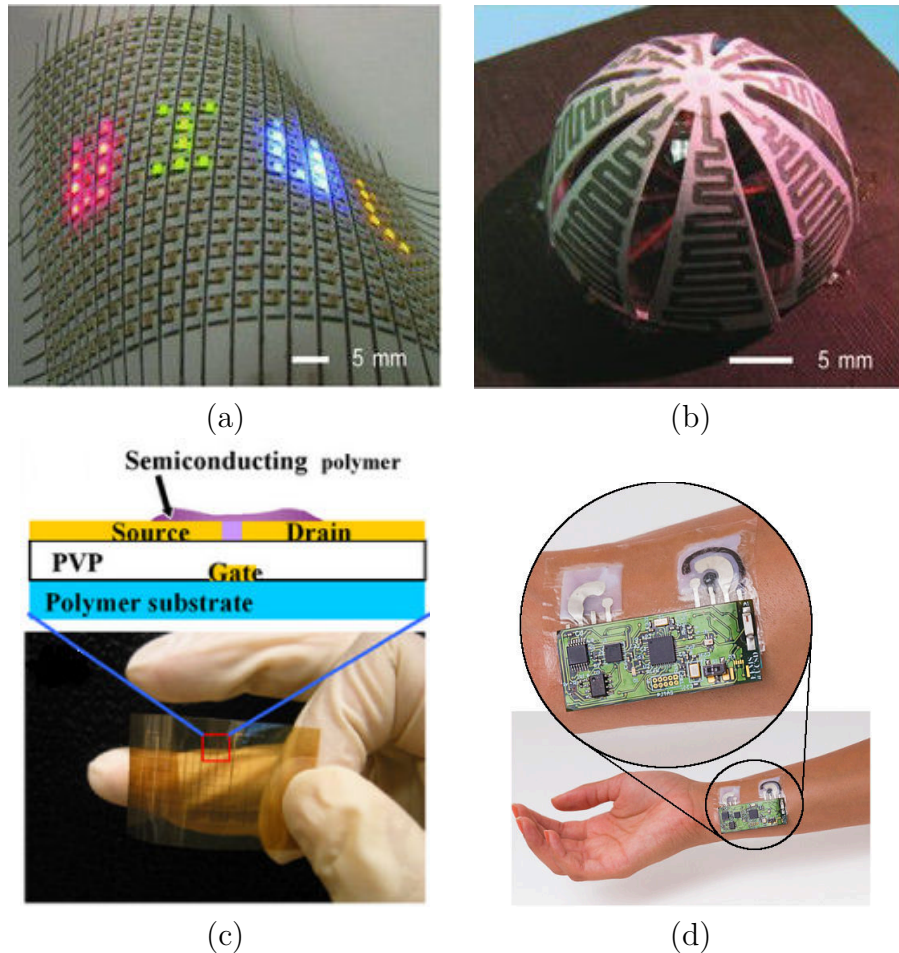


Figure 2.13: Applications of printed large-area electronics including (a) flexible display [45], (b) three dimensional printed antenna [45], (c) printed field effect transistor [47], and (d) wearable sensors.

Careful choice of low-cost, lightweight, flexible and renewable substrates makes printed electronics more versatile in areas of application. They can be unobtrusively integrated to consumer electronics, wearable electronics, hidden/embedded security codes, and sensors. The relative short fabrication time of these methods is attractive for fast, large scale manufacturing of electronics or rapid prototyping of designs. The most pervasive printing techniques used for printed electronics are inkjet, gravure and screen printing. These methods involve the use of conductive inks or pastes to create the desired patterns which are then sintered in an oven (or other means) to achieve electrical conductivity. An alternative to inkjet printing and screen printing is re-

ported in [48] which employs conductive adhesive tapes on which a desired pattern is etched using photo-lithography (or laser-cutting equipment) and then transferred to a paper substrate using a sacrificial layer. The process achieves better conductivity and lower losses than inkjet printing, allows soldering of components, and is marginally cheaper than inkjet. However, the use photo-lithography step presents a compromise between environmental friendliness for performance. Screen printing of dielectric antennas and passive microwave components has also received some attention in recent years [49, 50]. An exhaustive list of printing techniques for electronics is outside the scope of this Thesis and can be found in [51]. Figure 2.14 shows a selection of the most common techniques used in printed electronics which are then described subsequently.

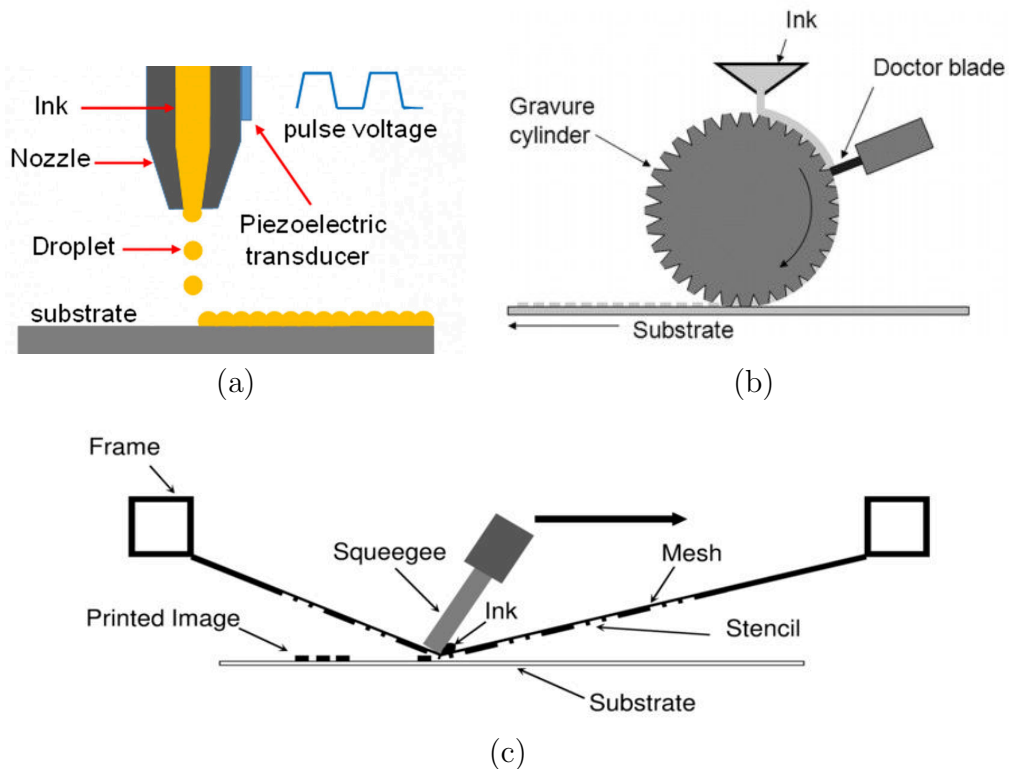


Figure 2.14: Low cost printing techniques for electronics (a) drop on demand inkjet printing [52], (b) gravure printing [53], and (c) screen printing [54].

Inkjet printing uses piezoelectric actuated nozzles which allow the ink drops to pass when activated by an image signal and is commonly referred to as drop on demand. The conductive ink is deposited on to the moving substrate below as illustrated in Figure 2.14(a) creating the desired image. Gravure printing uses a cylinder on which the desired pattern is embossed. During printing, the grooves on the cylin-

der are filled with ink and the excess ink is removed by the doctor blade. The ink is then transferred to the substrate upon contact with the gravure cylinder as shown in the schematic in 2.14(b). Screen printing uses a patterned screen on which the negative areas are masked by use of an emulsion on a porous mesh screen. During printing, the ink is forced through the unmasked areas of the screen by a squeegee thus creating a pattern on the substrate as demonstrated in Figure 2.14(c).

After printing, the traces are typically sintered in an oven to dry the ink/paste and improve electrical conductivity. Typically curing is done at 120°C for approximately one hour or more depending on the ink and substrate. High temperature curing often causes permanent damage to some substrates [55] thus limiting the number of substrates that can be used with these methods. Alternative sintering methods have been investigated as a work around the problem in [56] with flash sintering [57], laser sintering [47] and development of low-temperature sintering inks [58] being advanced as viable solutions. While screen printing and gravure printing can achieve high printing throughput in roll-to-roll manufacturing scenarios, the need to fabricate masks and pattern the gravure cylinders make low quantity and custom designs uneconomical. Inkjet printing allows a digital image to be directly printed from design making it suitable for custom designs and low batch production like rapid prototyping. As a result, inkjet printing has been widely adopted for printed electronics.

2.2.1 Thermal transfer printing method

Thermal transfer printing (TTP) allows direct printing of a digital image of the desired pattern without any modification to the printer or an intermediate step which is required for both screen and gravure printing. Because the image is printed directly from digital format, successive prints can be unique allowing custom designs, rapid prototyping and cost effective low batch manufacturing. Moreover, the printed traces do not require a sintering or curing stage and can be used immediately after printing. The achievable printing speeds of TTP are up to 5 cm/s with thermal printheads of up to 600 dpi resolution currently available in the market [59]. With careful choice of substrates and conductive ribbons, the achievable printing speeds of TTP are up to 20 cm/s (8 inch/s) [60]. There are potential benefits for advancing the TTP fabrication technique in printed and flexible electronics to produce low-cost and custom electronics with the capacity for high volume roll-to-roll production.

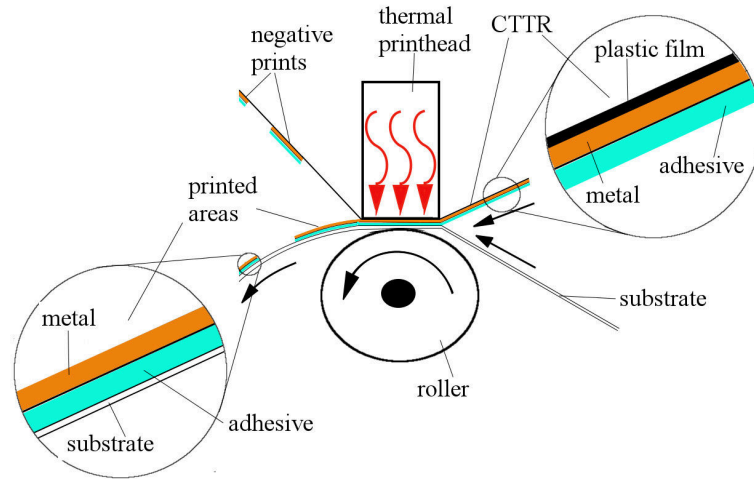
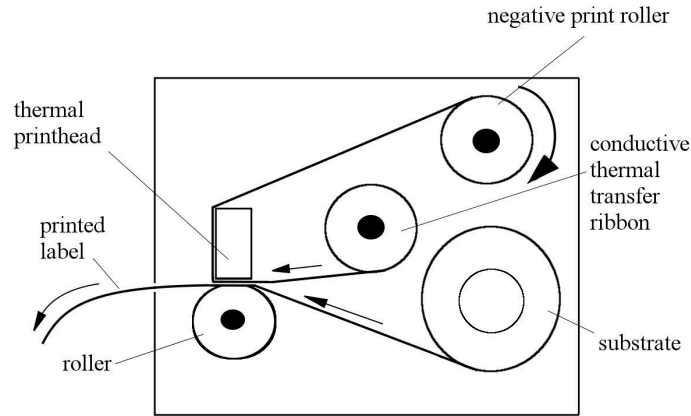


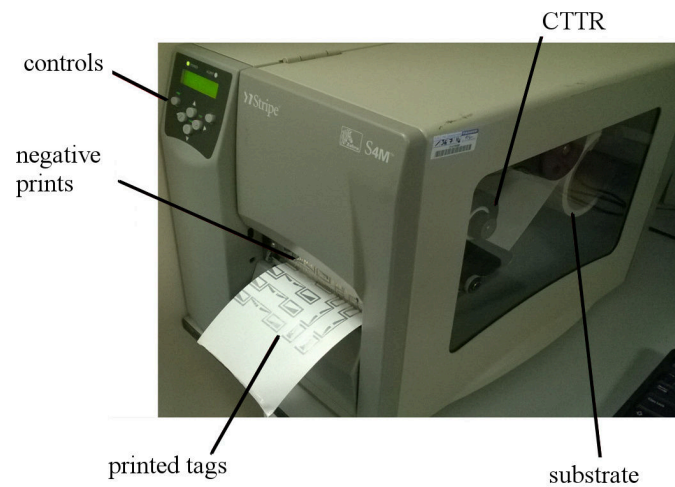
Figure 2.15: Schematic of the thermal transfer printing process [61].

Thermal transfer printing uses a multi-layered ribbon containing a heat-activated ink layer. For metal printing, the ribbon features a plastic membrane on top of which a thin layer of metal is bonded using a resin, and a heat-sensitive acrylic adhesive on top of the metal. Printing is achieved by using a thermal print-head to selectively activate the desired regions of the heat-sensitive adhesive. The thermal print-head is essentially made of an array of resistors which produce heat when a current is passed through them. The heat-sensitive adhesive adheres to a compatible substrate placed in physical contact with the ribbon when heat is applied and in the process, transfers the metal from the ribbon to the substrate as shown by Figure 2.15. A schematic of the Zebra S4M thermal printer used is shown in Figure 2.16(a) showing the operation of the printer, while a photograph of the printer used in this Thesis is shown in Figure 2.16(b). The printer has a print-head resolution of 300 dots per inch (dpi) and an adjustable print speed of up to 20 cm/s. The sample can be used immediately with no drying or curing required.

The suitability of TTP traces for use in printed electronics is studied subsequently in this Thesis with application in fabrication of antennas and waveguides. Thermal transfer printed radio frequency (RF) waveguides and antennas are then characterised from DC to 10 GHz on flexible substrates for IoT applications. Direct performance comparisons are also made to inkjet printing which is an established technique for printed electronics using the read range of radio frequency identification (RFID) an-



(a)



(b)

Figure 2.16: Schematic showing operation (a) and a photograph (b) of the Zebra S4M thermal printer [61].

tennas fabricated by the two techniques.

2.3 Millimetre-wave communications

The requirements of fifth generation (5G) of mobile networks are dominated by low latency, high data rate, and low costs [62]. In order to meet the bandwidth demands projected for 5G, the millimetre-wave spectrum has been considered for wireless communications [63]. The millimetre-wave band is the range of frequencies that lie between the microwave and infrared bands and is defined by free space wavelength between 1 mm to 10 mm (that is, frequencies from 30 GHz to 300 GHz) by the inter-

national telecommunications union (ITU) [64] while IEEE defines the millimetre-wave band from 110 GHz to 300 GHz [65]. The range of frequencies between 300 GHz and 3 THz is known as the submillimetre band and commonly referred to as the terahertz band [66]. Electromagnetic waves in the millimetre-wave and submillimetre-wave (terahertz) band suffer high atmospheric attenuation mainly due to oxygen and water vapour as shown in Figure 2.17 which limits the maximum achievable communication distances. Careful band selection by targeting the frequencies that experience comparatively lower attenuation within the band could potentially avail an aggregate of up to 252 GHz bandwidth for 5G communications [67]. To counter the effects of atmospheric attenuation, beam-forming techniques are often used to produce directional beams [68] which could be used to increase communication range. The fine spatial resolution of these beams makes it possible to accommodate many users in picocell and/or femtocell deployments by allowing frequency re-use within a small geographical area [69] and has also found uses in radar [70] and imaging applications [71]. The use of directive antennas and the short propagation distances of millimetre-waves also have security benefits by limiting the location of a potential eavesdropper [72].

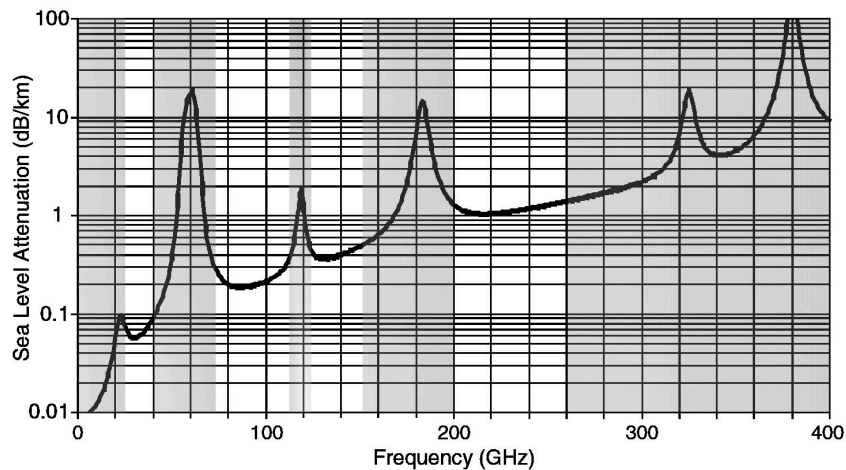


Figure 2.17: Average sea-level millimetre-wave atmospheric attenuation [73]

The frequency bands around 30 GHz have traditionally been used in point-to-point scenarios connecting sites or as last mile connectivity in local multipoint distribution systems (LMDS) over long distances due to the lower atmospheric attenuation [74]. However these bands are strictly regulated and have narrow bands by spectrum regulation authorities (26MHz in UK and 56MHz in US) [73, 75]. The limited bandwidth places a constraint on the maximum achievable data rates. To meet the high data rate

requirements of 5G, the 70-90 GHz band is a viable candidate with the band available in most countries [73]. The available bandwidth makes this frequency band suitable for high data rate backhaul links. The 220-300 GHz band is suitable for picocell and femtocell settings or machine to machine (M2M) communications due to localised beam footprint and short propagation distances. The 60 GHz band has been used and allocated in some countries for backhaul links [76] and small volume pico-cell applications [15] despite the high atmospheric attenuation.

One of the limitations of millimetre and submillimetre-wave consumer electronics communications has been the lack of availability of compact, low-cost, and low-noise radio frequency (RF) sources that operate at room temperature [77]. Resonant tunnelling diode (RTD) oscillators have been demonstrated to be capable of room temperature operation in the entire millimetre wave band [78–80] and up to a few terahertz [81]. RTD based oscillators are compact and relatively simple circuits with radio frequency (RF) output power around 1 mW in the millimetre-wave band. An RTD based oscillator at 28 GHz with phase noise of -95 dBc/Hz at 100 kHz was demonstrated in [78]. While an oscillator with around 1 mW power at 300 GHz was demonstrated in [82]. Future targets for 5G deployment is to build millimetre-wave transceiver systems with power output of approximately 10 mW to achieve reasonable communication range (around tens of metres) at the upper end of the millimetre-wave band (300 GHz).

Resonant tunnelling diodes operate by quantum mechanical tunnelling phenomenon across a double barrier formed by a highly doped quantum well layer sandwiched between two thin barrier layers as shown in Figure 2.18. The quantum well has a conduction band at higher energy level than both the emitter and collector at zero bias as shown in Figure 2.19(a). When no bias voltage is applied there is zero net current flowing between emitter and collector. When a positive bias voltage is applied across the emitter and collector, electrons flow across the barrier with increasing bias voltage as the energy level of the emitter increases resulting almost linear current increase. Applying a bias voltage (V_p) where the conduction band of the emitter equals that of the well results resonance and a peak current (I_p) as shown in Figure 2.19(b). An increase in bias voltage beyond V_p results in current drop because the emitter conduction band is higher than the quantum well conduction band (off-resonance) resulting in reduction of current and a net negative differential resistance (NDR) as shown in 2.19(c). Further increase in bias voltage beyond V_v where the

current is lowest results in diode-like behaviour as shown by the I-V curve shown in 2.19(d). Due to the double barrier structure symmetry, an ideal RTD I-V curve has an odd symmetry. In practice however, fabrication variations often result in slightly non-ideal behaviour where the I-V curve is not symmetric around the origin.

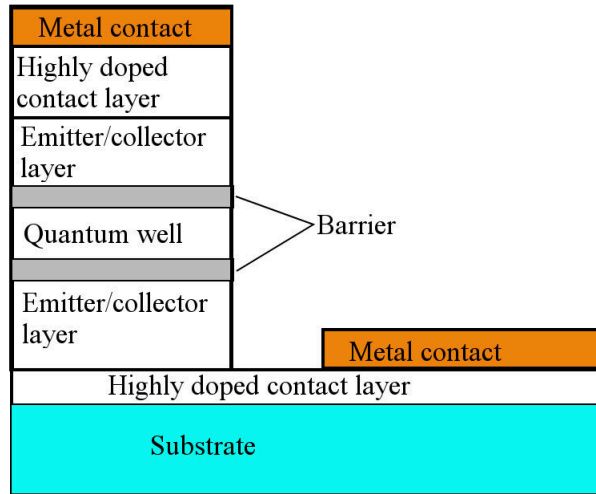


Figure 2.18: Simplified epitaxial structure of a resonant tunnelling diode.

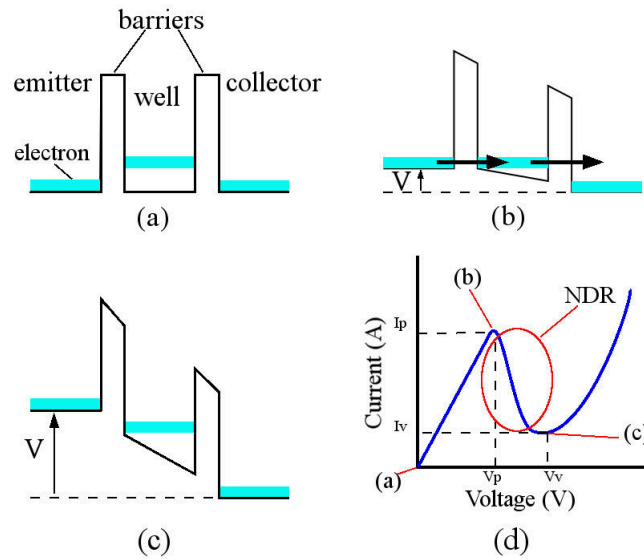


Figure 2.19: Conduction band profile of an TRD at different bias voltages; (a) zero bias, (b) resonance, (c) off-resonance and (d) the corresponding current-voltage relationship.

The negative differential resistance allows RTDs to be used in oscillator circuits by connecting them in parallel with an inductor L , forming an LC tank circuit with

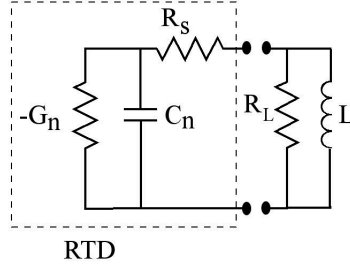


Figure 2.20: An RTD oscillator circuit showing the small signal model (dotted box), inductor (L) and load (R_L).

the RTD self-capacitance C_n . A schematic of an RTD-based oscillator is shown in Figure 2.23 with the small signal model of an RTD shown in the dotted line. The series resistance R_s arises from the contact resistance, negative conductance $-G_n$ is the reciprocal of value of the negative differential resistance and self capacitance C_n is proportional to the physical size of the RTD. The inductor L is normally realised by passive structures in monolithic microwave integrated circuits (MMIC) [79, 83] or is the effective impedance of an integrated antenna [81]. The oscillation frequency of the circuit is then given by;

$$f_{osc} = \frac{1}{2\pi\sqrt{C_n L}} \quad (2.28)$$

The load R_L can also be an instrument (oscilloscope or spectrum analyzer) or antenna (integrated or off-chip).

At millimetre and submillimetre-wave frequencies, the losses along the transmission lines and matching networks are significant which makes the use of off-chip antennas inefficient. To minimise or eliminate these losses, integrated antennas are favoured where the antenna is part of the oscillator circuit as shown in Figure 2.21.

Planar antennas at the millimeter-wave frequencies suffer from low efficiency due to the excitation of surface waves as the substrate gets electrically large beyond a quarter of a wavelength [39]. The excitation of surface waves confines some - and in some cases all- of the antenna's radiated energy in the substrate instead of into the air. Moreover, the surface waves travelling along the substrate diffract at the edges as they exit the substrate and interfere with the desired radiation pattern. Thus, the radiation of the integrated antennas in Figure 2.21(a) and (b) are lateral and backside respectively. To improve the radiation pattern, the substrate was thinned in [84] as shown in Figure 2.21(a). In most cases the thickness of the substrates can not be made electrically thin due to manufacturing process, materials used and packaging

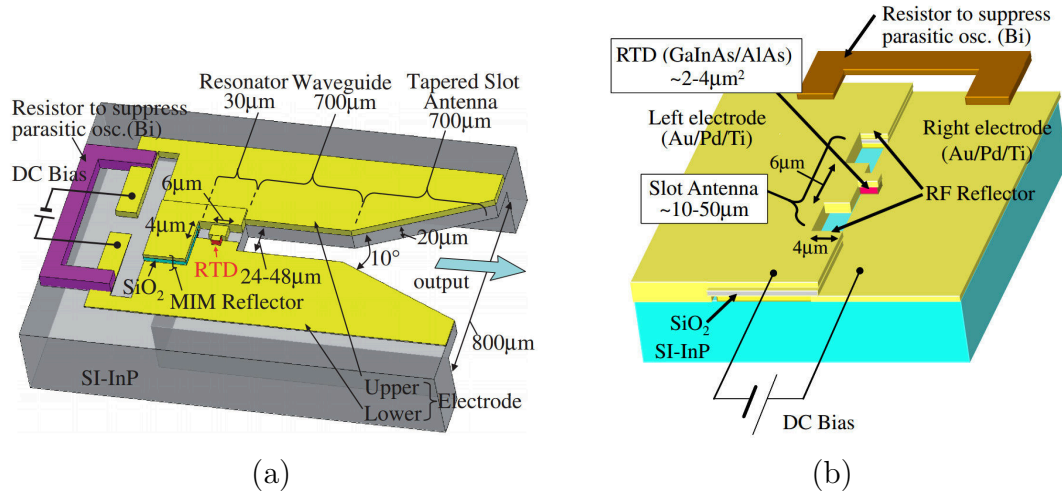


Figure 2.21: Antennas integrated into RTD oscillator circuits; (a) planar horn antenna [84] and (b) planar slot antenna [37].

constraints. A lens was used along with the slot antenna in [37] to focus the radiated power on the backside of the chip. A patch antenna fabricated on top of the slot was used to improve air-side radiation which avoids the use of the bulky lens [85] as shown in Figure 2.22(a). A wideband slot bow-tie antenna with a reflective ground plane has been studied as an alternative alternative for an integrated solution [86] and shown in Figure 2.22(b). In this Thesis a slot-ring multi-port driven antenna is investigated for integration with RTD oscillators.

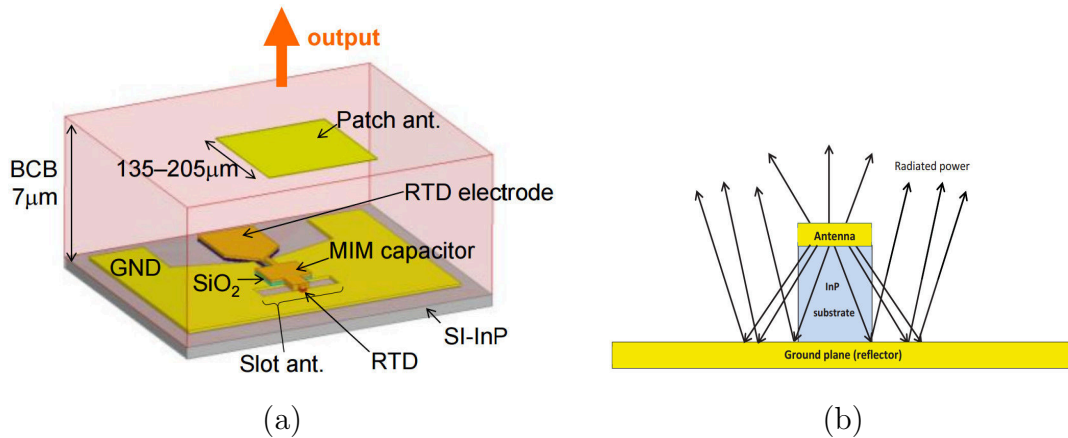


Figure 2.22: Antenna with improved airside radiation suitable for integration with RTDs; (a) Slot-coupled patch antenna [85] and (b) Slot bow-tie antenna with a reflecting ground for improved airside radiation [86].

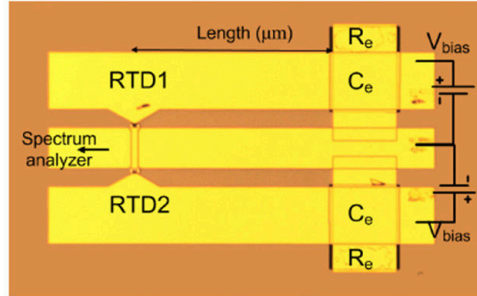


Figure 2.23: Power combining using two individually biased RTD oscillator circuits [78].

Power combining using arrays of RTDs has been demonstrated to improve total output power for applications that require more power [87]. Injection-locking of individual oscillators to achieve high output power has been explored in [88]. An oscillator using two individually biased circuits was used to realise an RF output power of around 1 mW [78]. While improving the output power of individual RTD oscillator circuits is still an active research topic it is reasonable to expect the use power combining techniques to play an active role in deployable communication systems. An integrated multi-port driven (MPD) antenna was used with eight phase controlled sources at 161 GHz on a silicon substrate with up to -25.8 dBm received signal power on an overall area of 1 mm². The MPD antenna offers a compact power combining solution that can be utilised for RTD based transceivers.

2.4 Chapter summary

In this Chapter, key antenna figures of merit that are used for performance evaluation in this Thesis have been provided along with some examples of antennas. The background on low cost printed antennas on flexible paper substrates has also been established. The thermal transfer printing method which is a printing technique that is subsequently studied in the this thesis as a viable alternative for direct printing of electronics is introduced. Millimetre-wave communications as an enabler for the next generation of wireless communications is also discussed. Resonant tunnelling diode oscillator circuits are also presented as a key enabler for millimetre-wave communications. The background of a slot-ring multi-port driven antenna is presented which will be subsequently studied for integration with RTD oscillator circuits for the purposes of building an integrated RF front-end for millimetre-wave communications.

Chapter 3

Methods

Antenna design is an iterative process that involves at least one, and often multiple passes of the design cycle which is made of the following steps; design and/or simulations, fabrication and characterisation. This chapter discusses the methods and tools used to design, analyse, fabricate and characterise antennas in this Thesis.

3.1 Antenna design and simulation tools

In the case of simple antenna geometries (e.g. dipole), the current distribution on the antenna structure can be calculated or approximated with reasonable accuracy which allows a designer to estimate antenna key performance parameters (e.g radiation pattern). For complex and arbitrary antenna geometries, the current densities are often difficult to compute or do not have close form solutions hence simulation tools are required to estimate the performance. A number of electromagnetic simulation tools are available commercially and in open source allowing antenna design and analysis. These simulation tools use either one or a selection of computational electromagnetic techniques to solve for the propagation and scattering of electromagnetic energy. The common techniques for computational electromagnetics are finite difference time domain (FDTD), method of moments (MoM), and finite element method (FEM). Each technique has its merits and limitations and suitability of application of each method is determined by the problem being studied. In this thesis, an open source FDTD-based simulation tool was used due to budgetary constraints and the technique is briefly described subsequently.

3.1.1 Finite-difference time domain method

The finite difference time domain (FDTD) method solves Maxwell's partial differential equations using finite difference approximations in the time domain. The FDTD method is a relatively intuitive and straightforward implementation, and allows for broadband computations [89]. In three dimensional (3D) FDTD, the volume that includes and surrounds the device under test (DUT) is discretised into unit cubic cells known as Yee cells. Each cell is then assigned electromagnetic material properties of the objects that occupy them. The evolution of the electromagnetic energy in each cell is advanced in discrete time steps according to the material properties in each cell. FDTD is based on Yee's algorithm which is dependent on the location of the electric and magnetic fields on the unit cell as shown in Figure 3.1 [90]. The electric field components are placed in the center of the cube's face while the magnetic field components are placed along the edges as shown in the Figure. It is worth noting that this arrangement is not compulsory and in some implementations, the electric fields could be placed along the edges while the magnetic fields are placed on the faces. Either arrangement ensures that each \mathbf{E} component is surrounded by four circulating \mathbf{H} components from neighbouring cells shown in faded colour in Figure 3.1. Similarly, each of the \mathbf{H} components is also surrounded by four circulating \mathbf{E} components. This arrangement of fields allows Ampere's and Faraday's Laws to be calculated in an alternating fashion, and thus fully describing the propagation of electromagnetic energy.

Faraday's law and Ampere's law in linear, isotropic, lossy materials, with independent electric and magnetic sources \mathbf{J}_{source} and \mathbf{M}_{source} are given by [89]:

$$\frac{\partial \mathbf{H}}{\partial t} = -\frac{1}{\mu} \nabla \times \mathbf{E} - \frac{1}{\mu} (\mathbf{M}_{source} + \sigma^* \mathbf{H}) \quad (3.1)$$

$$\frac{\partial \mathbf{E}}{\partial t} = \frac{1}{\epsilon} \nabla \times \mathbf{H} - \frac{1}{\epsilon} (\mathbf{J}_{source} + \sigma \mathbf{E}) \quad (3.2)$$

with the relations

$$\mathbf{B} = \mu \mathbf{H} \quad (3.3)$$

$$\mathbf{D} = \epsilon \mathbf{E} \quad (3.4)$$

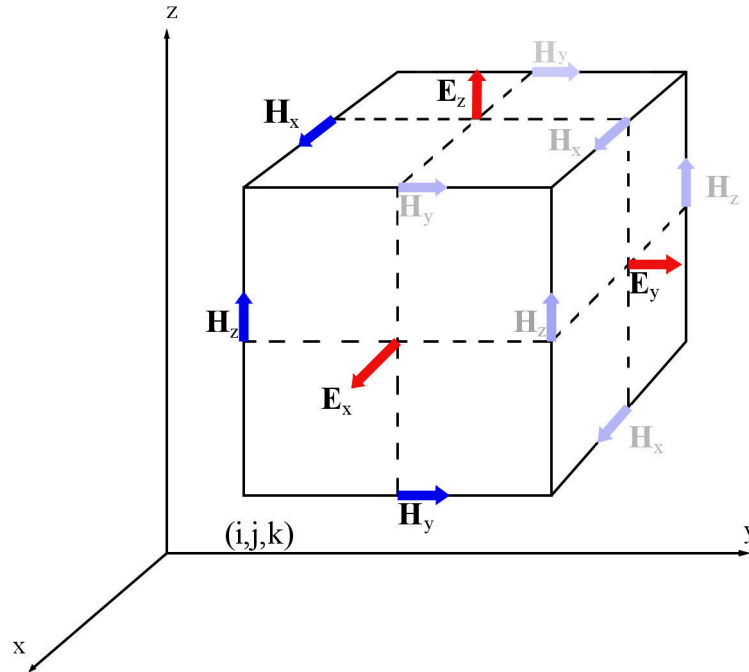


Figure 3.1: Field position on a cubic unit cell

where;

- B** : Magnetic flux density
- E** : Electric field
- M** : Magnetic current density
- D** : Electric flux density
- H** : Magnetic field
- J** : Electric current density
- μ : Magnetic permeability
- ϵ : electrical permittivity
- σ : electric conductivity
- σ^* : equivalent magnetic loss

The x component of the electric field E_x of equation 3.2 is given by

$$\frac{\partial E_x}{\partial t} = \frac{1}{\epsilon} \left[\frac{\partial H_z}{\partial y} - \frac{\partial H_y}{\partial z} - (J_{source_x} + \sigma E_x) \right] \quad (3.5)$$

which can be approximated at a spatial location $(x,y,z)=(i,j,k)$ at time-step n , denoted $E_x|_{i,j,k}^n$, by

$$\frac{E_x|_{i,j+1/2,k+1/2}^{n+1/2} - E_x|_{i,j+1/2,k+1/2}^{n-1/2}}{\Delta t} = \frac{1}{\epsilon_{i,j+1/2,k+1/2}} \cdot \begin{pmatrix} \frac{H_z|_{i,j+1,k+1/2}^n - H_z|_{i,j,k+1/2}^n}{\Delta y} \\ -\frac{H_y|_{i,j+1/2,k+1}^n - H_y|_{i,j+1/2,k}^n}{\Delta z} \\ -J_{source_x}|_{i,j+1/2,k+1/2}^n \\ -\sigma_{i,j+1/2,k+1/2} E_x|_{i,j+1/2,k+1/2}^n \end{pmatrix} \quad (3.6)$$

Approximating the electric field at time-step n as an average of the $n - 1/2$ and $n + 1/2$ i.e.

$$E_x|_{i,j+1/2,k+1/2}^n = \frac{E_x|_{i,j+1/2,k+1/2}^{n+1/2} + E_x|_{i,j+1/2,k+1/2}^{n-1/2}}{2}$$

and isolating $E_x|_{i,j+1/2,k+1/2}^{n+1/2}$ gives

$$\begin{aligned} E_x|_{i,j+1/2,k+1/2}^{n+1/2} &= \left(\frac{1 - \frac{\sigma_{i,j+1/2,k+1/2}\Delta t}{2\epsilon_{i,j+1/2,k+1/2}}}{1 + \frac{\sigma_{i,j+1/2,k+1/2}\Delta t}{2\epsilon_{i,j+1/2,k+1/2}}} \right) E_x|_{i,j+1/2,k+1/2}^{n-1/2} \\ &+ \left(\frac{\frac{\Delta t}{\epsilon_{i,j+1/2,k+1/2}}}{1 + \frac{\sigma_{i,j+1/2,k+1/2}\Delta t}{2\epsilon_{i,j+1/2,k+1/2}}} \right) \cdot \begin{pmatrix} \frac{H_z|_{i,j+1,k+1/2}^n - H_z|_{i,j,k+1/2}^n}{\Delta y} \\ -\frac{H_y|_{i,j+1/2,k+1}^n - H_y|_{i,j+1/2,k}^n}{\Delta z} \\ -J_{source_x}|_{i,j+1/2,k+1/2}^n \end{pmatrix} \end{aligned} \quad (3.7)$$

In equation 3.7 the future value of the electric field at timestep $n+1$ depends only on the current value of the energy in the cell and the neighbouring cells. This allows the use of simple arithmetic equations to update the x-component of the electric field in each cell at each time step. The y and z components of the electric field E_y and E_z can be derived in a similar way. Similarly, the x,y and z components of the magnetic field H_x , H_y , and H_z can also be derived giving a full set of update equations used in Yee's algorithm.

To ensure stability, the grid size has to be such that there is no significant change in electromagnetic field from one cell to the next. The condition that ensures stability is [90]:

$$c\Delta t < \sqrt{(\Delta x)^2 + (\Delta y)^2 + (\Delta z)^2} \quad (3.8)$$

where c is the speed of light, Δx , $\Delta y, \Delta z$ are the cell dimensions and Δt is the discrete time step.

OpenEMS

For the work presented in this Thesis, OpenEMS was used to simulate the designed antenna performance. OpenEMS is an open source electromagnetic field solver based on FDTD written in C++ with a Matlab (or Octave) interface through which the simulation parameters are specified. Matlab post-simulation operations subroutines are used to analyse the simulation data. OpenEMS has been verified and validated as a simulation tool and has been used in a number publications [91–93]. A typical simulation scenario for antenna design include the antenna geometry, a Gaussian excitation centred at the design frequency for broadband analysis, some ambient material surrounding the antenna (typically air or free space) and some absorbing boundary conditions to truncate the simulation domain. The maximum mesh cell size was at most a tenth (often smaller than a tenth) of the wavelength of highest frequency excited by the source while the minimum cell size was determined by the smallest feature size of the antenna geometry. An air spacing of at least a quarter wavelength of the longest wavelength excited in the simulation was added to the domain around the antenna in all directions. The grid was truncated with a perfectly matched layer (PML) which is an absorbing material to minimise reflections at the boundaries to simulate an unbounded domain [94]. PML is shown to be 40 dB more accurate than second order Mur’s absorbing boundary conditions (ABC) [95] and is the boundary used in all simulations. A good trade off between computational burden and electromagnetic absorption of PML thickness is between four and eight cells [95]. Thus, eight cells of PML were used in all domain boundaries to achieve reasonable computation times. A near-field-to-far-field (NF2FF) box was added one cell from the start of the PML layers in all directions. The fields logged in the NF2FF box were then used in the post processing to calculate the far field radiation pattern using Matlab scripts that are part of the OpenEMS tool. A graphical representation of the simulation domain is shown in Figure 3.2. A stopping criteria was set to halt simulations when total energy present in the simulation domain fell below 10000th (-40 dB) of the peak total energy. OpenEMS allows modelling of lumped circuit components such as resistors, capacitors and inductors and can be integrated with circuit simulators [96] which was done to model some circuits in this Thesis.

OpenEMS allows logging of electric and magnetic fields during simulation time in Visualisation Tool Kit (VTK) compatible formats. The field files can be viewed and analysed during simulation time and one need not wait for the simulation to complete. Paraview, which is an open source data analysis and visualisation tool was

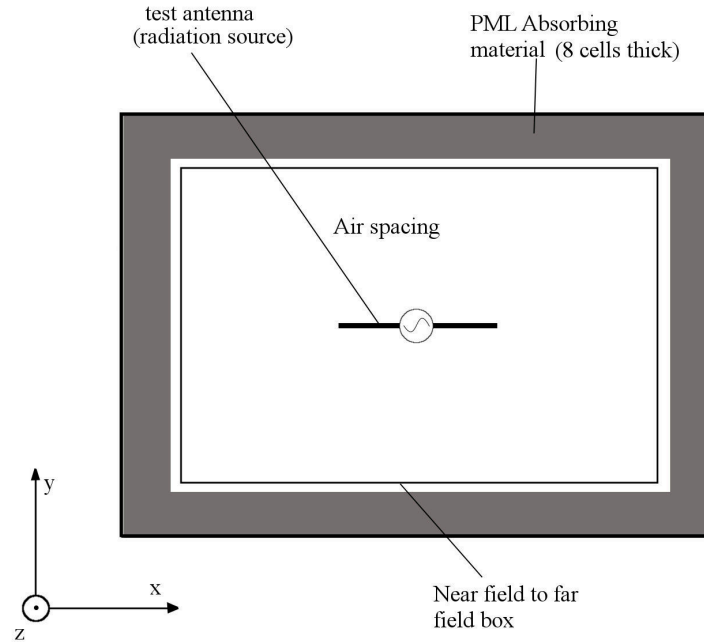


Figure 3.2: Typical antenna simulation scenario

used to analyse the simulation log files.

3.1.2 Antenna design tools

The GNU Image Manipulation Program (GIMP) version 2.8 which is an open source graphics editor was used to create the printed antenna designs. The dimensions of optimal designs obtained via simulations were used to create images in portable document format (PDF) compatible with the Zebra S4M printer. GIMP was also used to create masks required for photolithography process for antennas fabricated on printed circuit boards (PCB).

3.2 Antenna fabrication

In this Thesis two main antenna fabrication methods were used. The thermal transfer printing (TTP) technique was used for flexible polymer substrates while the photolithography process was used for fabricating the slot-ring multi-port driven antenna on printed circuit boards.

3.2.1 Printed antennas

A Zebra S4M 300 dots per inch (dpi) thermal printer was used along with two different IIMAK Metallograph™ Conductive Thermal Transfer Ribbons (CTTR). One ribbon had a 260 nm thick aluminium film while the other has 340 nm thick copper film. Both ribbons have a 1 μm thick heat-sensitive acrylic adhesive. A range of substrates were explored for compatibility with TTP. The tested substrates includes Magnum Materials Limited’s 50MIC White Polytherm UL Perm and Fastransfer Superior S2000, Kapton, fabric (cotton) and Flexcon’s THERMLfilm SELECT 21944E (formerly TC-390). THERMLfilm SELECT 21944E achieved the best adhesion resulting in consistent continuous traces than the other tested. Therefore, THERMLfilm SELECT 21944E was chosen as the substrate to study TTP. THERMLfilm SELECT 21944E is a polyester based flexible substrate with a glossy finish backed with an acrylic adhesive and a removable glassine liner suitable for TTP. The relative dielectric constant of THERMLfilm SELECT 21944E is 3.2 [97]. For brevity, THERMLfilm SELECT 21944E will be referred to as THERMLfilm throughout the Thesis.

Table 3.1: Metallograph ribbon : key parameters

	Ribbon no.1	Ribbon no.2
Metal	Aluminium	Copper
Metalisation thickness	260 nm	340 nm
Adhesive	1 μm	1 μm

The Zebra S4M printer has adjustable settings which are key to achieving successful prints. To obtain consistent prints, the printer mode was set to **transfer mode**, print speed 5 cm/s and a darkness of 30 (which is a measure of the heat intensity). The optimal printing settings were achieved by varying the parameters on the printer and observing the print quality under a microscope. Further characterisation of the continuous tracks was done by use of the four probe method to obtain the sheet resistance. The results of which are discussed in subsequently. A summary of the optimal printer settings used to fabricate antennas is presented in Table 3.2.

Table 3.2: Zebra S4M printer settings for THERLfilm

CTTR	Aluminium	Copper
Print mode	transfer	transfer
Darkness (heat intensity)	30	30
Print speed	5 cm/s	5 cm/s

Conductive epoxy was used to attach connectors and other circuit components (e.g. RFID chips, inductors and diodes) to the printed tracks.

3.2.2 Photolithography process

The slot-ring multi-port driven (MPD) antenna was fabricated at the Electronic Workshop at the University of Glasgow using the photolithography process. The photolithography is commonly used to fabricate printed circuit boards (PCB) and includes the following steps:

1. Photoresist is applied to a laminated board which has a $735\ \mu\text{m}$ layer of copper on both sides,
2. A mask is placed and aligned on top of the undeveloped photoresist
3. Exposure and development of the photoresist by exposure to ultra violet (UV) light to reveal the areas to be etched away,
4. Etching is achieved by placing the sample in an acid bath which etches away the unmasked areas,
5. The photoresist is finally removed from the sample.

The masks used in the Thesis were designed by GIMP and then printed on a transparent paper.

3.3 Antenna measurement tools

A Nearfield Systems Inc. (NSI) 2000 near-field spherical scanner antenna measurement system was used to characterise the antennas operating between 500 MHz and 20 GHz. The system has a rotating stage on which the antenna under test (AUT) is placed and a probe mounted on a robotic arm as shown in Figure 3.3. The system is housed in a $4.5 \times 4.5 \times 4.0\ \text{m}^3$ reflection-less room equipped with EHP-18PCL microwave absorber rated for 500 MHz-40 GHz operation [98] and isolated from external electromagnetic energy by a Faraday cage. During measurement, the AUT is placed at the center of the room. Then the probe mounted on the probe-arm scans the electric field around the antenna under test in the elevation plane (θ) in incremental steps specified by user. For every complete scan in the elevation plane, the rotating stage advances the azimuth angle (ϕ) by a pre-determined angle until the

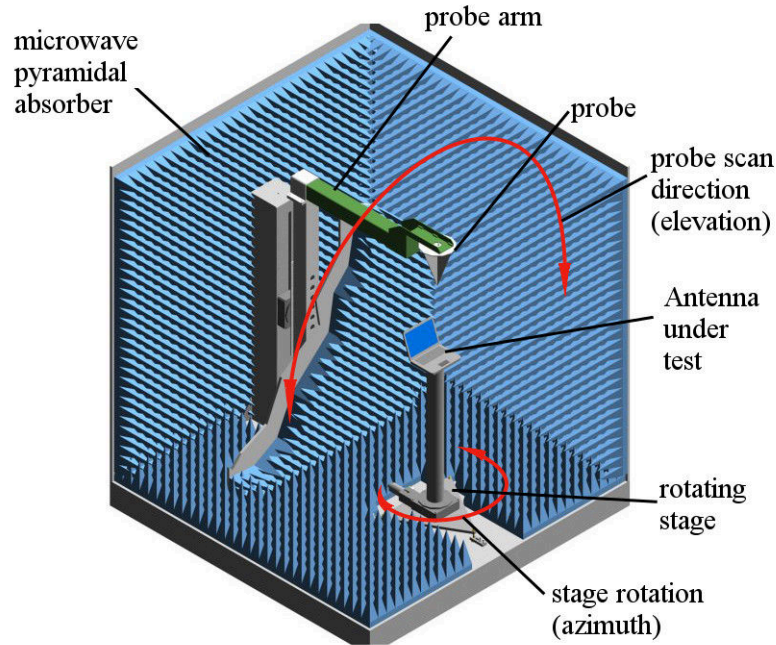


Figure 3.3: NSI 2000 near-field spherical scanner antenna measurement system

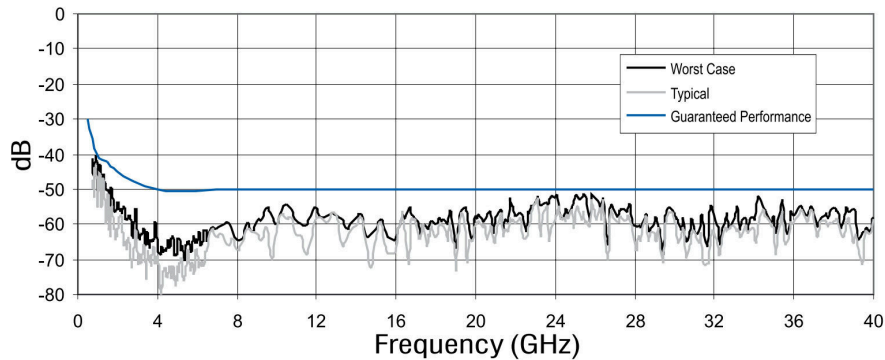


Figure 3.4: Microwave absorber reflections at normal incidence [98]

probe covers a sphere around the antenna that forms the near-field. Scanning of the RF energy is automated by the NSI2000 software. The measured near-field electric field is then fed to a nearfield-to-farfield (NF2FF) transform to obtain the far-field radiation pattern of the antenna at frequencies of interest. The NF2FF transform is performed by the NSI2000 software. The gain of the antenna under test can then be calculated by using the comparison method, in which the far-field maximum is compared to a reference antenna with a known gain. The antenna used as a reference was Aaronia AG's BicoLOG 20100 which has known gain from 20 MHz to 3000 MHz. Return losses of the antennas were characterised by Agilent Technologies E8362B PNA Network Analyzer calibrated using Agilent 3.5 mm Economy Calibration Kit.

3.4 Chapter summary

In this Chapter, the methods used for designing, simulating and characterising antennas are provided. The finite-difference time-domain (FDTD) method for full wave analysis was introduced highlighting how it solves electromagnetic propagation and scattering. OpenEMS was also introduced which is an open source computational electromagnetic solver that uses the FDTD method and was used in the design and analysis of antennas presented in this Thesis. The thermal transfer printing (TTP) method along with the associated equipment used to fabricate low-cost, flexible IoT antennas was also introduced. The TTP method is studied in detail in subsequent Chapters as a viable method of for producing low-cost large scale electronics. The antenna characterisation tools used in this Thesis to measure the performance of antennas were described as well.

Chapter 4

Characterisation and Performance Evaluation of Thermal Transfer Printed Traces

In this Chapter, the physical and electrical properties of thermal transfer printed traces from direct current (DC) up to 10 GHz are characterised. Then a performance comparison to inkjet printing, which is the most pervasive technique for printed electronics is made using the reading range of RFID antennas as a performance metric. Section 4.1 presents the physical and electrical characterisation of thermal transfer printed traces while Section 4.2 presents a performance comparison to inkjet printing which is an established and pervasive printed electronics technique. Chapter conclusions are subsequently drawn in Section 4.3.

The work presented in this Chapter was published in [61] by Kgwadi, M., Rizwan, M., Ajith, A. K., Virrki, J., Ukkonen, L., and Drysdale, T.D., “Performance Comparison of Inkjet, and Thermal Transfer Printed Passive UHF RFID tags,” *IET-Microwaves, Antennas and Propagation* and is reproduced in this Thesis with permission from Institution of Engineering and Technology (IET).

4.1 Characterisation of thermal transfer printed traces

Thermal transfer printing is a relatively new technique for fabricating electronics. It is therefore critical to characterise its key properties that influence performance of

electronics to determine its benefits and limits as a guide to designers. This Section characterises the thermal transfer printing process to determine its suitability as well as limits to fabricating electronics. The physical characteristics including feature size and print quality of the traces are made as well as electrical properties from DC to 10 GHz.

4.1.1 Physical characterisation

Thermal transfer printing achieves consistent traces on THERMLfilm from both the aluminium and copper conductive thermal transfer ribbons (CTTR) using the settings in Table 3.2. White light optical microscope images of the metal traces are shown in Figure 4.1 with aluminium in Figure 4.1(a) and copper in Figure 4.1(b). The images show hairline discontinuities on both the aluminium and copper traces. The discontinuities are more clearly shown in the aluminium trace due to the contrast in the picture but the density is higher in the copper traces ($\sim 8/\text{mm}^2$). These discontinuities are attributed to the mechanical stresses associated with the handling of this prototype material, although further investigations are required to characterise their formation and elimination, such a study is outside the scope of this Thesis and deferred to future studies.

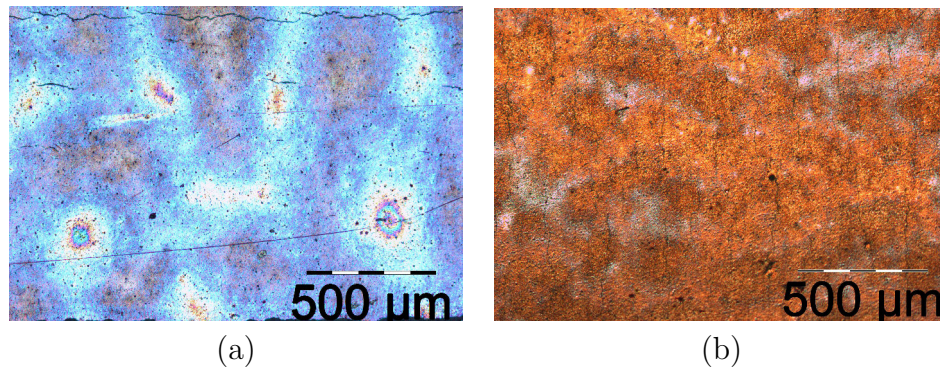


Figure 4.1: Microscope images of printed traces on THERMLfilm substrate. Aluminium trace (a) and copper trace (b) [61].

Figure 4.2 shows a printing resolution test using the copper CTTR. The feature size is determined by the printhead which in this Thesis is a 300 dots per inch (dpi) resolution. The minimum feature size to obtain consistent continuous traces is $155\ \mu\text{m}$ as shown on the close up on bottom right of Figure 4.2. The track is equivalent to 2

pixels on the 300 dpi (1 pixel is $85\ \mu\text{m}$) printer used for this study. TTP results in non-ideal rough edges and hairline discontinuities on the prints for both aluminum and copper CTTRs as shown in Figure 4.3 (a) and (b) respectively. The estimated edge roughness for both CTTR is approximately $10\ \mu\text{m}$ which places a constraint on the smallest feature size than be achieved with the equipment used in this Thesis. We note that there are thermal printers available on the market that have a resolution of up to 600 dpi [59] that would potentially achieve a higher resolution and smoother edges and overall improved print quality allowing smaller feature size. Budget constraints limited the acquisition of higher resolution thermal printers. The smallest separation (gap) between prints achieved was $208\ \mu\text{m}$ as shown on the bottom left of Figure 4.2, this corresponds to about 3 pixels. The gap between prints is critical for high frequency waveguides such as coplanar waveguides (CPW) and slot-lines printed using this method as it places the limit on the minimum separation between the signal and ground lines. The feature size achievable through TTP using a commercially available Zebra S4M 300 dpi printer with no modifications are comparable to those achieved in [48] which achieves $200\ \mu\text{m}$ line/gap size with the use of photo-lithographic etching technology.

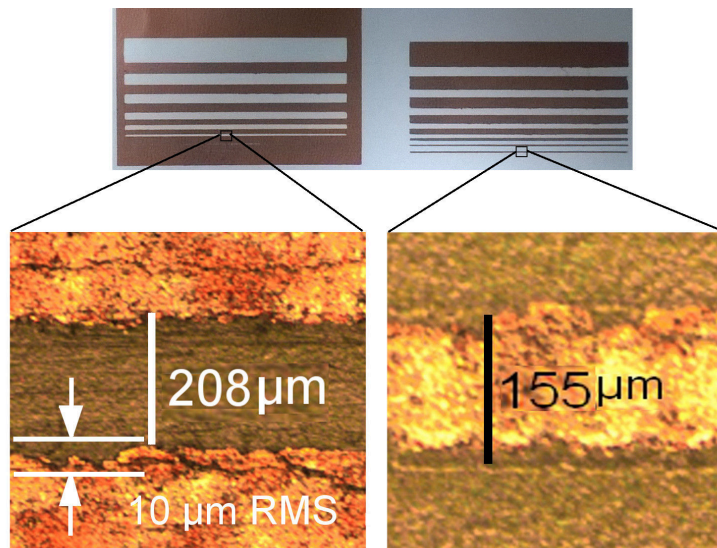


Figure 4.2: Thermal transfer printing resolution test with a copper CTTR

An atomic force microscope (AFM) surface roughness measurement of both aluminium and copper traces was made on an area of $5 \times 5\ \mu\text{m}$. The surface roughness of the aluminium and copper traces are shown in Figure 4.4(a) and Figure 4.4(b) respectively. The aluminium traces had a root-mean square (RMS) roughness of $20.8\ \text{nm}$ while the copper traces have an RMS roughness of $19.8\ \text{nm}$. The copper traces have

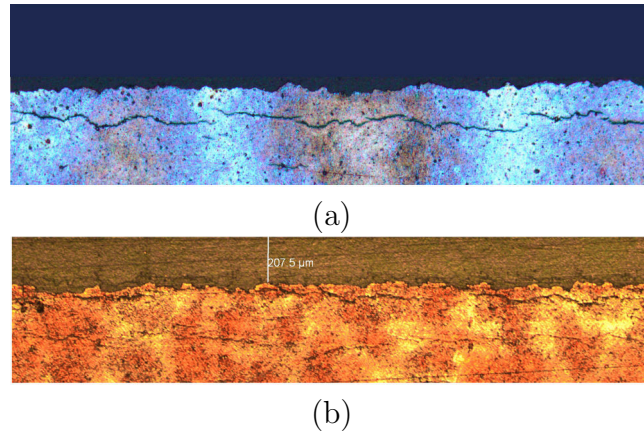


Figure 4.3: Microscope images of printed traces on THERMLfilm substrate showing the morphology of the edges. Aluminium trace (a) and copper trace (b) [61].

a marginally smoother surface than aluminium with 0.4 nm average (1.0 nm rms). Surface and line-edge roughness is known to result in current scattering in microwave circuits. Current scattering due to surface roughness can cause up to 40% increase the resistivity of thin films [99] which is expected to result in low efficiency.

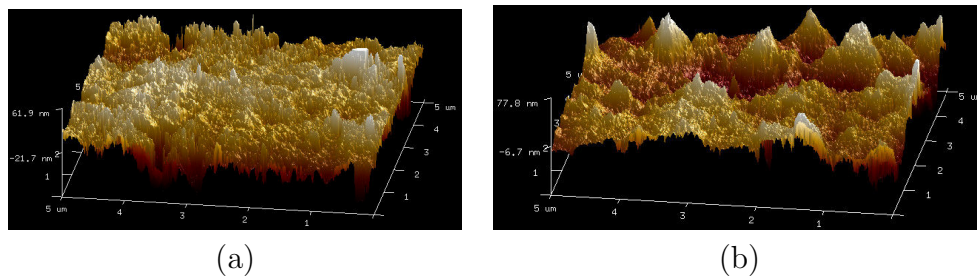


Figure 4.4: AFM images showing the surface roughness of thermal-transfer printed traces on THERMLfilm. Aluminium trace surface morphology (a) and copper trace surface morphology (b) [61].

4.1.2 Electrical characterisation

The TTP traces were characterised to obtain the DC sheet resistance and the frequency dependant characteristics up to 10 GHz.

DC characterisation

The sheet resistance of the thermal transfer printed traces on THERMLfilm was measured by the four probe method on a 5 cm by 5 cm square patch using Agilent's B1500 Semiconductor Device Analyzer with American Probe & Technologies' Quasi Kelvin Probes. The sheet resistance measured for both copper and aluminium traces show a dependence on the direction of print. This artefact is attributed to the printhead elements being positioned in a row across the width of the print substrate, perpendicular to the direction of substrate movement. The result of which is better electrical conduction along the row than between rows. The aluminium traces have a measured sheet resistance of $0.16 \Omega/\square$ along print direction and $0.15 \Omega/\square$ across the print direction. Copper traces have a measured sheet resistance of $0.10 \Omega/\square$ along the print direction and $0.08 \Omega/\square$ across the print direction. Thus the highest conductivity of the aluminium and copper traces are $2.6 \times 10^7 \text{ S/m}$ and $3.9 \times 10^7 \text{ S/m}$ respectively.

RF characterisation

Coplanar waveguides (CPW) are a good choice for use for this particular printing technique and thin substrates because the impedance can be controlled by the lateral dimensions unlike microstrip waveguides which are heavily dependant on substrate thickness. Moreover, only one side print is required which simplifies fabrication by avoiding precision alignment during assembly. For this study, two CPW lines made from aluminium and copper were printed and then characterised from DC to 10 GHz. Coplanar waveguides of the two available CTTRs (Al and Cu) were simulated in OpenEMS to estimate the performance of the waveguides. The dimensions of the CPW lines are identical; center conductor 4 mm, gap $210 \mu\text{m}$, length 50 mm and ground width 10 mm. The fabricated CPW line are shown in Figure 4.5 with the copper at the top of the figure and the aluminium at the bottom of the figure. The CPW designed has a characteristic impedance of 60Ω instead of the ideal case of 50Ω due to the restriction on the width of the center conductor placed by the separation of the ground planes on the sub-miniature version A (SMA) connectors. A 50Ω CPW with a $210 \mu\text{m}$ gap would be 10 mm which is wider than the SMA connectors available. It should be noted that a higher resolution printer will be able to reduce the CPW gap allowing for a narrower center conductor.

The simulated and measured reflection and insertion losses of the aluminum and copper CPW lines are shown in Figure 4.6(a) and (b) respectively. The s-parameters

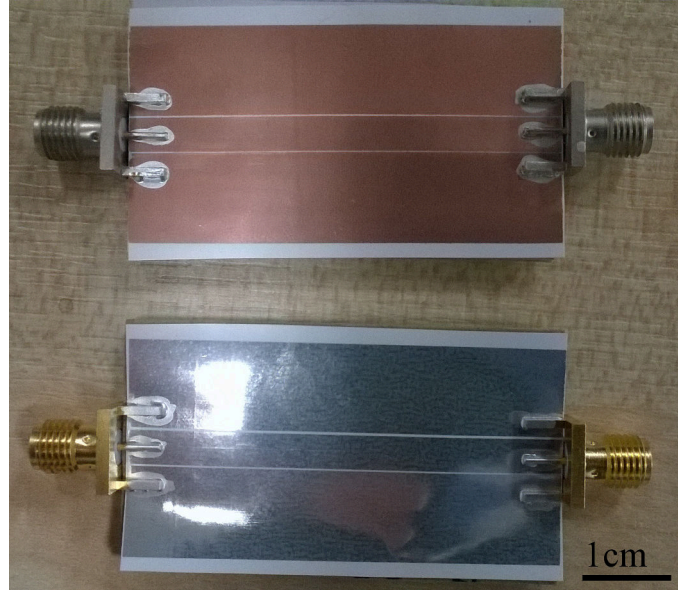


Figure 4.5: Photographs of the fabricated CPW lines with SMA connectors.

were characterised by Agilent Technologies E8362B PNA Network Analyzer calibrated using Agilent 3.5 mm Economy Calibration Kit using the Short-open-load-through (SOLT) calibration standard. The return losses (S_{11}) are well below the -10 dB through out the band even with the impedance mismatch between the SMA connector and the CPW. The return losses of the aluminium CPW matches well with the simulation results with a slight shift in frequency due to the presence of a backing glassine cover at the back of the substrate that protects the adhesive. The measured insertion losses (S_{21}) matches well with the simulation from DC up to about 6 GHz where there is a significant divergence between the curves due to the surface and line edge roughness of the printed waveguides. In the simulations, the metalisation is simulated with perfectly straight edges and a smooth surface which accounts for the difference in simulations and measurements. The surface and line edge roughness of the printed areas is known to result in scattering and increased ohmic losses [99,100], increasing the insertion losses. This effect gets amplified at higher frequencies as the size of the roughness undulations become electrically significant compared to the wavelength as shown by the difference of about 4 dB at 10 GHz compared to lower frequencies (close to DC).

The measured return losses copper CPW also agree well with simulations, staying well below -10 dB between DC and 10 GHz. The insertion losses in the copper CPW also follow a similar trend to the aluminum CPW. The losses get larger at higher

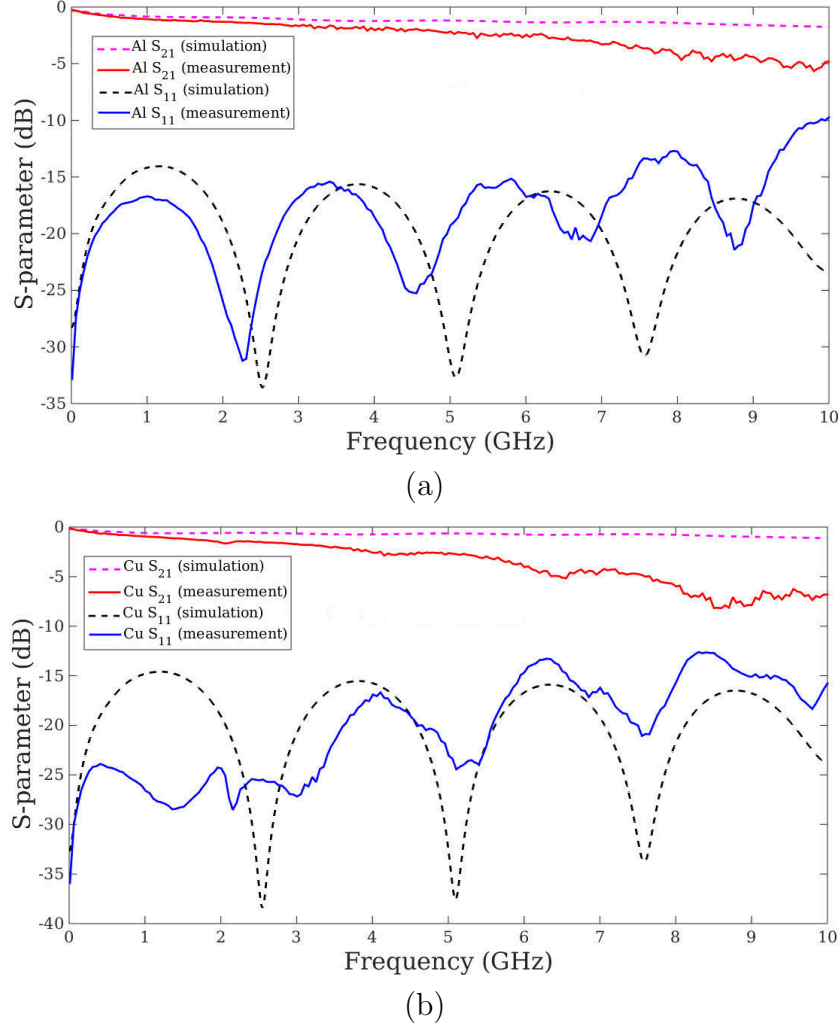


Figure 4.6: Microscope images of printed traces on THERMLfilm substrate. Aluminium trace (a) and copper trace (b) [61].

frequencies, and are -7 dB at 10 GHz which is significant. The insertion loss for the copper CPW are much higher than those measured in the aluminum CPW despite the fact that the copper traces have higher conductivity and thicker metal thickness.

The insertion losses of a 30 mm microstrip line in [48] which were fabricated using a photolithography process are 1.8 dB at 10GHz, which is equivalent to 0.6 dB/cm. For comparison, the two aluminium and copper thermal transfer printed CPW lines in this study have insertion losses of 1.0 dB/cm and 1.4 dB/cm respectively. TTP offers a fast and low-cost fabrication process with a performance penalty on the insertion losses compared to the microstrip waveguide in [48] which uses photo-lithographic

technology. However, the insertion losses of TTP can be further minimised by the use of a higher resolution printer (which are already available on the market) to improve the printing quality in particular surface and line edge roughness and deferred for future work.

4.2 Performance Comparison with Inkjet using RFID tags

The performance of thermal transfer printing was then benchmarked to inkjet printing which is one of the most pervasive method for printed electronics. This part of the experiment was done in conjunction with a research team at Tampere University where the inkjet printing and the tag read range measurements were taken.

4.2.1 Inkjet printing

Inkjet printing of electronics has been studied extensively as fabrication method for large-area electronics (LAE) including but not limited to antennas, sensors and circuits [23, 25]. In this Thesis, we used a Fujifilm Dimatix DMP-2831 material inkjet printer, with 10 pL print nozzles. The ink was Harima's NPS-JL silver nanoparticle ink with particle sizes of 5-12 nm with a maximum achievable conductivity in the range of 1.6×10^7 - 2.5×10^7 S/m [101]. This particular ink was chosen because it is commonly used, but it is worth noting that other (potentially more cost-effective) metallic inks are available and under development [102]. The optimised inkjet printing key parameters are presented in Table 4.1. Four of the sixteen jets were used simultaneously to obtain continuous traces on THERMLfilm at a jetting voltage of 28 V and a cartridge temperature of 40 °C. A high platen temperature (60 °C) was used to reduce ink drying time, and the sample was left on the platen for two-three minutes before sintering to partially dry the ink so as to avoid ink movement or smearing during sample movement to the oven. The samples were then sintered for one hour at 150 °C in an oven.

Inkjet printing produces continuous traces on THERMLfilm when using the parameters in Table 4.1. As shown in Figure 4.7(a), a white light microscope image of the printed trace shows some small discontinuities in the printed traces, which were caused by air bubbles forming during jetting. A surface roughness measurement of a trace was made using a Bruker Dimension Icon atomic force microscope (AFM)

Table 4.1: Inkjet Printing Key Parameters [61].

Parameter	value
Platen Temperature	60 °C
Cartridge Temperature	40 °C
Max. Jetting Frequency	9 KHz
Jetting Voltage	28 V
Drop Velocity	8-9 m/s
Drop Volume	10 pL
Drop Spacing/Pattern resolution	40 μm /635 DPI

on an area of $5 \times 2 \mu\text{m}$ that was representative of the sample and is shown in Figure 4.7(b). The measured root mean square (RMS) surface roughness was 21.2 nm, which is comparable to the measurements in [103] of 22.1 nm (rms) inkjet printing on Polyetherimide (PEI), a substrate well suited to inkjet printing.

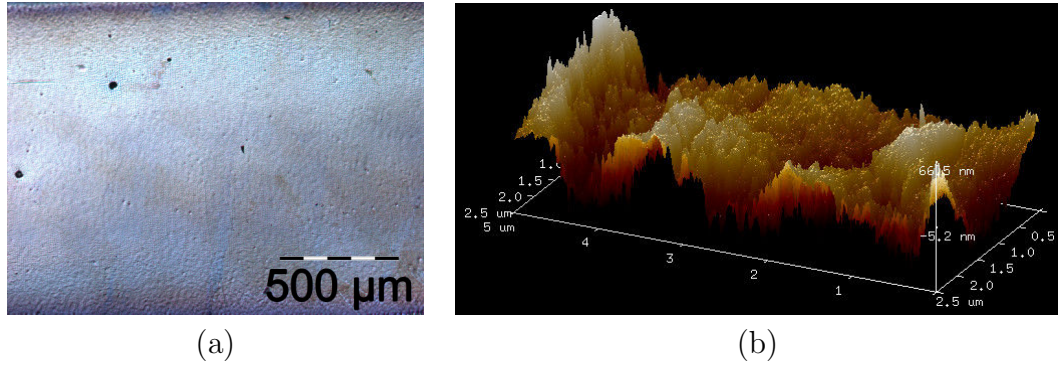


Figure 4.7: Physical characteristics of inkjet printed traces. Microscope image of inkjet trace on THERMLfilm (a) and an AFM image of inkjet trace on THERMLfilm. Note that the trace edges are outside the edge of the pictures, and that the AFM trace covers $\sim 1/100^{\text{th}}$ of the area shown in (a) [61].

The measured sheet resistance of the silver inkjet traces on THERMLfilm using the four probe method was $0.15 \Omega/\square$. The calculated conductivity using the average metal thickness and sheet resistance was $1.7 \times 10^7 \text{ S/m}$. The calculated skin depth for inkjet on THERMLfilm at 900 MHz is $4.1 \mu\text{m}$. THERMMLfilm has a porous surface and absorbs some of the ink and results in thinner metallisation for inkjet printing. To get optimal printing for inkjet printing, Kapton was used as a substrate for inkjet printing as a baseline for inkjet performance. Kapton is a polyimide with little ink absorption and has been used extensively for inkjet printing because it also has good thermal properties for sintering at high temperatures. For comparison, the

realised metal thickness on Kapton was $1.0\ \mu\text{m}$ while the measured sheet resistance was $0.056\ \Omega/\square$, yielding conductivity of $1.8\times 10^7\ \text{S/m}$. The skin depth of inkjet on Kapton is $3.9\ \mu\text{m}$ at 900 MHz. Thus the metalisation is 12.9% of the skin depth for inkjet printed traces on THERMLfilm, while it is 25.6% on Kapton. Therefore larger ohmic losses are expected on the inkjet printed traces on THERMLfilm than on Kapton.

Table 4.2: Key physical and DC characteristics of inkjet and TTP. Note that TTP sheet resistance and conductivity results are reported both perpendicular (\perp) and parallel (\parallel) to the direction of substrate movement [61]

	Inkjet THERMLfilm	TTP Aluminium THERMLfilm	TTP Copper THERMLfilm	Inkjet Kapton
Metal Thickness	400-600 nm	260 nm	340 nm	$1\ \mu\text{m}$
Surface Roughness (RMS)	21.2 nm	20.8 nm	19.8 nm	-
Sheet Resistance	$0.15\ \Omega/\square$ -	$0.15\ \Omega/\square\ \perp$ $0.16\ \Omega/\square\ \parallel$	$0.08\ \Omega/\square\ \perp$ $0.10\ \Omega/\square\ \parallel$	$0.056\ \Omega/\square$ -
Conductivity	$1.7\times 10^7\ \text{S/m}$	$2.6\times 10^7\ \text{S/m}$	$3.9\times 10^7\ \text{S/m}$	$1.8\times 10^7\ \text{S/m}$
Skin Depth at 900 MHz	$4.1\ \mu\text{m}$	$3.4\ \mu\text{m}$	$3.1\ \mu\text{m}$	$3.9\ \mu\text{m}$

The metal thickness realised through thermal transfer printing appears relatively thin (260 nm for aluminium and 340 nm for copper) compared to ink-jet metal thickness which can be over $1\ \mu\text{m}$. This difference would appear to be critical to the operation of a ultra-high frequency (UHF) radio frequency identification (RFID) tag where the skin depth is $\sim 2\ \mu\text{m}$ in pure copper at 1 GHz. However, the quality of the deposited metal (represented by its conductivity or sheet resistance) is also a determining factor, as is the influence of substrate on adhesion of the ink, surface and line edge roughness, substrate losses and mechanical flexibility. An overall performance comparison between thermal transfer printing and inkjet is obtained by characterising a set of three UHF RFID antennas with different designs that use a representative mixture of thick and thin line widths. The comparison is limited to single layer prints of the designs using both inkjet and thermal transfer printing on the same substrate. Then determining from measurements, the maximum read range of the antennas give a direct comparison of the printing techniques for RFID IoT applications.

4.2.2 RFID antenna designs

To compare the effect of changing the technique for printing the metal antennas and circuit traces, the tags were kept as similar as possible. In particular, the same antenna designs, the same electronic circuit, and the same substrate were used. The use of the same substrate allows us to eliminate sources of variation arising from differences in the thickness, dielectric constant, dielectric loss, and surface roughness. The only substrate available to us that could achieve consistent results using both techniques was THERMLfilm SELECT 21944E. Three different UHF RFID tag antenna designs were chosen to highlight the benefits and limitations of the printing techniques. As shown in Figure 4.8, the antenna designs have different geometries featuring wide and narrow tracks that experience different conductor losses and are expected to have different read ranges. By using three different tags, we reduce the influence of any individual antenna design upon the results.

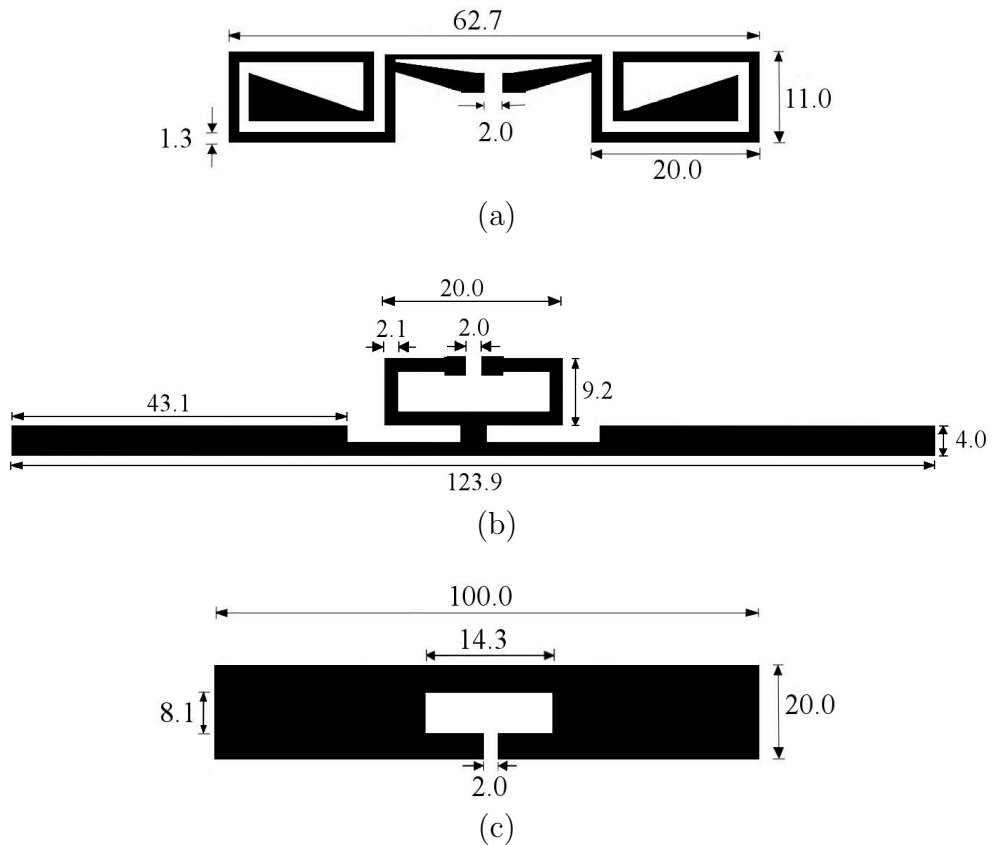


Figure 4.8: Schematics of the RFID tags; (a) Tag design 1, (b) Tag design 2 and (c) Tag design 3 [61]. All dimensions in millimetres.

NXP UCODE G2iL series RFID integrated circuits were attached to each of the fabricated antennas using conductive silver epoxy and the read range of the tags was measured in a 120x80x80 cm Voyantic RFID measurement cabinet (Anechoic Chamber) using a Voyantic Tagformance RFID measurement unit. The equipment calculates the theoretical read range d using the backscattered signal from the tag assuming a reflection-less environment :

$$d = \frac{\lambda}{4\pi} \sqrt{\frac{EIRP}{P_{th} L_{iso}}}, \quad (4.1)$$

where λ is the wavelength of the transmitted signal to the tag, P_{th} is the measured threshold power required to activate the tag, L_{iso} is the measured path loss, and $EIRP$ is the effective isotropically radiated power which is limited to 3.28 W according to the European regulations [104].

4.2.3 Simulation and measurement results

The material properties outlined in Table 4.2 were used to simulate the performance of each antenna design. THERMLfilm and Kapton films were modelled as 50 μm thick substrates with relative dielectric constants of 3.2 and 3.0 respectively. The conductive tracks of the antennas were modeled using the layered impedance boundary in HFSS. A lumped port with 50 Ω source impedance was used as excitation at antenna terminals. Read range of the tag was computed using Friis free-space equation as:

$$R_{range} = \left(\frac{\lambda}{4\pi}\right) \sqrt{\frac{\tau \cdot G_{Tg} \cdot EIRP}{P_{chip}}}, \quad (4.2)$$

where λ is the wavelength, τ is the power transmission coefficient, G_{Tg} is the gain of the tag, $EIRP$ is the equivalent isotropic radiated power and P_{chip} is the minimum power required to wake up the microchip. The power transmission coefficient depends on the antenna input impedance and the input impedance of the microchip as shown by the expression,

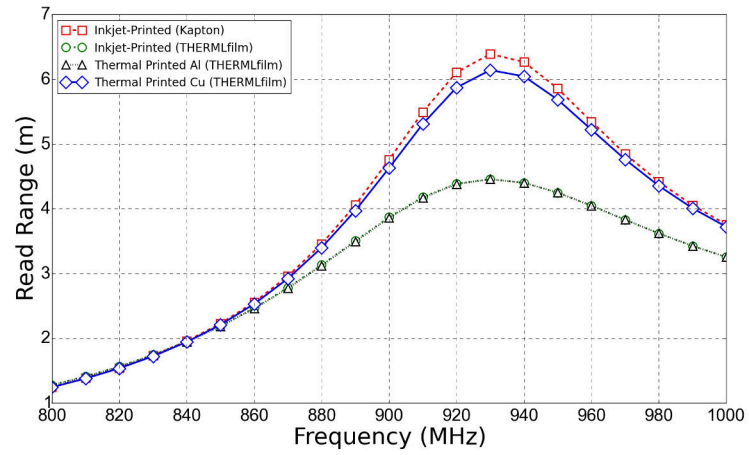
$$\tau = \frac{4R_A R_C}{(R_A + R_C)^2 + (X_A + X_C)^2}, \quad (4.3)$$

where $R_A + jX_A$ is the complex input impedance of the antenna and $R_C + jX_C$ is the complex input impedance of the chip. The equivalent circuit model of the NXP microchip developed in [105] was used to obtain the chip impedance across various frequencies.

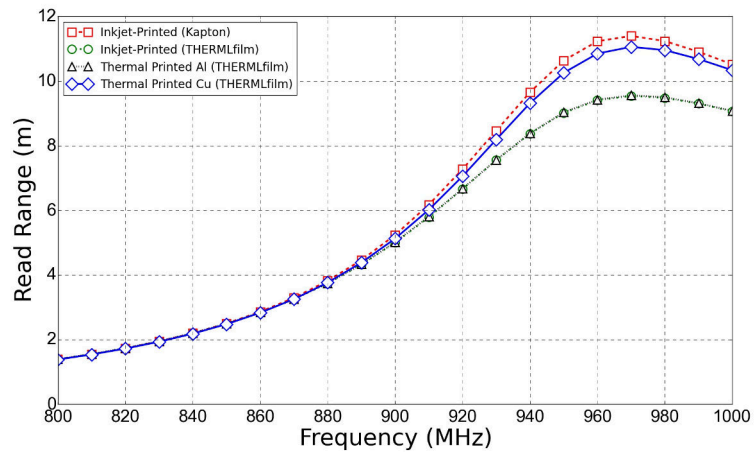
The read range estimates computed using Equation (4.2) are plotted against frequency as shown in Figure 4.9(a), 4.9(b), and 4.9(c) for tag design 1, design 2 and design 3 respectively. From the simulations, inkjet printed silver and thermal transfer printed aluminium on THERMLfilm substrate are expected to have very similar read range for all the tag designs. Inkjet printed silver on Kapton surface has the highest estimated read range, which is due to its higher thickness though its conductivity is lower. Thermal printed copper is expected to have a comparable albeit lower read range to inkjet printed silver on Kapton.

The average theoretical read range of tag design one fabricated by the two printing methods is presented in Figure 4.10. TTP copper antennas on THERMLfilm achieve a maximum read range of 6.6 m, while TTP aluminium antennas achieve 4.4 m read range. The difference of 2.2 m in the read range between the copper and aluminium TTP antennas is attributed to the higher conductivity of the copper traces and a thicker metalisation profile. These properties together with the narrow tracks of the antenna design results in significant conductor losses in the aluminium antennas and results in shorter average read range. The inkjet printed antennas on Kapton achieves a maximum read range of 5.9 m at 930 MHz. Inkjet printed antennas of THERMLfilm achieves a read range of 4.2 m, which is a 1.7 m less than the baseline performance. The difference is due to the suboptimal printing surface which results in thinner metalisation profile due to absorption of ink. The narrow metal tracks of the antenna design magnify the effects of the thin metalisation by increasing the ohmic losses, resulting in the significant reduction in reading range. The copper TTP antennas manages an improvement of 0.8 m in read range over the inkjet antenna on Kapton.

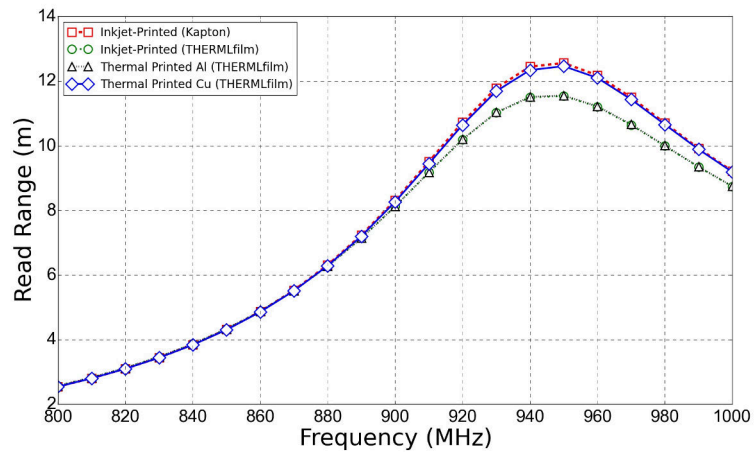
The average read ranges of antenna design two are shown in Figure 4.11. The printed examples all achieve relatively similar read range, which we attribute to the thick lines of the design reducing the conductor losses and masking the difference in conductivity. Inkjet printed tags on THERMLfilm achieves 7.9 m read range which is 0.7 m less than the baseline due to the afore-mentioned suboptimal substrate properties. Aluminum TTP antennas on THERMLfilm achieve a read range of 7.7 m, which is similar to inkjet on THERMLfilm with a difference of 0.2 m. The copper TTP antennas on THERMLfilm achieve peak read range of 9.0 m which is 0.4 m more than the baseline inkjet printed antenna. The inkjet on Kapton antennas achieve a maximum read range of 8.6 m at 960 MHz. The performance improvement of TTP copper over the baseline inkjet read range is due to the higher conductivity of the



(a)



(b)



(c)

Figure 4.9: Simulated read ranges for antennas using material properties in Table 4.2 (a) Tag design 1, (b) Tag design 2 and (c) Tag design 3 [61]

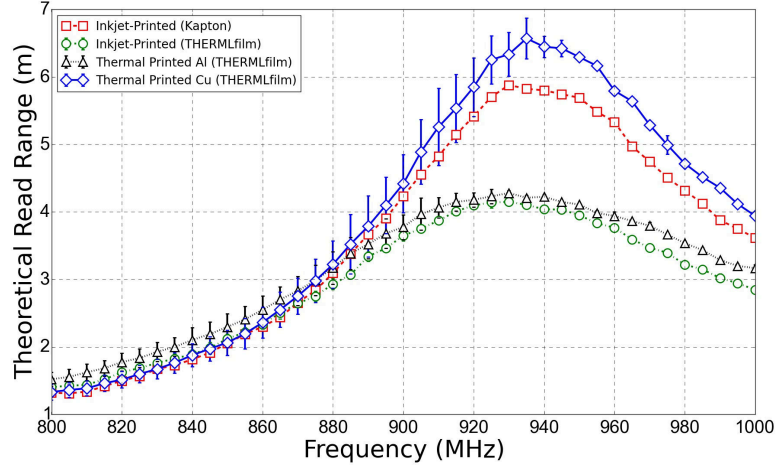


Figure 4.10: Measured theoretical reading range of tag design 1 fabricated by inkjet and thermal transfer printing methods [61]

copper traces (see Table 4.2).

The average read range of tags of design three are shown in Figure 4.12. There is more spread in the read range (2.3 m), similar to design one (1.2 m) due to the narrow and longer metal traces highlighting the effects of the conductor losses. Inkjet printed tags on THERMLfilm achieve a maximum read range of 9.2 m which is 1.6 m less than the baseline due to the suboptimal substrate. TTP aluminium antennas on THERMLfilm achieve a peak read range of 9.8 m, while the TTP copper antennas on THERMLfilm achieve a peak read range of 10.6 m. The inkjet tags on Kapton achieves a maximum read range equal to TTP copper tags on THERMLfilm of 10.6 m at 930 MHz.

A summary of the measured maximum read ranges is presented in Table 4.3. The achieved maximum theoretical read ranges by aluminium TTP antennas is equal to inkjet printing on THERMLfilm for the three designs in this study. The copper ribbon achieves better read range due a higher conductivity and a thicker metalisation compared to the aluminium ribbon leading to lower conductor losses, which gives an overall performance similar to inkjet on Kapton. The simulation results suggest that inkjet printing on Kapton could be slightly better than thermal transfer printing with copper, but these simulations do not take into account all of the fabrication parameters due to modelling the metallised regions with idealised smooth surfaces and edges. In practice, however, these surfaces have irregular edges and surfaces that

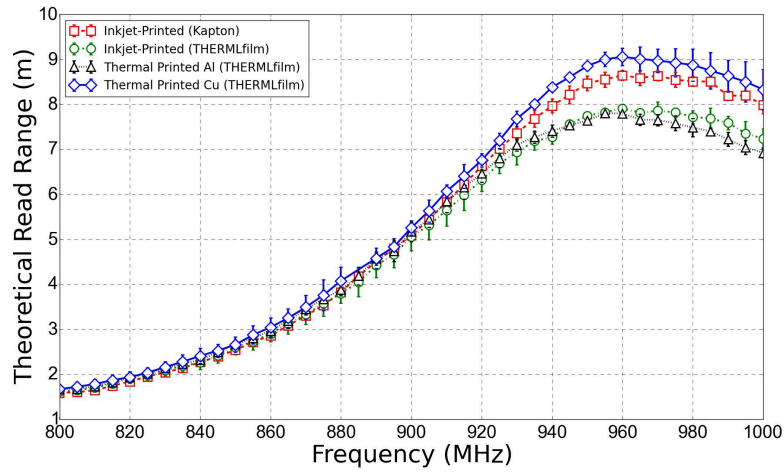


Figure 4.11: Measured theoretical reading range of tag design 2 fabricated by inkjet and thermal transfer printing methods [61]

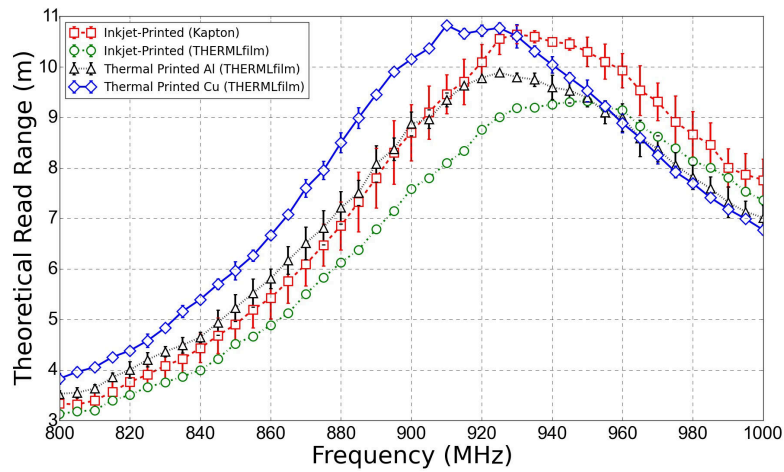


Figure 4.12: Measured theoretical reading range of tag design 3 fabricated by inkjet and thermal transfer printing methods [61]

lead to increased ohmic losses which can only be incorporated by measuring reading range of RFID tags. In such measurements, where all practical effects are included in the results, the thermal transfer printed labels outperform the inkjet printed labels by between 15-60 % compared to inkjet printing on THERMLfilm and up to 10 % on Kapton.

Table 4.3: Measured Theoretical Read Range [61]

Printing Method and substrate	Measured Theoretical Read range (m)		
	tag design 1 (940 MHz)	tag design 2 (960 MHz)	tag design 3 (920 MHz)
Thermal Transfer Printing (Al) THERMLfilm	4.4	7.7	9.8
Thermal Transfer Printing (Cu) THERMLfilm	6.6	9.0	10.6
Inkjet (Ag) THERMLfilm	4.2	7.9	9.2
Kapton	5.8	8.6	10.6

4.3 Chapter summary

In this Chapter, the thermal transfer printing (TTP) method was characterised for physical and electrical properties that influence the performance of printed electronics. The smallest feature size achieved by TTP is $155\ \mu\text{m}$ while the minimum gap size between prints attainable is $210\ \mu\text{m}$. Surface and line edge roughness for thermal transfer printing are $20\ \text{nm}$ and $10\ \mu\text{m}$ respectively. These feature sizes were achieved using a 300 dpi printer and are expected to be improved by use of higher resolution printers which are already available on the market. The aluminium and copper traces achieve sheet resistances of $0.15\ \Omega/\square$ and $0.08\ \Omega/\square$ respectively. High frequency characterisation of thermal transfer printed coplanar waveguides up to 10 GHz shows insertion losses of $1.0\ \text{dB}/\text{cm}$ and $1.4\ \text{dB}/\text{cm}$ for aluminium and copper prints respectively. The higher insertion losses of the copper prints at high frequencies are due to surface and edge roughness as well as cracks due to the prototypical material used. Thermal transfer printing was also benchmarked against inkjet printing, which is the most pervasive method of printing electronics, by means of RFID antenna read range. Our results indicate that thermal transfer printing using copper is able to equal or outperform inkjet printing with silver inks, regardless of whether the inkjet printing was conducted on the same substrate as the thermal printing, or on a substrate specially developed for inkjet printing. Our study used three different tag designs, representing antennas with a mix of thick and thin features to minimise the influence of a particular antenna geometry on the results. Across the three designs, the thermal transfer printed labels outperform the inkjet printed labels by between 15-60 % (1-10 %) compared to inkjet printing on THERMLfilm (Kapton). Therefore

our results indicate that TTP potentially has a role to play in printed electronics more generally.

Chapter 5

Application of Thermal Transfer Printing in Internet of Things

In this Chapter, the thermal transfer printing (TTP) method is studied as a viable low-cost fabrication method of antennas on flexible substrates. Rapid manufacture and prototyping of antennas is demonstrated by utilizing the speed of the TTP method for on-demand manufacture of antennas. A low cost frequency agile antenna produced by TTP is also designed, fabricated and characterised. An ultra-wideband (UWB) monopole antenna with operational bandwidth of up to 7.5 GHz is demonstrated and characterised under mechanical static bending conditions. This shows that thermal transfer printing can be used to fabricate electronics at microwave frequencies under a variety of deployment scenarios for IoT applications.

5.1 On-demand printing of antennas

The work presented in this Section has been published in [106] Kgwadi, M.; Vourch, C. J.; Harrison, D. J.; Drysdale, T. D., “On-demand printing of antennas for TV white-space communications,” *in Antennas and Propagation Conference (LAPC)*, 2014 Loughborough , vol., no., pp.553-556, 10-11 Nov. 2014 and is reproduced with permission from IEEE.

New communications bands are becoming available in the frequency range 300 MHz to 3 GHz, and in particular the 470-790 MHz band which was previously reserved for analogue terrestrial television (TV) transmissions [107]. Due to the attractive propagation characteristics at this frequency range, it is attractive for low power, low cost and short-range communications ideal for IoT applications. Thus it is conceivable

that it will be used for communications between nodes in ubiquitous computing networks and IoT. Opportunistic use of unused spectrum between licensed bands called TV white spaces (TVWS) has been proposed as one way of utilising this part of the spectrum. A consequence of this approach is that a user's frequency allocation will evolve both with their location and over time. This necessitates either designing a wide-bandwidth antenna with consequent cost, size, and efficiency compromises, or taking a new approach. The use of modern metallic thermal printing techniques [97] offer the prospect of low-cost antennas that can be printed on demand, at or near the point of use, with a design that is customised to suit the locally available TVWS communications bands.

Thermal transfer printing is an interesting method of producing electronics with benefits of low-cost and fast fabrication speeds. Unlike other methods for printing electronics like inkjet, gravure or screen printing, the printed samples can be used immediately with no requirement for curing/sintering. Direct image printing of TTP allows successive prints to be unique and thus cost effective for on-demand and/or rapid prototyping electronics.

5.1.1 Antenna design

A proof of concept demonstration using a meanderline monopole operating at 800 MHz was chosen due to its compact size and omnidirectional pattern. These are desirable characteristics for antennas in an ad-hoc network where the location of other communicating nodes are not known and can change over time. The meanderline has a total length of 187 mm ($\lambda/2$) while the overall antenna dimensions are 70 mm by 30 mm. The antenna was printed in less than 2 seconds using a Zebra S4M thermal printer of resolution 300 dpi and print rate 5 cm/sec. We used the IIMAK Metallograph aluminium conductive thermal transfer ribbon (CTTR) which results in metallisation thickness of 0.26 μm . The substrate used is Flexcon THERMLfilm Select 21944E (TC-390) which has a thickness of 72 μm and a relative dielectric constant (ϵ_r) of 3.2. Figure 5.1 shows the antenna, with the design and dimensions in Figure 5.1(a) and a photograph of the printed antenna with an SMA connector in Figure 5.1(b). The connection to the SMA connector was achieved via a conductive epoxy which required drying time of approximately 5 minutes.

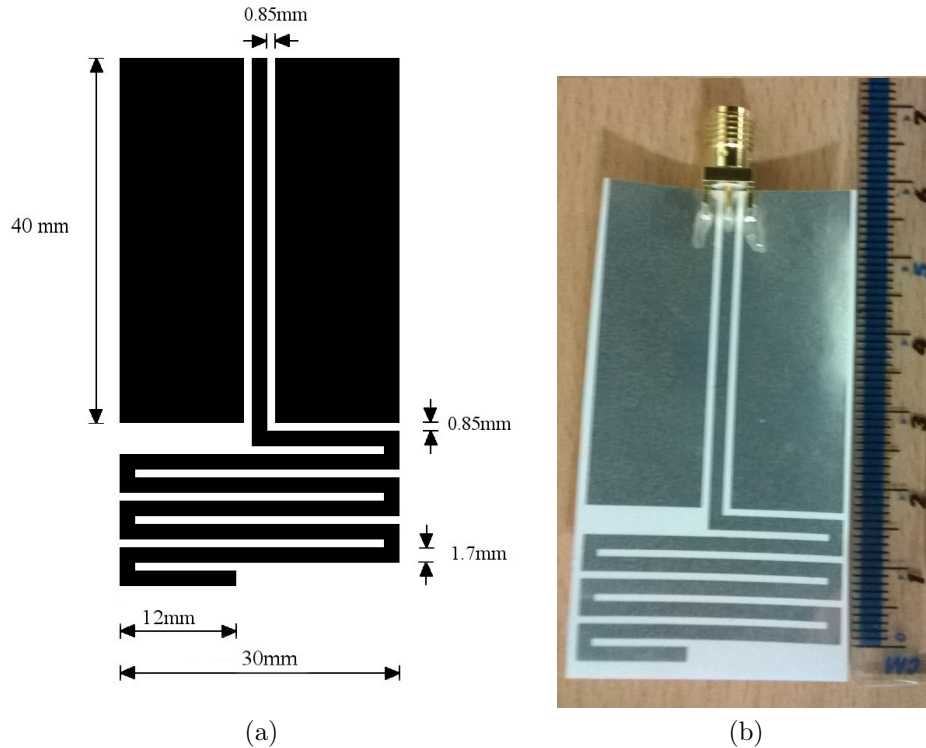


Figure 5.1: Monopole antenna geometry; (a) schematic and (b) photograph of printed antenna [106].

5.1.2 Simulation results and measurements

The antenna was designed and analysed using OpenEMS with metal modelled as a perfectly conductive layer of infinitesimal thickness to minimise the simulation times. The return losses were measured s_{11} using an Agilent E8362B PNA Network Analyser calibrated with an Agilent 85052B mechanical calibration kit. The measured and simulated s_{11} are plotted in Figure 5.7 and show good agreement, with the measured frequency (840 MHz, -37 dB) shifted slightly from the simulated value (820 MHz, -21 dB). This effect is due to the presence of a thin glassine release layer which preserves the adhesive on the substrate. The electrical properties of the glassine release layer are unknown and were not included in the simulations because in a practical deployment scenario, the glassine release should be removed. The measured fractional bandwidth below -10dB is 26%, compared to 8% for the simulation. The slight deviation from simulated and measured return losses is attributed to the SMA connector.

The radiation pattern of the monopole was measured using the NSI 2000 near

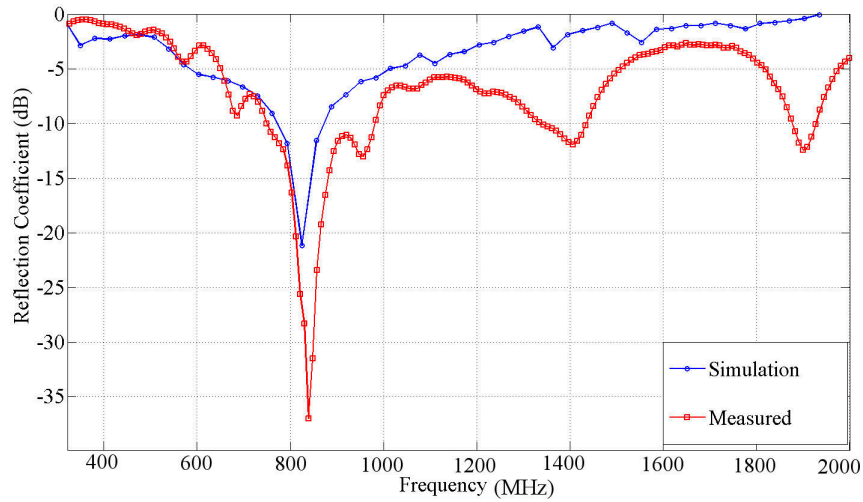


Figure 5.2: Measured and simulated reflection coefficient of antenna [106].

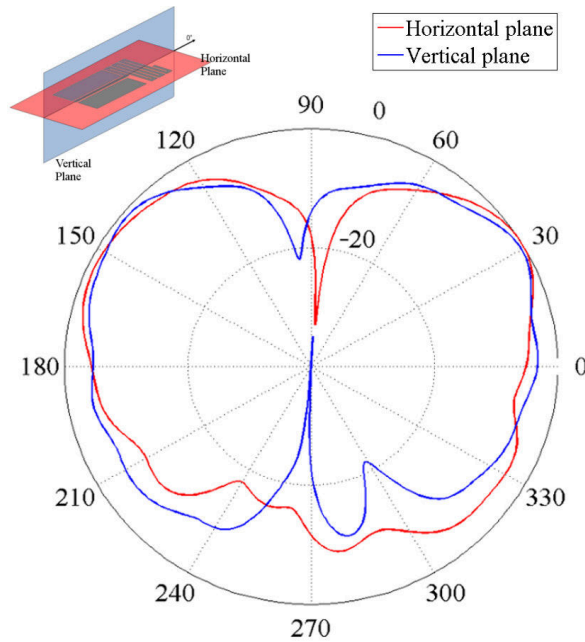


Figure 5.3: Polar plot of normalised measured radiation pattern in horizontal and vertical planes [106].

field spherical scanner in a $4.5 \times 4.5 \times 4.0 \text{ m}^3$ anechoic chamber and is shown in Figure 5.3. The farfield radiation pattern is omnidirectional and typical of a small monopole. The measured directivity is 4 dBi. The antenna shows low radiation efficiency, with a measured gain of -9.23 dBi, which we attribute to the thin metallisation ($0.26 \mu\text{m}$). At the operation frequency of 800 MHz, the skin depth on a conductor of $2.7 \times 10^7 \text{ S/m}$ (the measured conductivity of a thermally printed aluminium metalli-

sation for thermal transfer printing) is approximately $3.4 \mu\text{m}$. The insertion losses of coplanar waveguides raise exponentially as the thickness decreases below the skin depth [108] which lowers the efficiency and realised gain of the antenna. At these frequencies, the metallisation is 7.6% of the skin depth which results in high Ohmic losses and low radiation efficiency is expected.

5.1.3 Gain improvement

Low radiation efficiency is typical of low profile antennas [21, 109] due high conductor losses in the thin metallisation. There are several methods to improve gain in antennas with thin metallisation. In [109], the Authors demonstrate a method of increasing the radiation efficiency by stacking meander lines to achieve an improvement of 6 dB in antenna gain. That method could be employed in a straightforward manner using the thermal transfer printing method due to the speed and low-cost nature of the process although a via fabrication process would need to be developed to couple the multiple layers. The radiation properties of antennas are also affected by the antenna geometry as well [21] which provides an alternative optimisation parameter for the design to improve the efficiency and gain by use of either high conductivity ribbons, wider meander line and optimised geometry. The latter two techniques for gain improvement were explored since the thickness of the metallisation is fixed at $260 \mu\text{m}$.



Figure 5.4: The initial and improved monopole antennas [106]

To minimise the ohmic losses along the coplanar feed, which could be as high as 2.5 dB/cm [108] at 10% of the skin depth, the coplanar wave feed was shortened from 40 mm to 13 mm. The width of the meanderline was also increased from 1 mm to 4 mm to reduce the conductor losses. The gap between the ground planes and the centre strip of the CPW was 250 μm which was the smallest feature size that allowed consistent electrical isolation between the centre strip and the ground plane as discussed in Chapter 4. The geometry of the meanderline was also optimised through simulation. The antenna is shown in Figure 5.4 alongside the initial proof of concept design. The gain after the geometry optimisation is -3.9 dB, with a directivity of 4.3 dBi. Thus an improvement of 5.3 dB was achieved without employing the gain improvement techniques mentioned in [21] and [109]. Figure 5.5 shows the gain of the optimised antenna compared to the initial design, highlighting the improved gain of the optimised design. The use of thicker metal ribbons and multi-layered antenna gain optimisation described in [109] could also be employed to improve the gain even further.

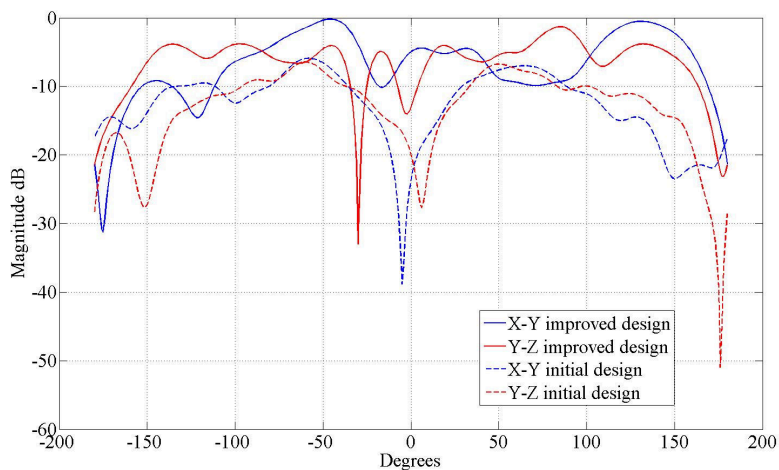


Figure 5.5: Far-field patterns of the initial and improved monopole antennas [106]

5.2 Low-cost reconfigurable antenna on flexible substrate

The work presented in this Section has been published in [110] Kgwadi, M., and Drysdale, T.D., “Diode-switched thermal-transfer printed antenna on flexible substrate”, *Electronics Letters*, 2016, and is reproduced here with permission from the Institution

of Engineering and Technology (IET).

It is reasonable to expect IoT devices to be able to handle dynamic frequency allocation, at least in part determined by regulatory authorities according to location [107] but also influenced by the local propagation environment favouring some channels over others due to fading mechanisms associated with building geometry [111] and other radio noise sources. Hence, reconfigurable antennas are attractive both for prototyping IoT communications networks in new locations, but also during deployment for responding to changes in the optimal channel choice. Cognitive radio also make reconfigurable antennas attractive to allow the radio to reconfigure the antenna when conditions require such action. Reconfigurable antennas can go further than frequency agility to include polarisation diversity [15] or beamforming capability [112]. Switching is known to introduce frequency [113] and polarisation [114] agility into planar antennas produced using conventional printed circuit board techniques on a variety of dielectric substrates. A thermal transfer printed frequency agile antenna for IoT applications was designed and characterised, demonstrating the feasibility of TTP in incorporating other circuit elements.

5.2.1 Antenna design and implementation

A sequentially reconfigurable frequency agile Sierpinski antenna using RF microelectromechanical systems (RF MEMS) switches was achieved in [115]. The RF MEMS in [115] require DC bias voltage of up to 17 V to achieve switching. The use of high voltage may not be cost effective or possible in low power sensor nodes which often use small capacity, low voltage batteries. Therefore PIN diodes are an attractive alternative for a low cost IoT approach because they can be switched with voltages lower than 1 V DC (nominal value 0.95 V) [116]. A thermal transfer printed agile Sierpinski gasket-based tunable antenna using NXP semiconductor's general purpose PIN diodes (BAP50-03) as switches was designed to demonstrate the compatibility of TTP with circuit components. The design allows a sensor node to switch between ISM band (2400 MHz) communications and the television white space (TVWS) bands centered at (800 MHz). Thus an associated sensor node could switch between the two frequency bands depending on availability and/or network traffic conditions.

Figure 5.6(a) shows a schematic of our design, with a photograph of the final

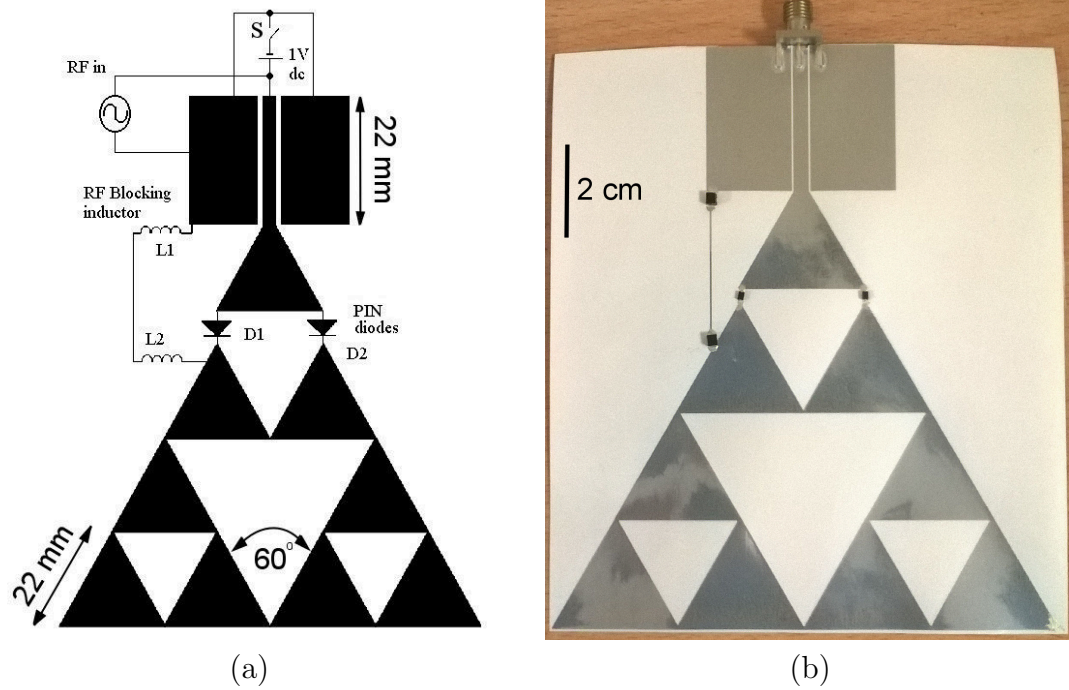
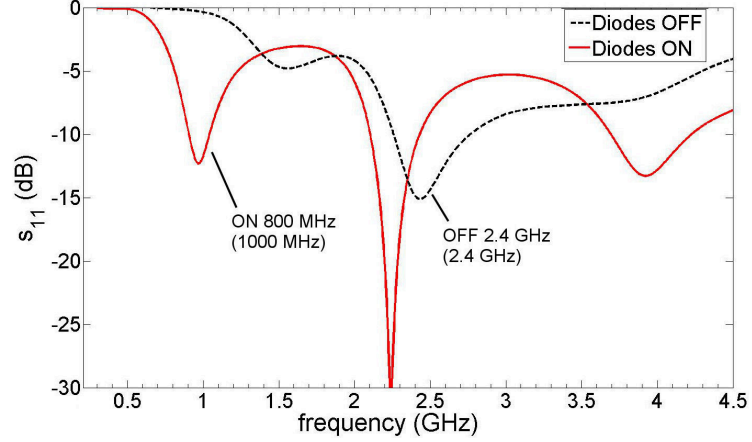
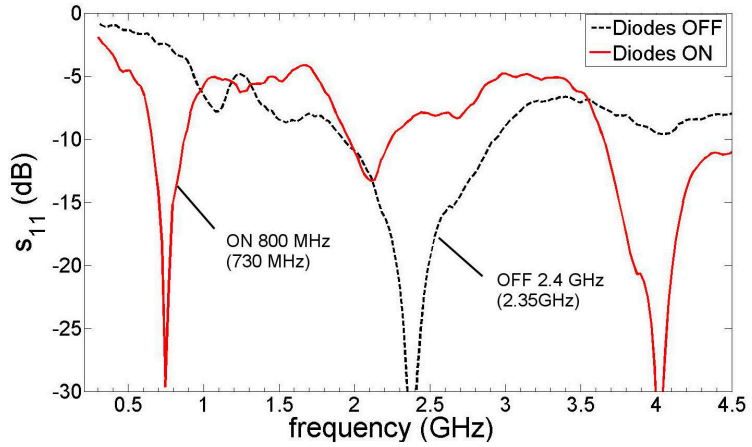


Figure 5.6: Schematic (a) of the reconfigurable Sierpinski antenna (dimensions: CPW center strip 3.2 mm, CPW gap 0.35 mm, CPW ground width 18 mm) and picture (b) of the fabricated antenna [110].

printed version shown in Figure 5.6(b). The antenna is switched between the ‘ON’ and ‘OFF’ state by switch S , via a voltage supply fed through the vector network analyser DC-bias port. On a microcontroller-based sensor node, the same operation can be achieved by programming one of the output pins. For a 3.3 V output pin voltage, a $47\ \Omega$ resistor in series with the PIN diode will be required obtain the required forward bias current of 50 mA. In the ‘ON’ state the diodes are forward biased and the whole of the antenna is in operation, resonating at 800 MHz. In the ‘OFF’ state the diodes are at zero bias and the antenna elements beyond the cathodes of the diodes are effectively disconnected, yielding a short antenna structure that resonates at 2400 MHz. In practice, some residual loading remains because the diode is not a perfect open circuit. Two surface-mount inductors are used to isolate the RF signal from the ground shown by L1 and L2 in Figure 5.6.



(a)



(b)

Figure 5.7: Plots of S_{11} parameter for the (a) simulated and (b) measured antennas, for the diodes ON and OFF. With the diodes OFF, operation is at 2.4 GHz and ON at 800 MHz (larger effective structure size) [110].

5.2.2 Simulation results and measurements

The antenna was simulated in OpenEMS with the metallisation modelled as a perfect electrical conductor of infinitesimal thickness to obtain reasonable simulation times. This does not affect the radiation pattern or operating frequency but prevents accurate prediction of the efficiency. Lumped components were used to model the PIN diodes and inductors in the simulations. The reverse bias capacitance of the diodes was modelled as a 0.4 pF lumped capacitor in the ‘OFF’ state, while the forward bias resistance was modelled as a 3Ω lumped resistor in the ‘ON’ state. The inductor was modelled as lumped $4.7\mu\text{H}$ inductance in series with a 3Ω resistance. Figure 5.7(a) shows the simulated reflection coefficient in the two cases when the diodes are ‘ON’ and ‘OFF’. Figure 5.7(b) shows the measured S_{11} , with the desired resonance in

the ISM band (WLAN, 2400-2500 MHz) with an S_{11} better than -30 dB through the entire band and no resonance at 800 MHz in the ‘OFF’ state. In the ‘ON’ state, the resonance in UHF band is observed at 730 MHz with an S_{11} of -28 dB and operational bandwidth of 200 MHz ($S_{11} \leq -10$ dB). The 150 MHz shift in the resonance frequency between simulation and measurements is attributed to discretization of the diagonal lines into a staircase approximation and the presence of a 56 μm thick glassine liner which preserves the acrylic adhesive and thus makes the structure electrically larger than simulated (hence the resonances shifts to the lower frequencies)

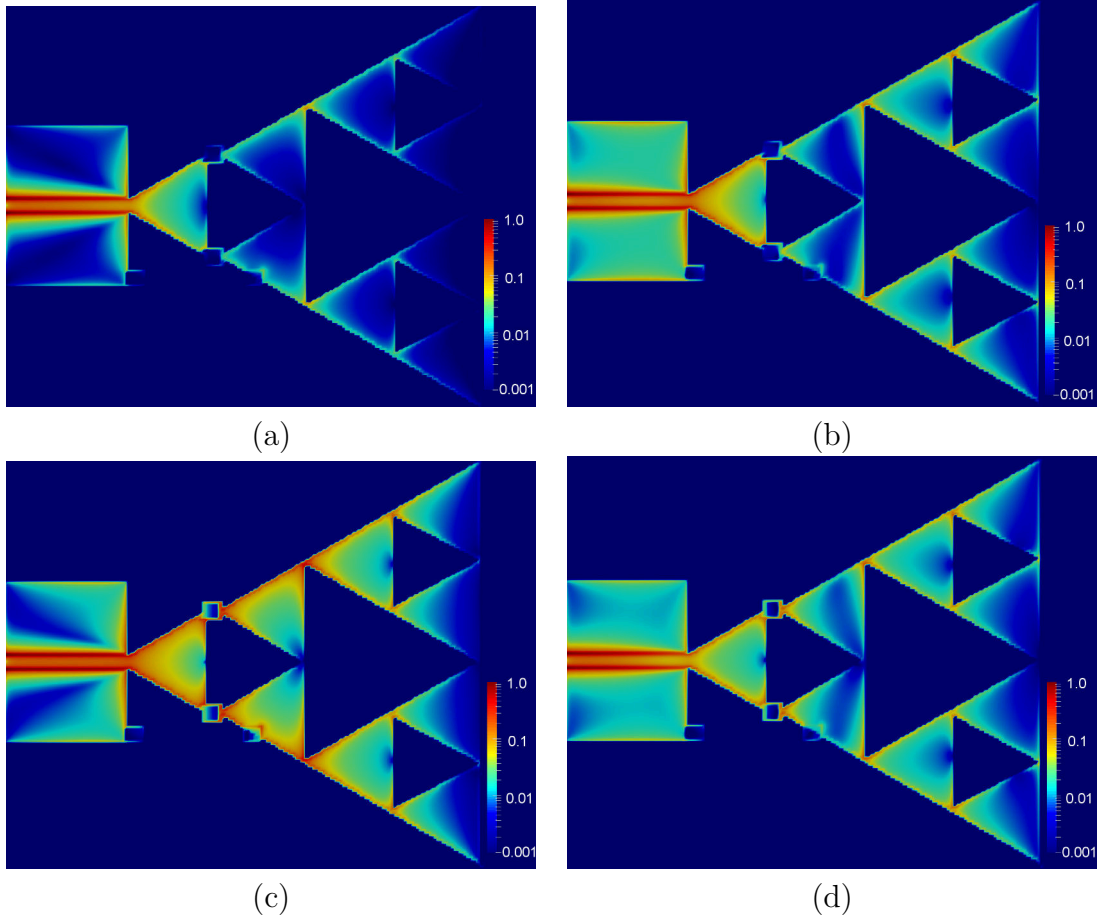


Figure 5.8: Simulated normalised current densities, (a) at 800 MHz in the ‘OFF’ state, (b) 2400 MHz in the ‘OFF’ state, (c) 800 MHz in the ‘ON’ state , and (d) 2400 MHz in the ‘ON’ state [110].

Figure 5.8 shows the normalised surface current distribution in both ‘ON’ and ‘OFF’ cases at the two design frequencies. In the ‘OFF’ state the current density at 800 MHz is limited to the lower part of the antenna as shown in Figure 5.8(a). The current distribution at 2400 MHz shown Figure 5.8(b) shows a higher intensity in the

active part of the antenna compared to 800 MHz in Figure 5.8(a) signifying resonance. Some currents also appear on the inactive part of the antenna in the ‘OFF’ state, due to fringing capacitance. In the ‘ON’ state, the 800 MHz current is distributed through out the whole antenna as shown in Figure 5.8(c) and shows higher intensity than in the ‘OFF’ state. This shows the antenna resonating at 800 MHz in the ‘ON’ state. Figure 5.8(d) shows the current distribution at 2400 MHz.

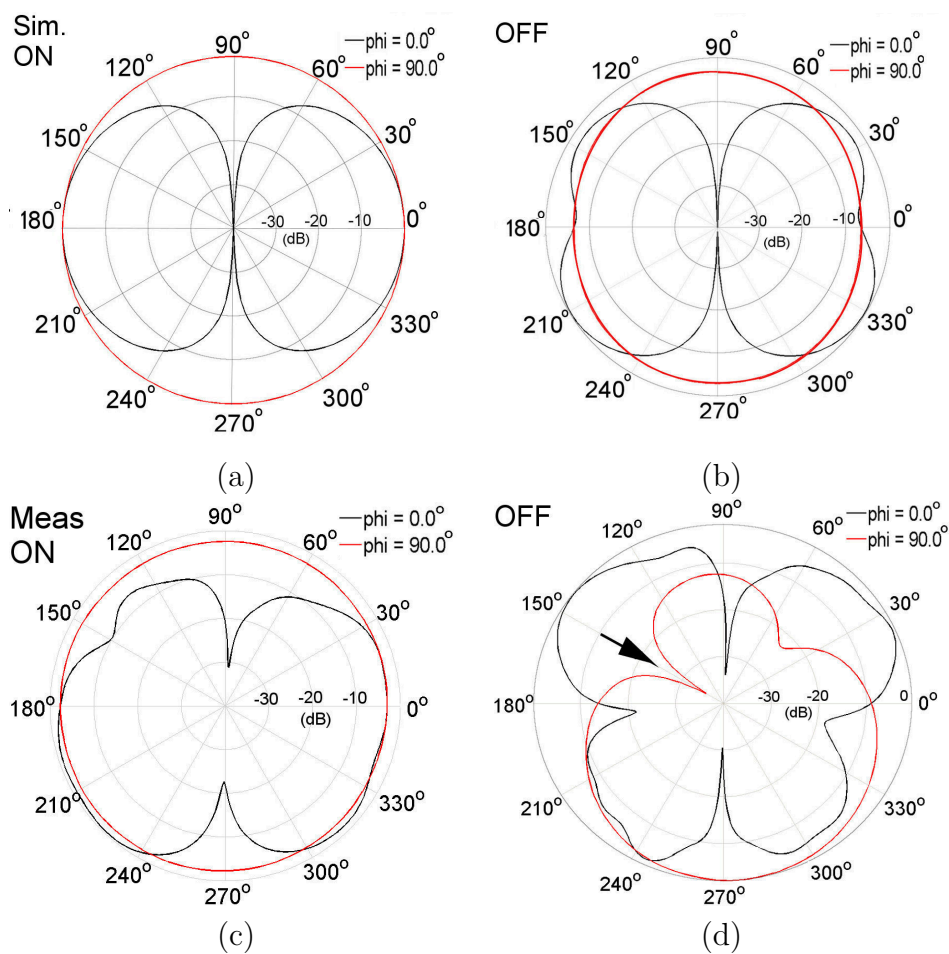


Figure 5.9: Simulated and measured radiation patterns. (a) simulated radiation pattern at 800 MHz in the ‘ON’ state and (b) simulated radiation patterns at 2400 MHz in the ‘OFF’ state; (c) corresponding measured radiation pattern in the ‘ON’ state at 800 MHz and (d) measured radiation pattern in the ‘OFF’ state at 2400 MHz. The arrow marks a null caused by the bias line [110].

The radiation pattern was measured using an NSI 2000 near field spherical scanner described previously in Chapter 3. The normalised simulated far-field radiation patterns for 800 MHz (‘ON’) and 2400 MHz (‘OFF’) are shown in Figure 5.9(a) and Figure 5.9(b) respectively. The corresponding normalised measured far-field radiation patterns at 800 MHz (‘ON’) and 2400 MHz (‘OFF’) are shown in Figure 5.9(c)

and Figure 5.9(d) respectively. The measured radiation patterns in the ‘ON’ state are omnidirectional with a measured gain of -5.3 dBi and a directivity of 3.1 dBi at 800 MHz. The low measured gain is attributed to the conductor losses due to thin metallization (0.07 of the skin depth) typical of printed antennas [21] and losses in the resistances of the forward biased PIN diodes and RF blocking inductors. The radiation pattern is however consistent with the simulated radiation pattern in Figure 5.9(a). The measured radiation pattern at 2400 MHz (‘OFF’) shows omnidirectional radiation pattern as shown in Figure 5.9(d), with a measured gain of 6.7 dB and directivity of 5.2 dB. There is an unexpected null in the measured pattern in the E-Plane at 150° which we attribute to the presence of bias line of length 2 cm which is significant compared to the wavelength at 2400 MHz (0.16λ) although this is of negligible consequence at 800 MHz (0.05λ).

5.3 Compact ultra-wideband antenna on flexible substrate

The IEEE 802.15.3a channel which covers 3.1 GHz to 10.6 GHz has been allocated for short-range, low power communications by the Federal communications commission (FCC). The available total bandwidth (7.5 GHz) allows up to 1 Mbs data-rates making the channel attractive for wireless personal area networks (WPAN) and wireless sensor networks (WSN) [117, 118]. The FCC limits the effective radiated power to a maximum of -41 dB/MHz [119] within this channel which is necessary for co-existence with other licenced users. These power level constraints make the IEEE 802.15.3a suitable for low power, short range indoor communication applications. The higher frequencies of the IEEE 802.15.3a channel allows for compact antenna designs suitable for unobtrusive incorporation into wearables, smart labels, and sensors compared to UHF frequencies. There have been several studies to improve the IEEE 802.15.3a channel characteristics including multiple-input-multiple-output (MIMO) solutions [42, 120] to mitigate multipath, shadowing effects, low-power constraints and increase channel capacity. It is therefore conceivable that the IEEE 802.15.3a will play a role in the IoT. Thermal transfer printed flexible and conformal electronics are well suited for unobtrusive integration either worn directly on the skin or are placed on clothing and are thus expected to be deployed under mechanical stress. Mechanical stress caused by bending is known to affect performance of flexible electronics [121] and these effects on thermal transfer printed electronics are yet to be

determined. The effects of static mechanical bending on thermal transfer printed antennas is studied subsequently.

5.3.1 Compact UWB antenna design

A compact coplanar-fed monopole antenna based on a design in [122] was designed and optimised using OpenEMS for operation in the IEEE 802.15.13a range (3.1 - 10.6 GHz). The optimized dimensions (in millimetres) of the UWB monopole design are shown in Figure 5.10(a). The coplanar gap was kept at the minimum achievable gap of $250\ \mu\text{m}$. The antenna was thermal transfer printed on THERMIfilm using the aluminium CTTR with printer settings as previously discussed in Chapter 3. A photograph of the printed antennas with an SMA connectors attached is shown in Figure 5.10(b). The overall dimensions of the antenna and the SMA connector are 44 mm by 32 mm. A photograph thermal transfer printed antennas with SMA connectors attached is shown in Figure 5.10(b) under different mechanical bending scenarios.

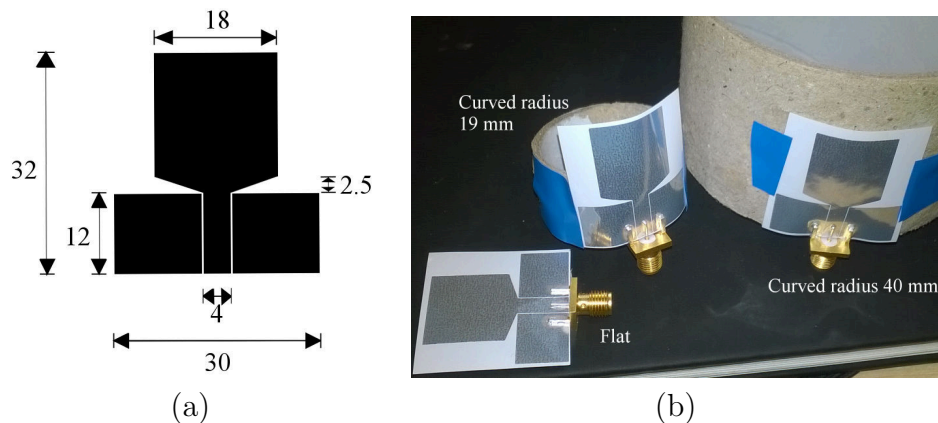


Figure 5.10: A compact ultra-wideband monopole (a) schematic (all dimensions in mm) and (b) TTP printed antennas with SMA connectors under varying degrees of mechanical bending scenarios.

5.3.2 Experimental results

The most anticipated deployment of flexible antennas are under mechanical static-bending where an antenna is attached to an object as a label or worn on a quasi-static part of the body. It is difficult to envisage an application where an antenna would be subject to repetitive mechanical bending which warrants dynamic-bending test. Thus, the static bend is sufficient for characterising thermal transfer printed antennas

under mechanical stress. To determine the performance of thermal transfer printed antenna under different mechanical static-bending conditions, the antenna was subjected to three possible deployment scenarios where the antenna has to conform to the shape of an object and/or person wearing it. In the first scenario, the antenna is flat with no mechanical bending while the in other two scenarios, the antenna was attached to cylinders with radii 19 mm and 40 mm as shown in Figure 5.10(b).

The antennas shows ultra-wideband performance covering the entire IEEE 802.13a frequency range. The measured return losses of the flat antenna are below -10 dB from 2.8 GHz to 11.0 GHz as shown by the solid black line in Figure 5.11 and matches well with the simulation results. Simulations were performed for the flat case only. The measured fractional bandwidth of the monopole is 122%. The antenna with the 40 mm radius of curvature experiences a reduction in the bandwidth with the return losses below -10 dB from 3.1 GHz to 9.5 GHz. The performance is still broadband with only 1 GHz of bandwidth difference from the flat deployment scenario. The total available bandwidth due to mechanical flexing of the antenna is 85% of the total bandwidth in the IEEE 802.13a band. As the radius of curvature is reduced to 19 mm the bandwidth is reduced even further from 3.5 GHz to 8.8 GHz. The total available bandwidth however is still 5.3 GHz which is 70% of the total bandwidth in the IEEE 802.13a band.

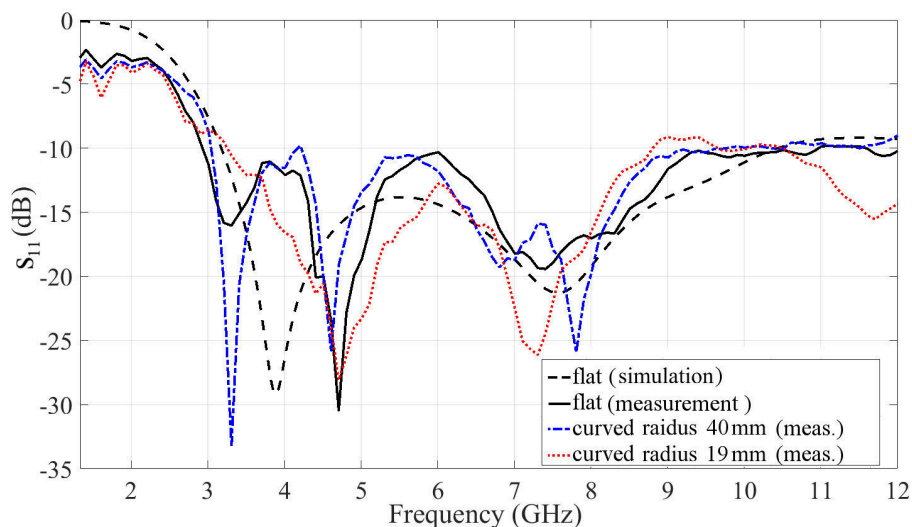


Figure 5.11: Return losses of the printed antenna under different mechanical flexing conditions.

The measured E-plane far-field radiation patterns for selected frequencies in the IEEE 802.15.3a band are shown in Figure 5.12 along with the simulated radiation pat-

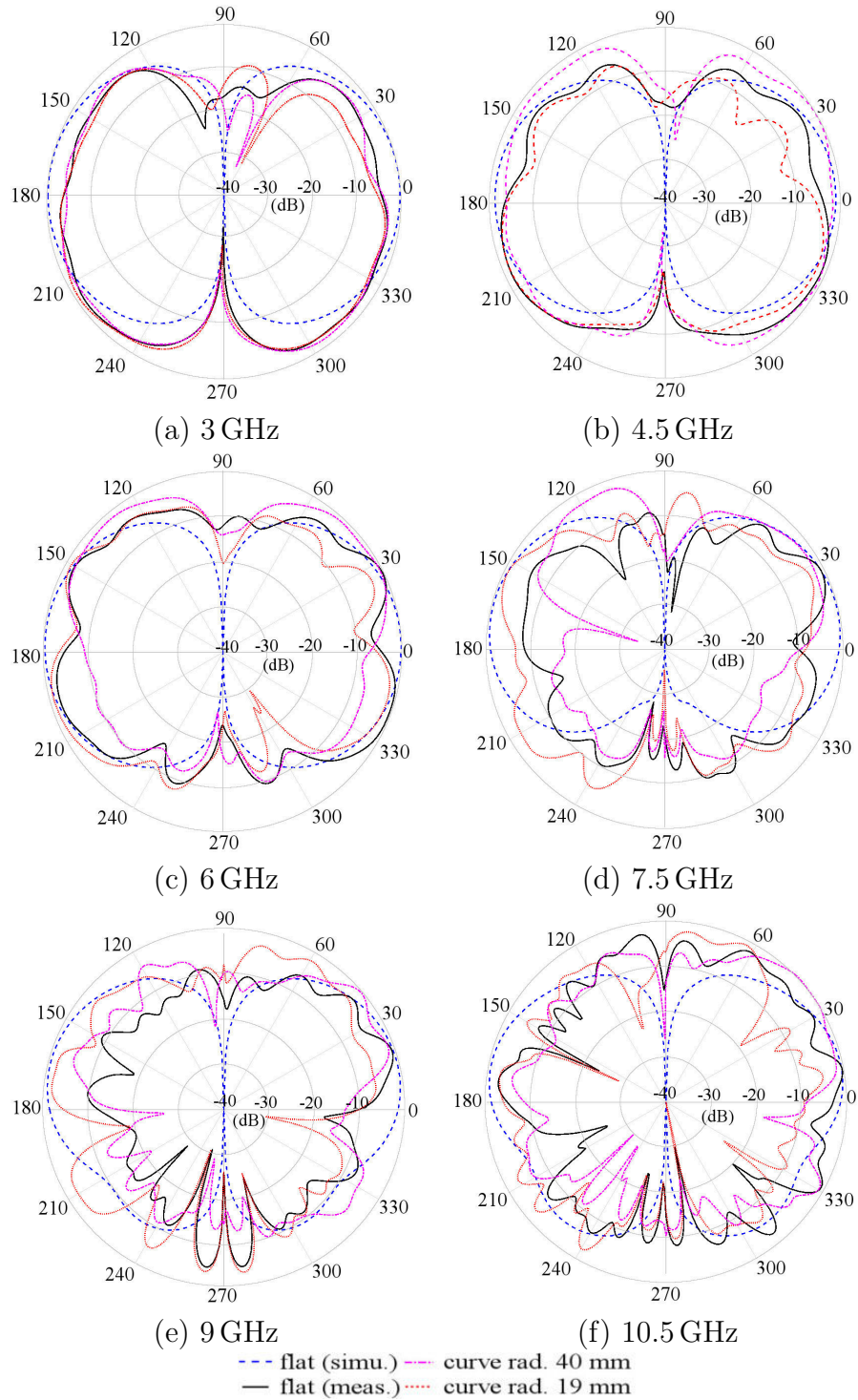


Figure 5.12: Normalised simulated and measured far-field (E-plane) radiation pattern for the compact UWB monopole under different static mechanical flexing conditions at select frequencies in the IEEE 802.15.3a band; (a) 3.0 GHz, (b) 4.5 GHz, (c) 6.0 GHz, (d) 7.5 GHz, (e) 9.0 GHz, and (f) 10.5 GHz.

terns. The radiation pattern shows omni-directional radiation and matches well with the simulated pattern for the frequencies up to 6 GHz for all the different mechanical bending scenarios. The radiation pattern of the antenna under 40 mm radius of curvature bend closely follows the flat radiation pattern due to the small difference in curvature from the flat deployment scenario. The smaller radius of curvature shows more deviation from the simulated pattern and the measured flat deployment scenario. Above 6 GHz, the radiation pattern diverges from theory due to the influence of the SMA connector whose dimension ($1\text{ cm} \times 1\text{ cm}$) become significant compared to the wavelength (5 cm). Thus as the wavelength gets short with higher frequency, the effect of the SMA connector on the radiation pattern becomes significant as shown by radiation patterns for 7.5, 9.0 and 10.5 GHz. The overall radiation pattern is however still omnidirectional and in an application setting, the SMA connector would be eliminated by directly bonding the communication modules to the antenna.

5.4 Chapter summary

In this Chapter, application of the thermal transfer printing method in fabricating IoT antennas was demonstrated. Exploiting the speed, low-cost and direct printing of thermal transfer printing, on-demand printing of highly custom antenna designs and or prototyping can be performed. TTP was also demonstrated capable of producing reconfigurable antenna using low-cost off the shelf components. Demonstrating that thermal transfer printing can be combined with switching elements (or any other circuit elements e.g. light emitting diodes, transistors, microprocessors) to make low-cost, flexible, reconfigurable antennas and in general, low cost flexible electronics in a very short time. An ultra-wideband, flexible antenna ideal for short-range, high datarate communications was also fabricated and characterised under varying degrees of static mechanical bend. The thermal transfer printed UWB antenna maintained UWB characteristics and minimal radiation pattern deviations under acute static mechanical bend (4 mm radius bending). This demonstrates that TTP can be used in large area electronics to produce low-cost, flexible electronics on renewable substrates.

Chapter 6

Slot-ring Multi-port Driven Antenna for Integration with RTD Oscillators

This Chapter presents a study of a slot-ring multi-port driven (MPD) antenna for the purposes of integration with resonant tunnelling diode oscillators. The slot-ring antenna is described and then the geometry is optimised to improve air-side radiation and reduce lateral radiation on electrically thick substrates. Validation of the design is experimentally verified at 5 GHz. The work presented in this Chapter has been published in [123] Kgwadi, M., Alharbi, K., Wang, J., Wasige, E.; “Slot-Ring Multiport Driven Antenna with Improved Airside Radiation for Terahertz Communications,” *European Microwave Week (EuMC)*, London, 3-7 October 2016. and is reproduced in part with permission from the publishers.

6.1 Analysis of slot-ring antenna

The slot-ring MPD antenna is a complementary structure of the ring MPD travelling wave radiator described in Chapter 2. Slot antennas less complex geometry which simplifies fabrication by minimising the number of metal layers during fabrication thereby lowering costs. For this reason, the state of the art integrated antennas with RTD oscillators use slotted geometries [37, 84, 85]. Unlike other single-port antennas, multi-port driven antennas allow power combining from multiple sources on a single antenna structure [43] allowing for compact integrated designs and in the process eliminating losses associated with transmission lines and/or matching networks.

Power combining capabilities by the antenna structure is an attractive property for an integrated solution due to the low power output of RTD oscillators where the target output power of 10 mW is realistically going to be achieved by more than one oscillator. In an MPD, multiple oscillators can be coupled to a single power combining antenna in a similar way as [43] where up to 8 sources were driving a single antenna. A slot-ring antenna for 135 GHz operation on a $250 \mu\text{m}$ silicon substrate, (0.41λ) was presented in [44] with less complicated fabrication process than the equivalent ring and spoke geometry.

The slot-ring antenna is a complementary structure of the microstrip annular ring antenna. The modes in a microstrip annular ring antenna have been studied in the literature [124–127] and the modes are shown to be TM. The dominant mode for the annular microstrip ring antennas is the TM_{11} and results in non-zero far-field radiation patterns at boresight. High-order modes result in nulls at boresight [127] and are not considered in this thesis. Since the annular slot-ring is a complementary structure, the slot cavity has the electric field reversed to the magnetic field resulting in TE modes.

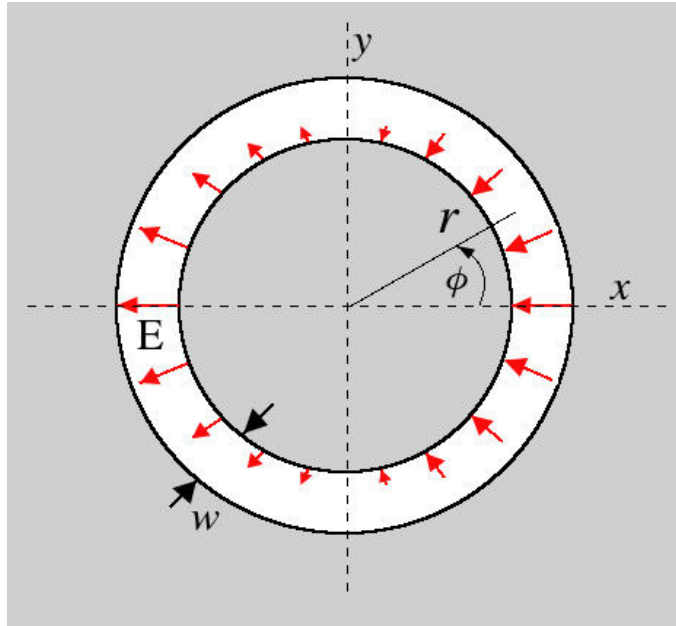


Figure 6.1: Electric field distribution of the first resonance in an annular slot-ring antenna.

Consider an annular slot-ring antenna lying on the x - y plane as shown in Figure 6.1 with an average circumference equal to the guided wavelength λ_g . The instantaneous electric field distribution along the slot is thus sinusoidal with virtual shorts along

the y -axis shown by the arrows in the Figure. The electric field is transverse to the direction of propagation and thus the dominant radiating mode is a TE wave. If the slot width w is much smaller than the guided wavelength ($w \ll \lambda_g$) such that the electric field only has azimuthal variation, the slot-ring can then be viewed as a magnetic current loop with a current distribution [128];

$$M(\phi) = M_o \cos(k_g r \phi) \quad (6.1)$$

where k_g is the phase constant in the slot and r is the radius of the slot and ϕ is the angular measurement from the x -axis. For a dual port slot-ring antenna with phase differential equal to the propagation delay between the feeding points, the resulting electric field propagates along the slot creating radiation.

The far-field radiation pattern can be calculated by the Hankel transform of the magnetic current distribution in the slot [129]. The far-field electric field of the annular slot-ring is thus given by [128];

$$E_\theta(\theta, \phi) \simeq J'_1(k_e r \cdot \sin(\theta)) \cdot \sin(\phi) \quad (6.2)$$

$$E_\phi(\theta, \phi) \simeq \frac{J_1(k_e r \cdot \sin(\theta))}{k_e r \cdot \sin(\theta)} \cdot \cos(\theta) \cdot \cos(\phi) \quad (6.3)$$

where $k_e = k_d = 2\pi/\lambda_d$ for the dielectric side or $k_e = k_o = 2\pi/\lambda_o$, and $J_1(x)$ is the first order Bessel function of the first kind and J'_1 denotes its first derivative.

6.2 Slot-ring multiport driven antenna on electrically thick substrate

The effects of electrically thick substrate ($\geq 0.41\lambda$) on the slot-ring antenna are yet to be established and these are investigated in this Chapter to determine their effect on the performance of the slot-ring MPD. Electrically thick substrates (thicker than a quarter wavelength) are known to support numerous substrate modes which confine the energy within the substrate, and thus reducing their radiation efficiency [39]. Moreover, these substrate modes interfere with the radiated energy when they exit the sides of the substrate causing undesired lateral radiations and side lobes. In some cases, the substrates cannot be thinned due to materials used, manufacturing and packaging constraints. Some substrates such as indium phosphide (InP) on which the RTD epitaxial layers are grown are extremely fragile, making thinning the sub-

strate a difficult process.

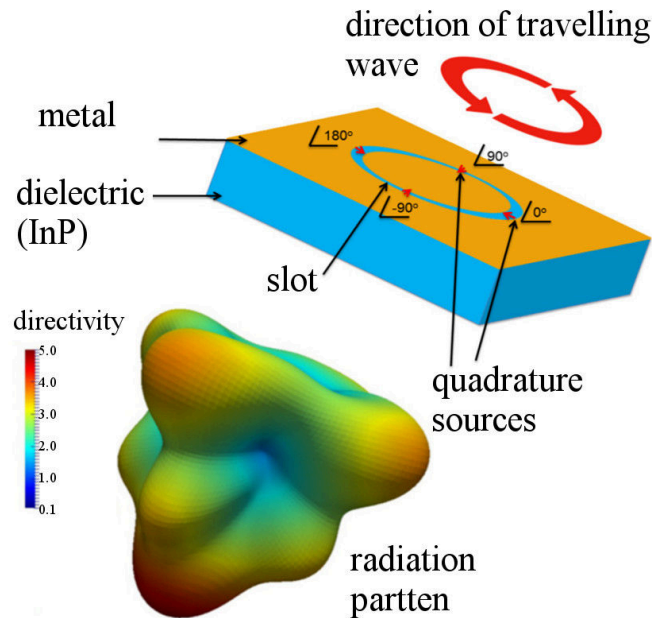


Figure 6.2: Radiation pattern of a MPD slot-ring on an electrically thick substrate

A 300GHz slot-ring MPD antenna was designed using the criteria described in Chapter 2 and simulated in OpenEMS to investigate the effects of electrically thick substrates on the radiation pattern. The designed slot ring has a radius of $45\ \mu\text{m}$ ($g = 1$ at 300GHz), a slot aperture of $5\ \mu\text{m}$, while the substrate dimensions are $1000 \times 1000 \times 635\ \mu\text{m}$. Four sources separated by a quarter wavelength were placed along the slot ring and driven with a quarter period delay (quadrature driven) from each other as shown in Figure 6.2. The resulting radiation pattern of the slot-ring is shown as well in Figure 6.2 and the effects of an electrically thick substrate are evident by the backward and lateral radiation. The radiated energy is on the back-side of the substrate as is was the case in [43] but with significant lateral radiation due to a thicker substrate. The electrically thick substrate supports more substrate modes which exit the substrate at the edges and cause lateral radiation which is also emphasized at the corners of the substrate. Due to the fragile characteristics of InP, thinning the substrate is not feasible and this necessitates a different approach to improve airside radiation.

6.3 Air-side radiation improvement

The low power output of RTD oscillators requires efficient antennas to achieve reasonable communicating and/or imaging distances. Highly directive antennas are also desirable in millimetre-wave bands to counter the effects of attenuation. To adopt the MPD slot-ring antenna for integration with RTD oscillators, the undesirable radiation characteristics have to be improved. The improvements made on the initial design in this Thesis are to address; 1) air-side radiation, and 2) minimise lateral radiation at the edges of the substrate. This was achieved by modifying the geometry of the outer ground plane from a square that covers the entire face of the substrate to a circle. An additional ground plane placed on the backside of the substrates acts as a reflective plane and refocuses the energy that would otherwise propagate downwards into the substrate upwards in to the airside. A similar backing ground plane on a ring and spoke MPD was shown in [43] uses a ground plane on the backside of the substrate. The solution in [43] however places a quarter wavelength substrate thickness requirement to guarantee coherent integration of the waves reflected from the ground for effective radiation. In this Thesis a 2.25λ (9 quarter wavelengths) thick substrate is used which is the standard thickness of the InP wafer on which RTD oscillators are grown. An odd number of quarter wavelengths is sufficient to ensure that the reflected waves do not add up destructively with the incident wave on the backing ground plane. A similar solution was demonstrated using diced bow-tie antennas on a large backing ground plane in [86] where the ground plane was used to refocus the energy to the airside.

Figure 6.3(b) shows the modified slot-ring MPD antenna. A circular outer ground plane minimizes the lateral radiation by allowing a purer circular travelling wave around the outer ground plane as shown in Figure 6.4 without corners which result in undesired radiation. Figure 6.3(b) shows the radiation pattern and directivity of the improved structure. There is an improvement on the directivity from 7.9 dBi to 10.8 dBi (approximately a 3 dB increase) and the radiation is directed to the air-side.

6.4 Optimisation of modified slot-ring MPD

The initial results suggest that there should be an optimal size for the outer ground between the smallest value (thin loop surrounding the slot) to the maximum (covering

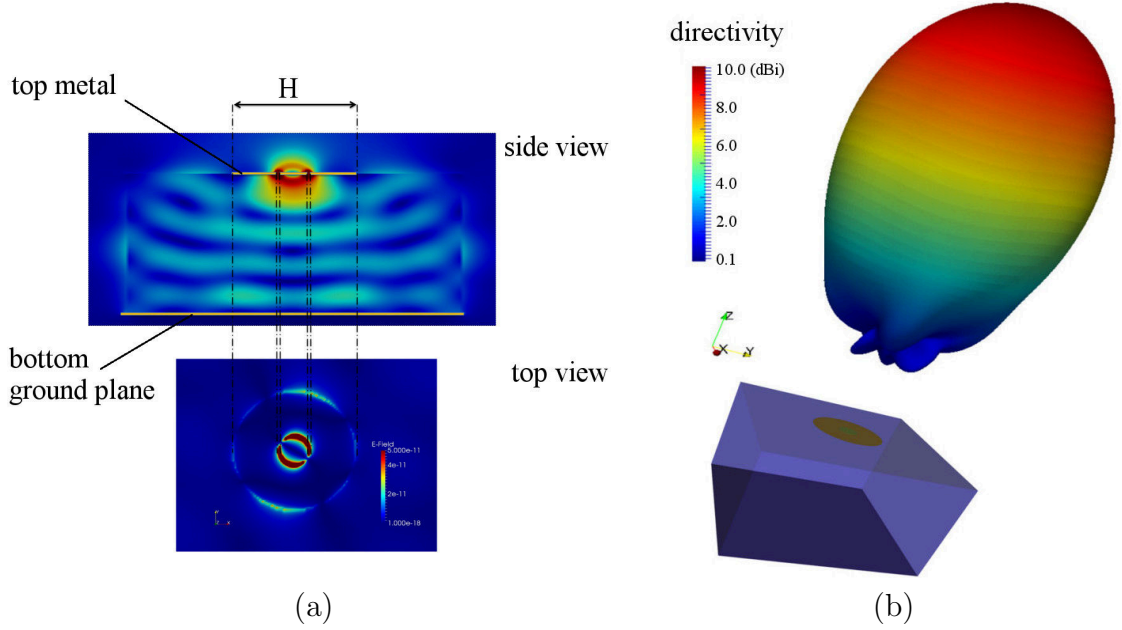


Figure 6.3: MPD slot ring with backing ground plane for improved air-side radiation. (a) side and topview showing the propagation of energy within the structure and (b) the resulting far field radiation pattern

the entire top surface). The geometry of the modified slot-ring MPD was varied in discrete steps to obtain the maximum directivity. To keep a nomenclature consistent with one used in Chapter 2 and for a general solution, define $H = 2\pi R_g/\lambda_g$ as the ratio of the circumference of the outer ground plane to the guided wavelength, where R_g is the radius of the outer ground plane and λ_g is the guided wavelength. An optimisation criteria was then to maximise the directivity by varying R_g and subsequently $H \in (1, N]$, where N is limited by the total area of the antenna which was limited to $1000 \times 1000 \mu\text{m}^2$.

Simulations of the structure at discrete values of the outer ground plane were performed and the directivity was observed. A selection of normalised far-field radiation patterns for ground sizes of $H=2, 4, 6, 8,$ and 10 are shown in Figure 6.5. Figure 6.6 shows the dependence of directivity on the size of the outer ground plane. The directivity increases as the size of the outer ground plane is increased from the initial value of 8.60 dBi at $H=2$ and achieves a maximum value of 10.9 dBi at $H=4$ and reduces to a value of 6.4 dBi at $H=6$. This suggests that the optimum outer ground radius for maximum directivity is approximately $R_g = 4\lambda_g/2\pi$.

The front-to-back lobe ratio also shows a dependence on the size of the outer ground plane as shown by Figure 6.7. The modified slot-ring MPD shows a good

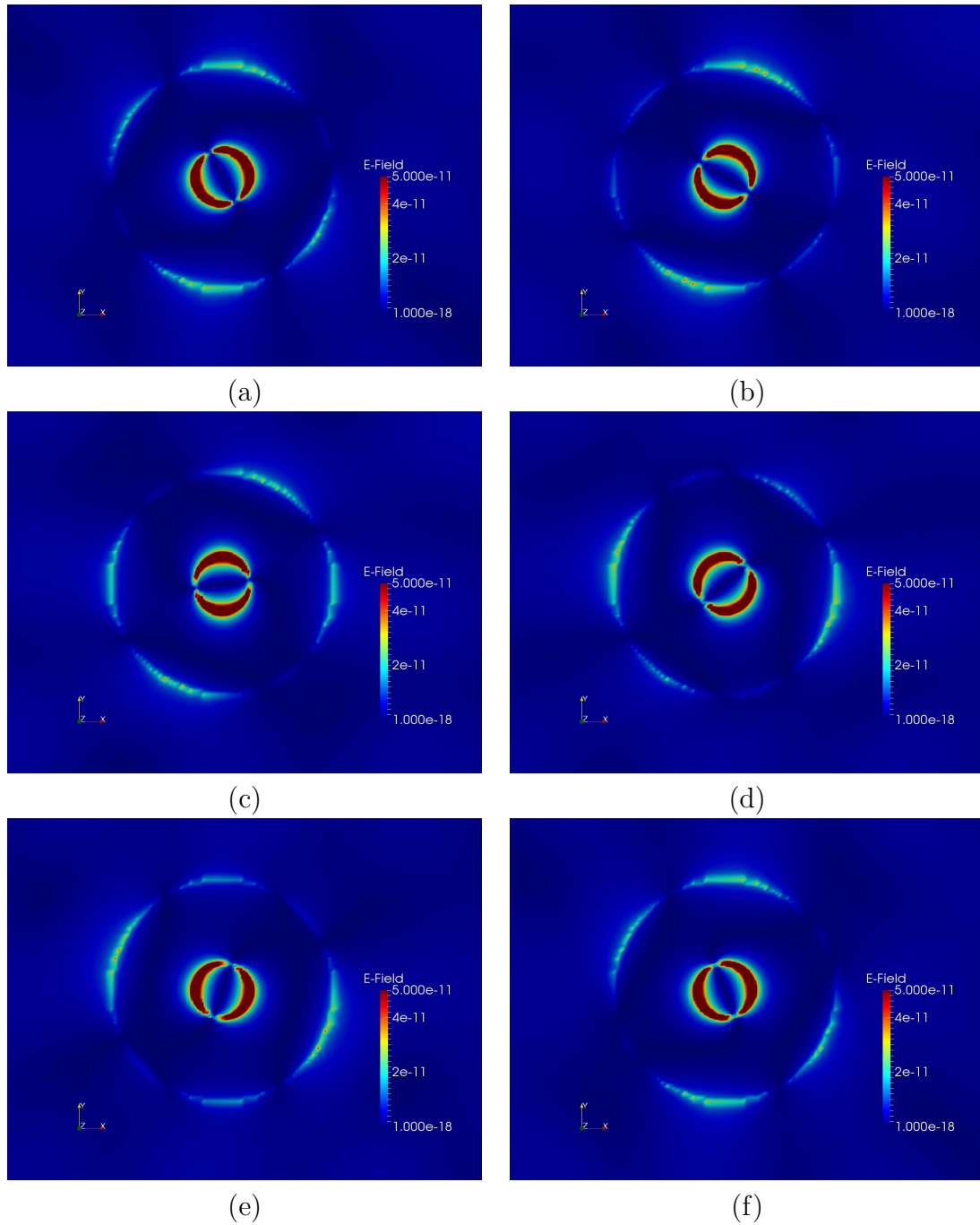


Figure 6.4: Simulated electric field distribution showing the circularly polarised travelling wave within the modified slot-ring MPD at consecutive timesteps, (a) $t=0$, (b) $t=2$, (c) $t=4$, (d) $t=6$, (e) $t=8$, and (f) $t=10$.

front-to-back lobe ratio of between 13 dBi and 14.8 dBi in the range $H \in [2, 5]$ beyond which a significant part of the radiation is directed to the back and laterally.

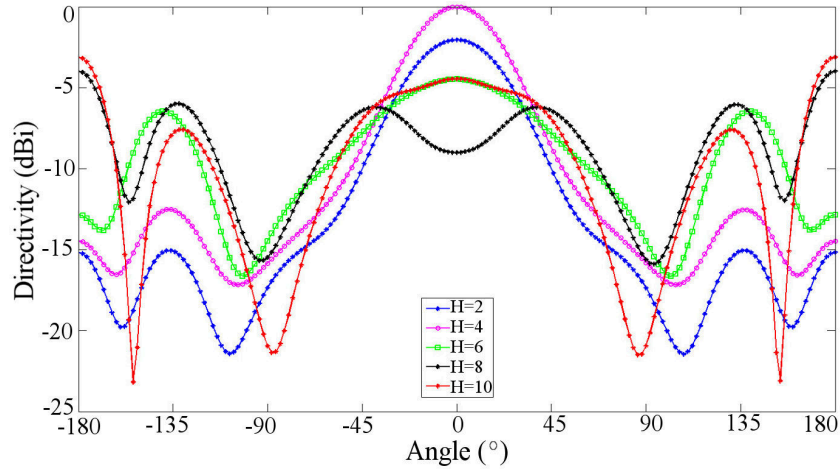


Figure 6.5: Simulated maximum directivity versus the size of the outer ground plane

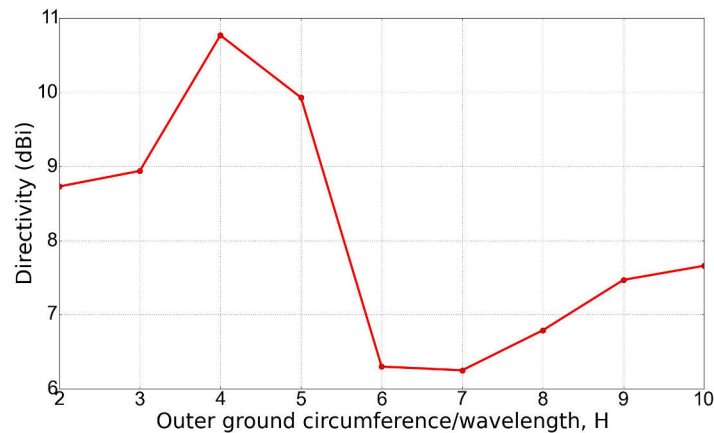


Figure 6.6: Simulated normalised maximum directivity versus the size of the outer ground plane

The input impedance at each port of the modified slot-ring antenna at the design frequency of 300GHz also shows a dependence on the size of ground plane as shown in Figure 6.8. The input impedance is inductive with the reactive part of the impedance between steadily increasing with H from $70\ \Omega$ and $95\ \Omega$ when $H \in [2, 6]$ and reducing there after. The resistive part shows a relative steady value around $25\ \Omega$ for $H \in [3, 5]$, reaching a peak of $40\ \Omega$ at $H=6$ and then reducing to $11\ \Omega$ for H greater than 9. The dependence on the input impedance gives a designer a parameter to manipulate for integration with RTD oscillators for matching purposes to maximise power transfer and design of oscillation frequency by adjusting the effective inductance.

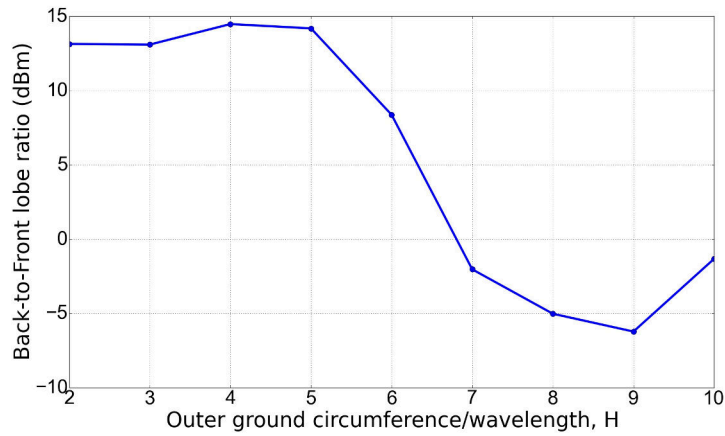


Figure 6.7: Simulated front-to-back ratio versus the size of the outer ground plane

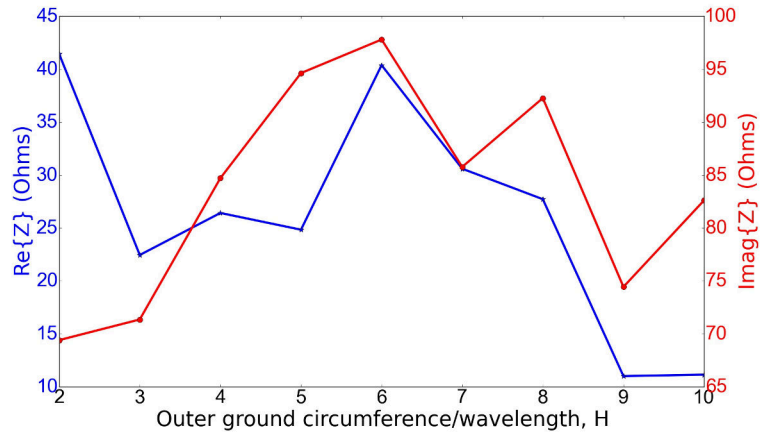


Figure 6.8: Input impedance versus the ground size

6.5 Experimental validation of modified slot-ring antenna

A slot-ring MPD antenna was designed, optimised and fabricated for 5 GHz operation to validate for the first time the concept of a slot ring antenna with a backing ground plane. The 5 GHz frequency was chosen for proof of concept due the ease of fabrication and less sensitivity to fabrication errors. Figure 6.9 shows the fabricated antenna on 762 μm thick Rogers laminated board ($\epsilon_r = 3.48$) with 1 μm thick copper. The optimal dimensions were derived based on the formulation described in the preceding section for maximum directivity. The optimal parameter are: of $H=4$, with the outer circle radius of 25.41 mm, slot radius, $r = 7.57$ mm and a slot width of 3 mm on a 100 mm \times 100 mm board. The fabricated antenna was fed at two locations



Figure 6.9: Fabricated slot ring antenna for 5 GHz operation

quarter wavelength apart. The quadrature phase difference at the feeding points was achieved by using two coaxial cables with a quarter wavelength difference in length connected to a Tee coupler as shown in Figure 6.9.

Figure 6.10 shows the measured and simulated return losses of the fabricated antenna. There is shift in the resonance frequency from 5 GHz to 5.4 GHz due to fabrication tolerances. The measured impedance bandwidth of the antenna is 500 MHz which is an increase of 200 MHz to the simulated bandwidth. The measured fractional bandwidth of the MPD slot ring is thus 18.5%. The phase difference at the two ports was achieved by the use of a quarter wavelength differential in the length which is also subject to errors. A more robust passive fabrication would include the use of integrated circuit (IC) phase shifters. However, since the purpose of this study is to obtain an integrated solution, it was unnecessary to use phase shifters. Using the concept of mutual synchronisation of oscillators driving a common load, the individual oscillators should synchronize in phase and oscillation frequency as previously demonstrated in [130].

The theoretical and experimental farfield radiation patterns are shown in Figure 6.11. The measured patterns matches simulated pattern with an unexpected null appearing at the angle 0° . The unexpected null is attributed to the coaxial cables

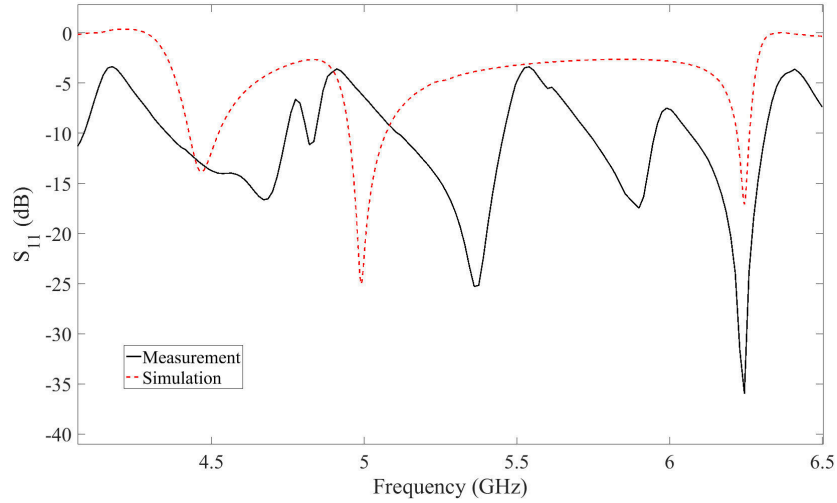


Figure 6.10: Return loss

that run across the front of the antenna. Feeding the antenna from the back through the use of narrower cables is expected to eliminate the effects of the cables. The measured directivity of the antenna is 10.2 dBi, which is similar to the simulated value of 10.8 dBi.

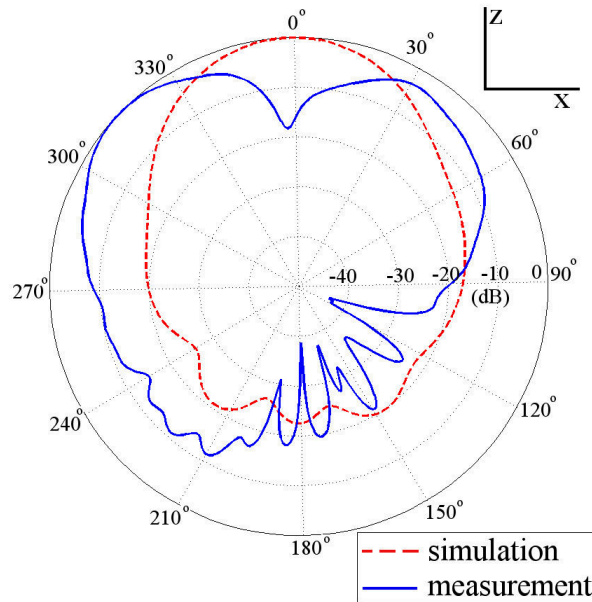


Figure 6.11: Simulated and measured normalised far-field radiation pattern of the 5 GHz slot ring antenna

The simulated axial ratio of the 5 GHz antenna is shown in Figure 6.12(a) as a function of elevation angle. The axial ratio is below the -3 dB level for approximately

$\pm 45^\circ$ around boresight of the antenna at 5 GHz. The simulated axial ratio remain below the -3 dB level at boresight through the -10 dB impedance bandwidth as shown in Figure 6.12(b) from 4.85 GHz to 5.68 GHz. Thus the slot ring antenna has a -3 dB axial ratio bandwidth of approximately 830 MHz.

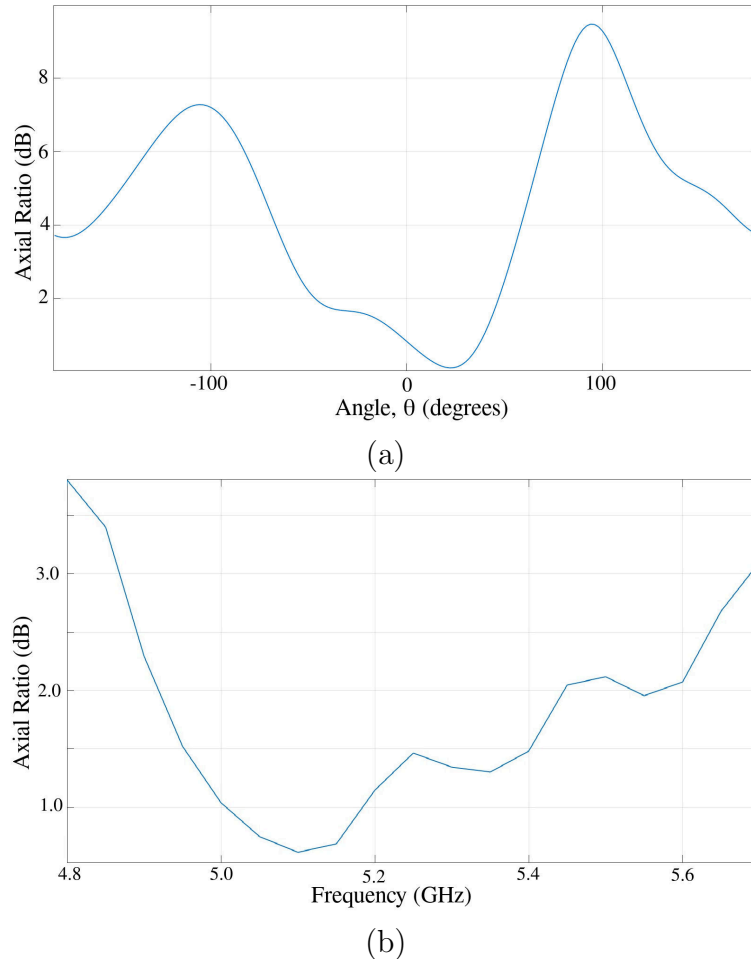


Figure 6.12: Simulated axial ratio of the slot-ring antenna at 5 GHz (a) and axial ratio as a function of frequency at boresight (b).

6.6 Chapter summary

An improved slot-ring multi-port driven antenna with air-side radiation for operation at 300GHz was demonstrated through simulation. Modifications to the original slot-ring antenna geometry are made to include a backing ground plane to focus the energy out of the substrate and into the airside. An optimal design for the improved antenna geometry is also achieved along with relations of the directivity and input

impedance on the geometry of the antenna. A maximum simulated directivity of the improved slot-ring MPD antenna is 10.8 dBi with a side-to-back lobe ratio of 14.8 dBi. The concept of the slot-ring was experimentally verified by a fabricated antenna for 5 GHz operation showing the expected performance with directivity of 10.2 dBi (simulated directivity of 10.8 dBi) and a fractional bandwidth of 18%.

Chapter 7

Resonant Tunnelling Diode Oscillator Based Millimetre-wave Communications Systems

This Chapter presents experimental work in which resonant tunnelling diode (RTD) oscillators were modulated with data for the purposes of data communications over a wireless channel in the millimetre-wave band. The work in this Chapter establishes the groundwork for building and optimising transceiver systems for millimetre-wave radio frequency (RF) front-ends for 5G user electronics in ubiquitous communications scenarios. The high output power (approximately 1 mW) RTD oscillators reported in [78] and [82] are used in this Thesis as part of millimetre-wave transmitter systems. The oscillators are characterised and modulated with data to determine the achievable data rates. Wireless transmission is demonstrated with the use of millimetre-wave commercial antennas. The baseband signal is recovered by a combination of detectors and off-line signal processing using Matlab. The bandwidth limitations and limiting factors of the oscillators are established and recommendations to improve the modulation bandwidth for RTD oscillators to achieve data-rates commensurate with 5G targets are made.

7.1 Resonant tunnelling diode oscillators

The operation of resonant tunnelling diode's (RTD) negative differential region (NDR) allows them to be used in compact oscillator design. When the self capacitance C_n formed by the top and bottom contacts of the RTD is connected in parallel with

an inductor L an L-C tank is formed which oscillates when the RTD is biased in the NDR. The oscillation frequency is given by $F_{osc} = 1/(2\pi\sqrt{C_n L})$. The RTD and RTD-based oscillators were described in Chapter 2.

The oscillator circuits used for experiments in this Thesis are shown in Figures 7.1 and 7.2. The circuit schematic including the bias network are also shown alongside each topology. Topology 1 has two individually biased oscillator circuits with one RTD each. The design was optimised for high radio frequency (RF) output power which is around 1 mW realised by power combining from the two individual oscillator circuits. The inductance L is realised by the co-planar waveguide of length $710 \mu\text{m}$ which forms an L-C tank with the self-capacitance of the RTD, C_n . The length of the inductor is a design parameter for oscillation frequency which is varied to obtain different oscillation frequencies between 28 GHz and 40 GHz. A stabilising resistor R_e is employed to suppress bias oscillations. The capacitor C_e is designed to be a short circuit at the design frequency and thus isolate the biasing network (R_b and L_b) from the LC tank and avoid power dissipation across the stabilising resistor R_e . Deploying two oscillators to drive a common load allows power combining with power up to 1 mW reported in [78]. The oscillators with topology 1 were designed for 28-43 GHz operation which is at the lower end of the millimetre-wave band. This frequency range is a good candidate for edge/last-mile connectivity or pico-cells because of relatively lower atmospheric attenuation compared to other millimetre wave frequencies.

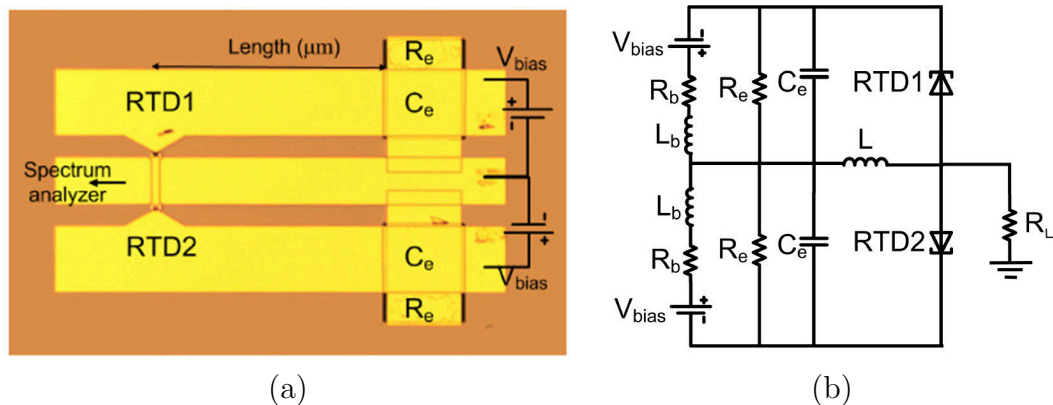


Figure 7.1: Oscillator topology 1 (a) microscope picture oscillator [131] and (b) circuit schematic including the bias network and load.

The second oscillator circuit (topology 2) used in this study is shown in Figure 7.2. The design oscillation frequencies range from 220 GHz to 300 GHz covering the upper end of the millimetre-wave band. The high atmospheric attenuation at the

these frequencies makes this channel ideal for short-range communications. The key difference to topology 1 is that a single oscillator circuit is used, and the inductance L realised by use of a microstrip line of length $l \mu\text{m}$ instead of a CPW. The stabilising resistor R_e in the second topology is realised by two 30Ω resistors in parallel. The components R_e and C_e have the same functionality as described for topology 1. A summary of the oscillators key parameters is presented in Table 7.1.

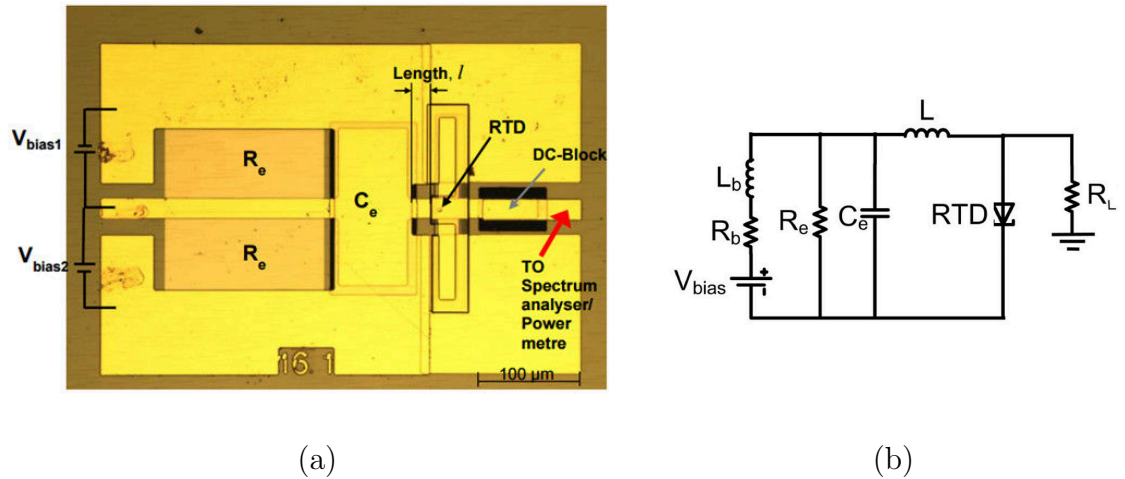


Figure 7.2: Oscillator topology 2 (a) microscope picture oscillator [82] and (b) circuit schematic including the bias network and load.

Table 7.1: Summary of RTD oscillators key circuit components.

Parameter	Topology 1	Topology 2
Operation Frequency	33-43 GHz	220-300 GHz
Output RF power	1 dBm [78]	1 dBm [82]
Number of RTDs	2	1
RTD size	$4 \times 4 \mu\text{m}^2$	$5 \times 5 \mu\text{m}^2$
R_e	20Ω	15Ω
C_e	16 pF	10 pF

7.2 Oscillator characterisation

The RTD oscillator of topology 1 were characterised to obtain the response to the bias voltage. The bias voltage was swept across the negative differential region (NDR) and the oscillation frequency and the RF power output was observed on a spectrum analyzer. Figure 7.3 shows the response of oscillation frequency and output power

as a function of bias voltage of a 43 GHz oscillator. The frequency shows a relatively flat response to bias voltage from 1.42 V to 1.75 V after which the frequency has an abrupt transition from 43.62 GHz to 43.28 GHz. The flat response of the frequency is attributed to the two independently biased oscillators injection locking each other when coupled to the same load. The output power shows a direct relation to the bias voltage in the first part of the NDR steadily increasing with an increase in bias voltage until a maximum output power is reached. The output power reduces with increase of bias voltage as the RTD is taken out of the NDR. This behaviour suggests that circuit can be used as a voltage-controlled oscillator (VCO) controlling the intensity of the RF signal by varying the bias voltage. The output power and bias voltage have a quasi-linear relationship between 1.45 V and 1.65 V. This makes it possible to perform amplitude modulation of the carrier signal by varying the bias voltage because the modulating signal has a one-to-one relationship with the output intensity which allows the modulating signal to be recovered.

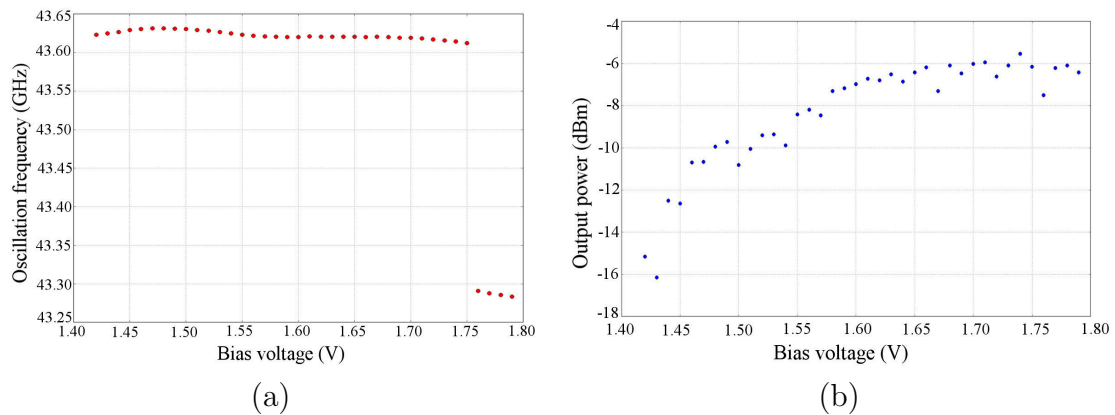


Figure 7.3: Frequency of oscillation (a) and output power (b) as a function of bias voltage for the 43 GHz oscillator

The oscillators of topology 2 were also characterised for the relationship of the output power and oscillation frequency to the bias voltage. A particular oscillator used in subsequent experiments chosen due to its high output power is presented subsequently. The oscillator has a free running oscillation frequency around 240 GHz. The relation of the oscillation frequency and the bias voltage is shown in Figure 7.4(a) while the output power relation to the bias voltage is shown in Figure 7.4(b). The oscillator showed oscillation under negative bias only, which is a result of fabrication process variations and different materials from the circuits of topology 1. The frequency varies steadily with the bias voltage as it is swept across the NDR as shown

in the figure. The output power steadily increases and reaches a maximum and then reduces as the bias voltage reaches the end of NDR.

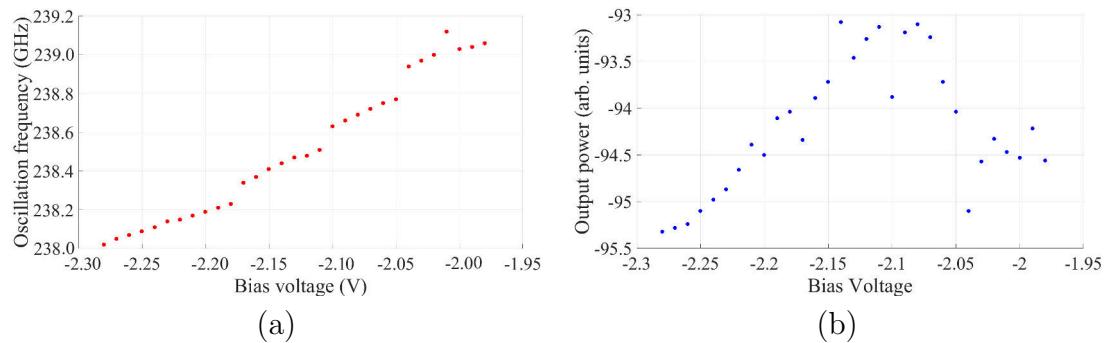


Figure 7.4: Frequency of oscillation (a) and output power (b) as a function of bias voltage for the 238 GHz oscillator.

7.3 Modulation bandwidth characterisation

Operating the RTD oscillator as a voltage controlled oscillator (VCO) within the region where the output power has a linear response allows one to perform amplitude modulation (AM) as shown in Figure 7.5. In this setup the RTD is used as a mixer with the modulating signal appearing as sidebands around the carrier signal. The 43 GHz frequency independence of the bias voltage allows straight forward coherent detection with a fixed local oscillator (LO) at the receiver end used with a mixer. The time domain output of the modulated signal is shown in Figure 7.5 on the right. The output signal is a carrier signal at the free running oscillation frequency with an amplitude that follows the shape of the modulating signal. Other forms of AM like amplitude shift keying (ASK) can also be used to send digital data which is more robust to noisy channels.

7.3.1 Amplitude modulation experiments

To establish the modulation bandwidth of the RTD oscillators of topology 1, the 43 GHz oscillator was biased at a fixed voltage of 1.55 V. A -17 dBm sinusoid was superimposed via a bias tee as shown in Figure 7.6 to perform AM modulation as described and shown in Figure 7.5. The modulated output was observed on a spectrum analyzer and a snapshot is shown in Figure 7.7(a). The distance of the sidebands from the carrier frequency follows the modulation frequency in a graph of slope 1 as

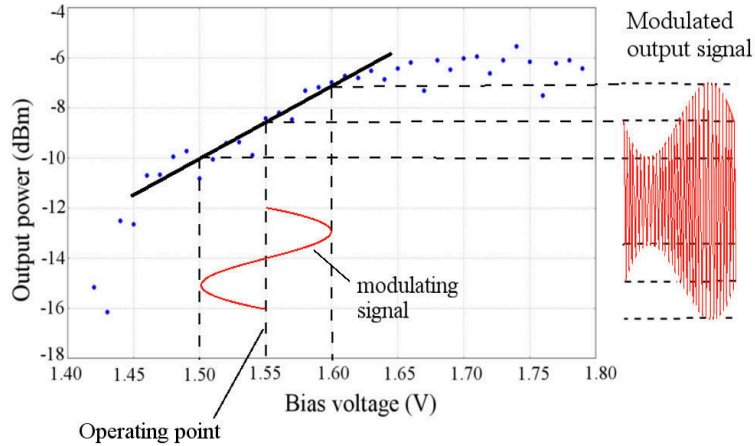


Figure 7.5: Amplitude modulation of a voltage-controlled oscillator.

shown in Figure 7.6(b) confirming that the sidebands observed on the spectrum analyzer are the mixed products of the free running oscillator and the modulating signal.

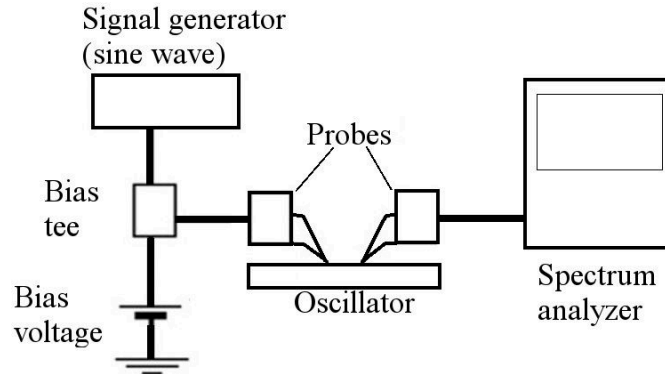


Figure 7.6: Experiment set up for modulation bandwidth determination.

The modulation frequency was swept from 100 MHz to 1 GHz and the power of the sidebands was monitored as shown in Figure 7.8. The lower frequency of modulation was determined by the bias tee used which had a lower cut-off frequency of 100 MHz. The modulation bandwidth of the oscillator is defined as the frequency at which the power of the sidebands is half of the initial power. The power of the sidebands fall below the 3 dB point of the initial value at approximately 300 MHz as shown in Figure 7.8. Thus the modulation bandwidth of the oscillator is 300 MHz, which gives a theoretical limit on the achievable data-rate of 428 Mbps.

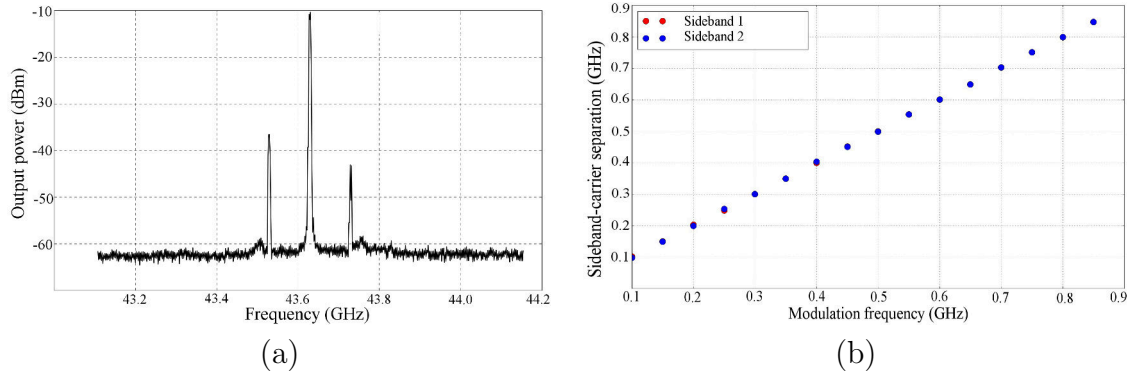


Figure 7.7: Frequency domain output (a) mixed signal showing carrier at 43 GHz oscillator and sidebands and (b) sideband separation from carrier as a function of modulation frequency.

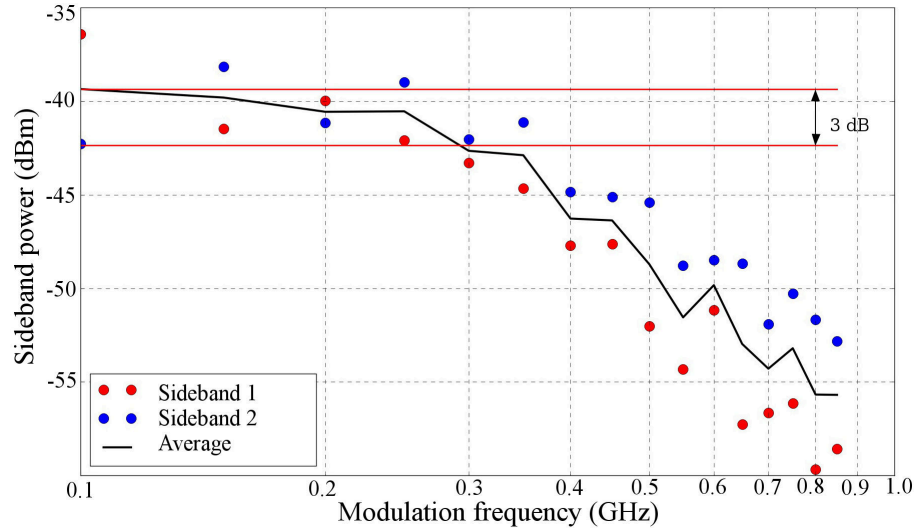


Figure 7.8: Modulation bandwidth of 43 GHz oscillator.

7.3.2 ON-OFF keying modulation

The modulation bandwidth calculated previously provides a theoretical data rate achievable by the oscillator. To determine the actual data rate achievable by the RTD oscillators, a random bit pattern was used to simulate data transmission to observe the limit. On/Off Keying (OOK) allows a straight forward method of modulating the oscillator by switching the RTD in and out of the NDR by adjusting the bias voltage. OOK significantly simplifies the design of the receiver since non-coherent detection is possible, with only an envelope detector required to retrieve the baseband signal. To perform On/Off keying, the oscillator was biased just outside the NDR as shown in Figure 7.9 at -1.95 V. A non-return to zero (NRZ) pseudo random bit sequence

(PBRS) with an amplitude of 0.5 V was superimposed on the bias voltage via a bias tee. This has the effect of switching the VCO on and off based on the incident bit as shown by Figure 7.9.

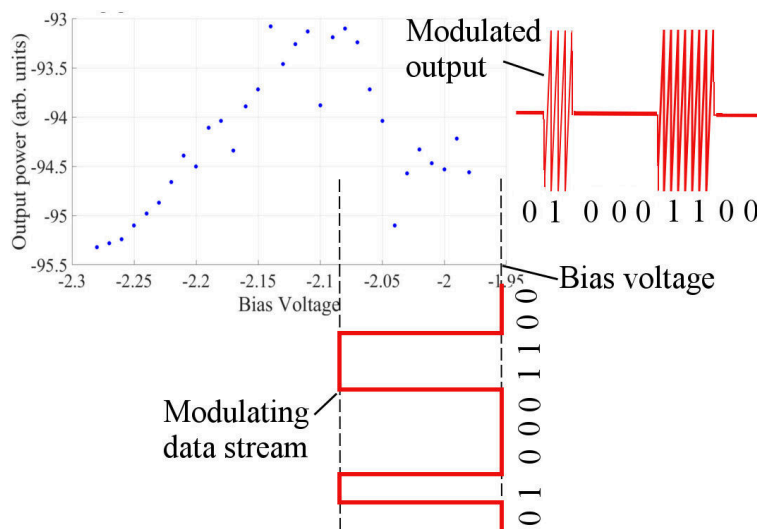


Figure 7.9: ON/OFF keying of an RTD oscillator.

Figure 7.10 (b) shows the modulated output of the oscillator observed on a real-time oscilloscope showing an On/Off keyed RF signal. The modulation data rate of 10 Mbps from an Anritsu pseudo random bit sequence (PRBS) generator was the slowest achievable data rate. To demodulate the signal and recover the original data, an envelope detector is required at the receiver end. A Matlab script was written to perform the envelope detection and retrieve the modulating bit pattern from the modulated signal. The envelope detection was performed by taking the magnitude of the signal (i.e. full wave rectifier) and a low pass filter. The same (or equivalent) operations can be realised in hardware on a field programmable gate array (FPGA) or as a custom integrated circuit (IC) for a dedicated compact receiver module. Figure 7.10(b) shows the demodulated baseband signal at 100 Mbps by the use of offline signal processing in Matlab.

The transitions between on and off state show some transients as shown in the figure. Close-ups of the ON and OFF transients are shown in Figure 7.11(a) and (b) respectively. There are apparent settling times on the transitions between a 1 bit and a 0 bit. The transition from the Off state to the On state takes 2 ns for the oscillator to settle in a constant envelope and frequency as shown in Figure 7.11(a). The tran-

sition from On to Off also takes approximately 2 ns. The rise and fall settling times place a constraint on the minimum bit duration of at least 4 ns to allow the oscillator to switch from Off to On and Off again. If the oscillator is driven with pulses smaller than 4 ns the oscillator will not be able to switch accordingly and provide a modulated millimetre wave signal. These rise and fall settling time determine the modulating datarate using ON/OFF keying at 250 Mbps.

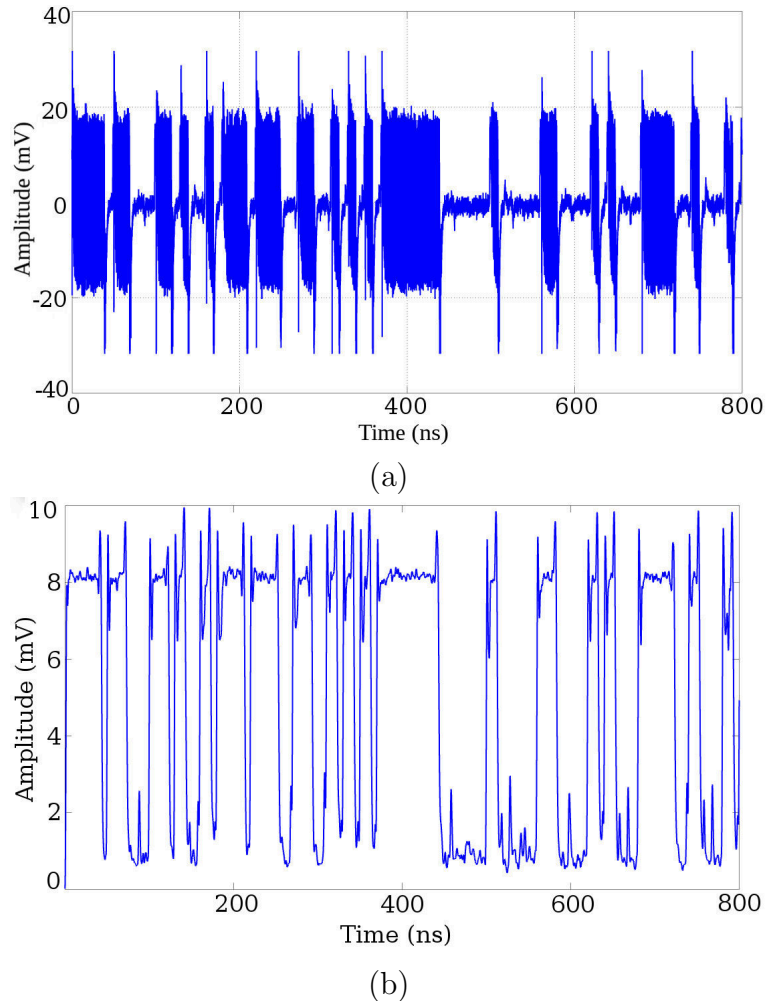


Figure 7.10: OOK modulated signal from the 33 GHz oscillator (a) and the demodulated baseband signal (b) at 100 Mbps.

A common way of measuring the fidelity of a received signal in communications is the use of eye diagrams. Eye diagrams give a measure of how difficult it is to distinguish between a zero bit and one bit. A wide eye with distinct levels for zero and one mean that the decision is easy and low probability of error. Eye diagrams at selected datarates presented in Figure 7.12 shows the fidelity of the demodulated

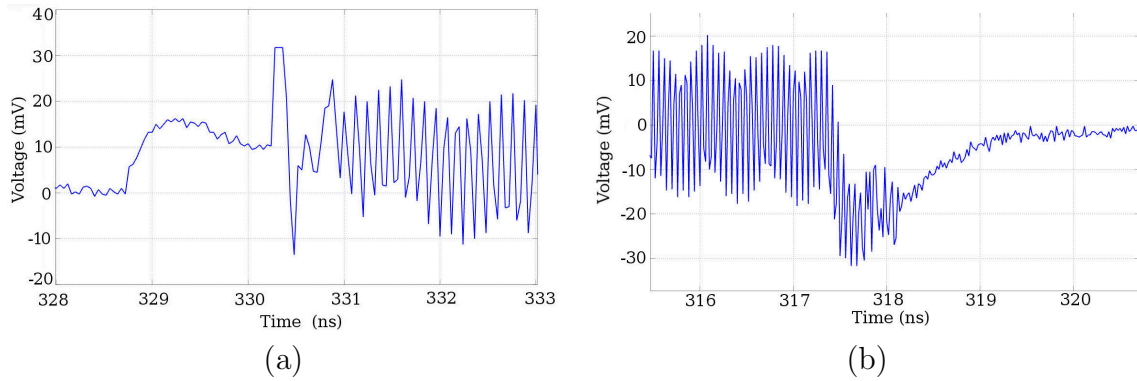


Figure 7.11: Bit transitions of the oscillator during On/Off Keying; (a) Off-to-On transient and (b) On-to-Off transient.

signals. Figure 7.12(a) shows the eye diagram at 10 Mbps, with distinct levels of 0 bit and a 1 bit shown by the vertical opening of the eye of approximately 8 mV which allows error-free detection of the modulating signal. Figure 7.12(b) shows the eye diagram at 40 Mbps modulation which also shows good signal fidelity with a wide eye diagram with about 4 mV vertical opening. Figure 7.12(c) and (d) show the demodulated signal at 100 Mbps and 200 Mbps respectively. The eye diagrams still show small eye opening but also show some jitter which causes timing problems and intersymbol interference between successive bits. The jitter is attributed to the phase noise of the oscillator. The On and Off transients shown in Figure 7.11 have more impact at higher modulation frequencies and make two levels for logical 1 symbols as shown in Figure 7.12(d) at 200 Mbps which makes the decision between a zero and a one difficult and subject to errors.

The G-band oscillator modulation bandwidth were characterised using a Schottky barrier diode (SBD) detector due to the unavailability of oscilloscopes capable of capturing signals at 225-325 GHz. Schottky barrier diodes used as detectors are capable of detecting the intensity of millimetre and sub-millimetre (terahertz) waves. These detectors are can perform envelope detection of very fast switching signals up to approximately 40 GHz [132]. An experiment as illustrated in Figure 7.13 using a Virginia Diodes Inc. (VDI) WR3.4ZBD-F40 zero bias SBD detector (220-325 GHz) was performed to characterise the achievable datarates of the 240 GHz oscillator. The SBD detector output is the demodulated baseband signal and the output was observed on a real-time oscilloscope without further processing. Eye diagrams of the recovered signal are shown in Figure 7.14 at selected datarates. Figure 7.14(a) shows the eye diagram at 2 Mbps with good fidelity of the signal shown by the wide opening

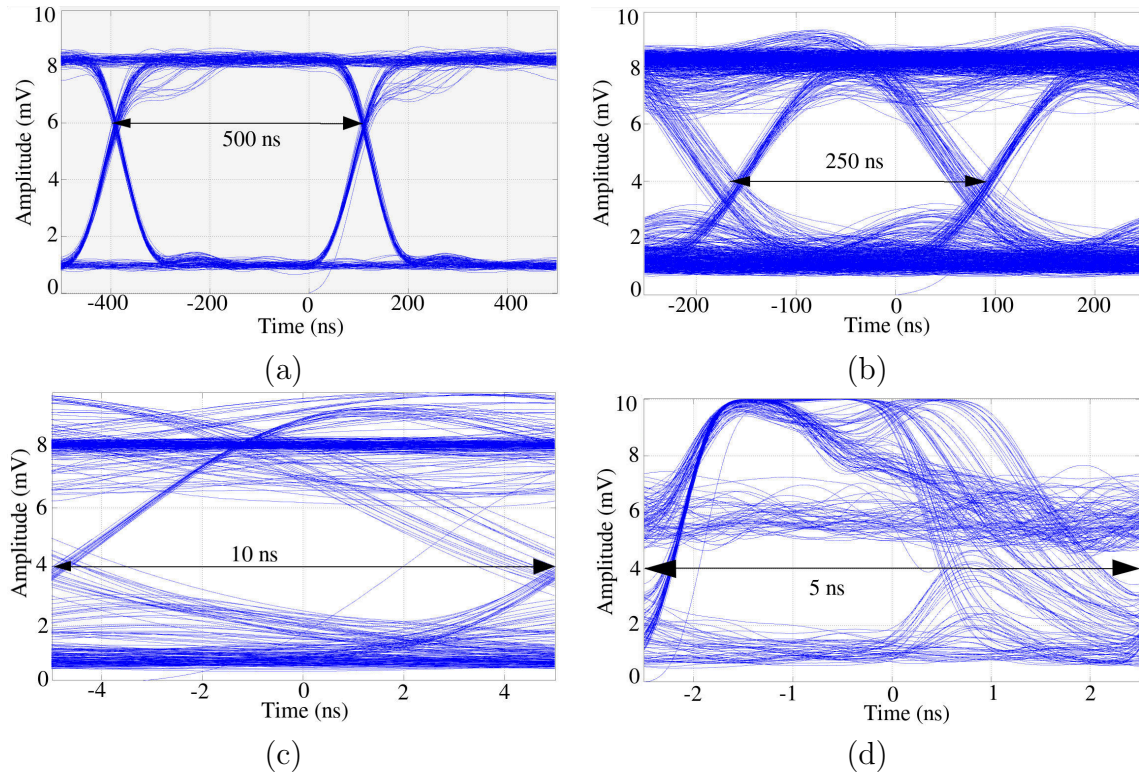


Figure 7.12: Eye diagrams of the recovered data at select frequencies; (a) 20 Mbps, (b) 40 Mbps, (c) 100 Mbps, and (d) 200 Mbps.

of the eye. The eye gradually gets smaller with increasing modulation speed as shown by Figure 7.14(b) and (c) at 8 and 10 Mbps respectively. The maximum achievable data rate from the 240 GHz oscillator is 15 Mbps as shown in Figure 7.14(d) as shown by a very small eye opening. A small eye opening implies that the decision between a 1 bit and 0 bit is difficult to make. The decision would be even harder over a noisy channel (e.g. wireless transmission). The small modulation bandwidth of topology 2 oscillators is attributed to the suboptimal bias network which is dominated by a large decoupling capacitor C_e of 10 pF.

7.4 Wireless communications using RTD oscillators

This Section presents experimental work using the oscillators discussed previously in wireless data transmission experiments.

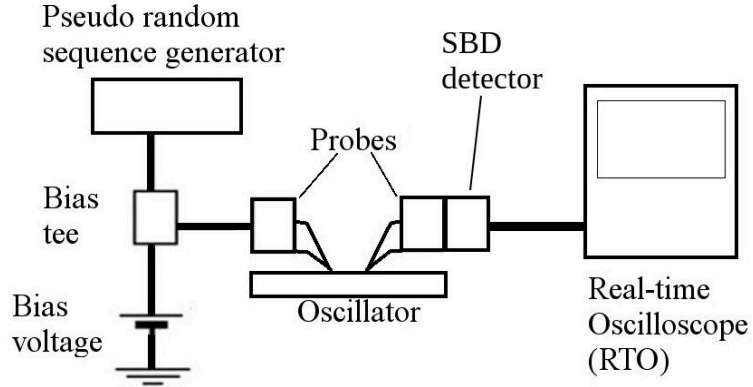


Figure 7.13: Modulation bandwidth experiment using a Schottky barrier diode detector.

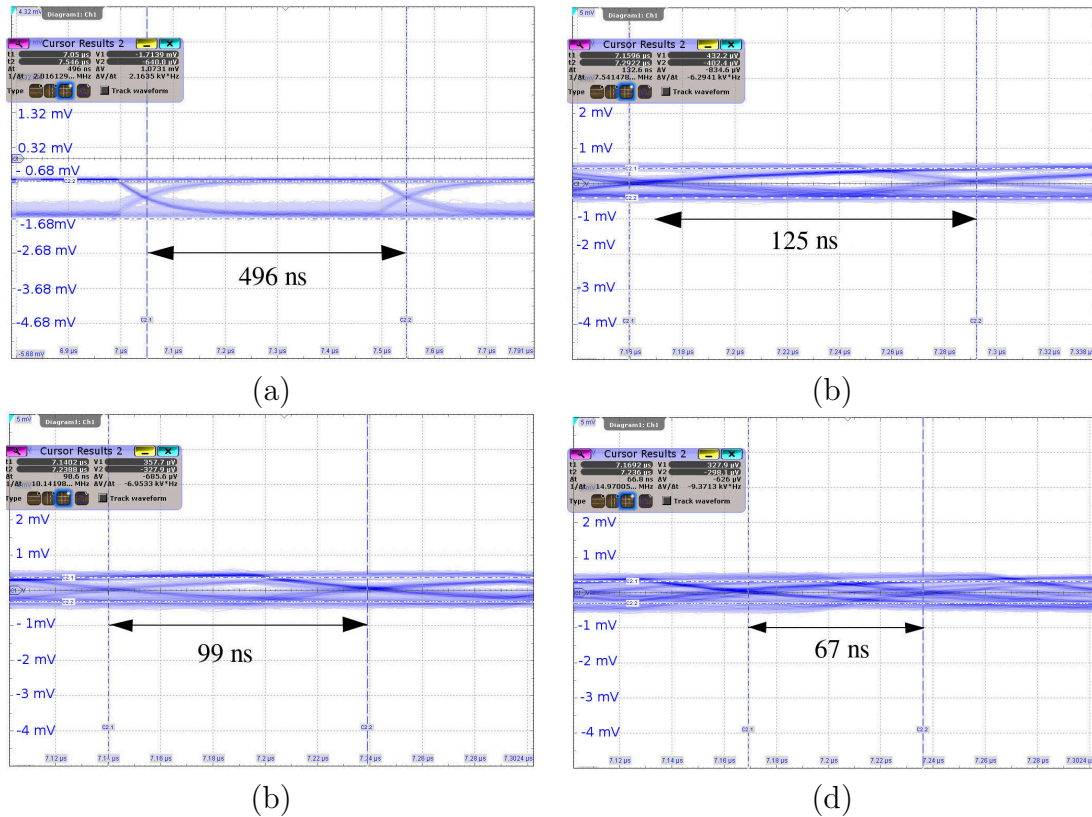


Figure 7.14: Demodulated baseband eye diagrams at selected datarates (a) 2 Mbps, (b) 8 Mbps (c) 10 Mbps, and (d) 15 Mbps.

7.4.1 K-band communications

A wireless transmission experiment was set up as shown in Figure 7.15 over the K-band at 33 GHz using On/Off keying as discussed previously. The oscillator was biased just outside the NDR and a pseudo-random bit sequence was used to switch

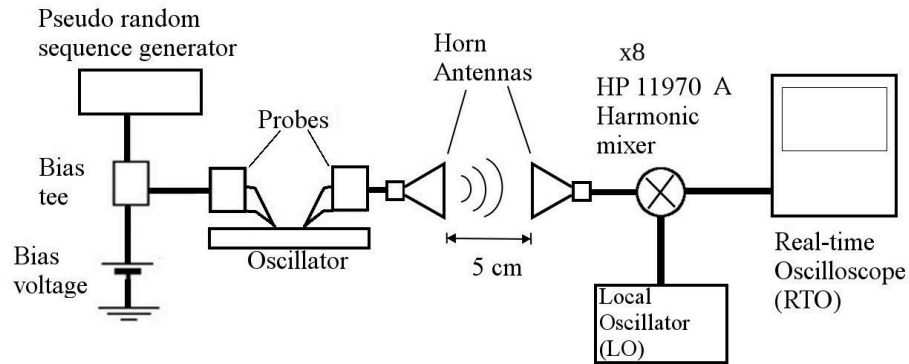


Figure 7.15: OOK modulation experimental set up for the 33 GHz oscillator

the oscillator on and off via a bias tee. The output of the oscillator was then connected to a Farran 26-40 GHz horn antenna. An identical horn antenna was placed 5 cm away from the transmitter in line-of-sight (LOS) conditions. The received RF signal was then mixed down from 33 GHz to 1 GHz using an HP 11970A 8th harmonic mixer using an Anritsu frequency synthesizer at 4 GHz as the local oscillator. The mixed down signal was then recorded on a real-time oscilloscope. The baseband signal was recovered by offline processing using Matlab using envelope detection. Envelope detection was achieved by taking the magnitude of the signal and then low pass filtering as described previously.

The eye diagrams at select datarates are shown in Figure 7.16. Figure 7.16(a) shows the demodulated baseband signal at 20 Mbps with high signal fidelity as shown by distinct levels of each symbol and an open eye. The eye diagrams at 30 Mbps still show distinct levels of each symbol but show some jitter between symbols which leads to timing issues and inter-symbol interference as shown by the eye closing in the horizontal axis. This behaviour attributed to the use the general purpose HP 11970A mixer which is not designed for high speed switching. The effect is more pronounced at 40 and 50 Mbps as shown by the closed eye diagrams in Figure 7.16(c) and (d) respectively.

7.4.2 G-band communications

To achieve wireless data transmission with the the 240 GHz oscillator, the output was connected to a G-band horn antenna. A commercial quasi-optical Schottky barrier diode (SBD) detector - from Tera-Tech Components- was placed approximately 3 cm

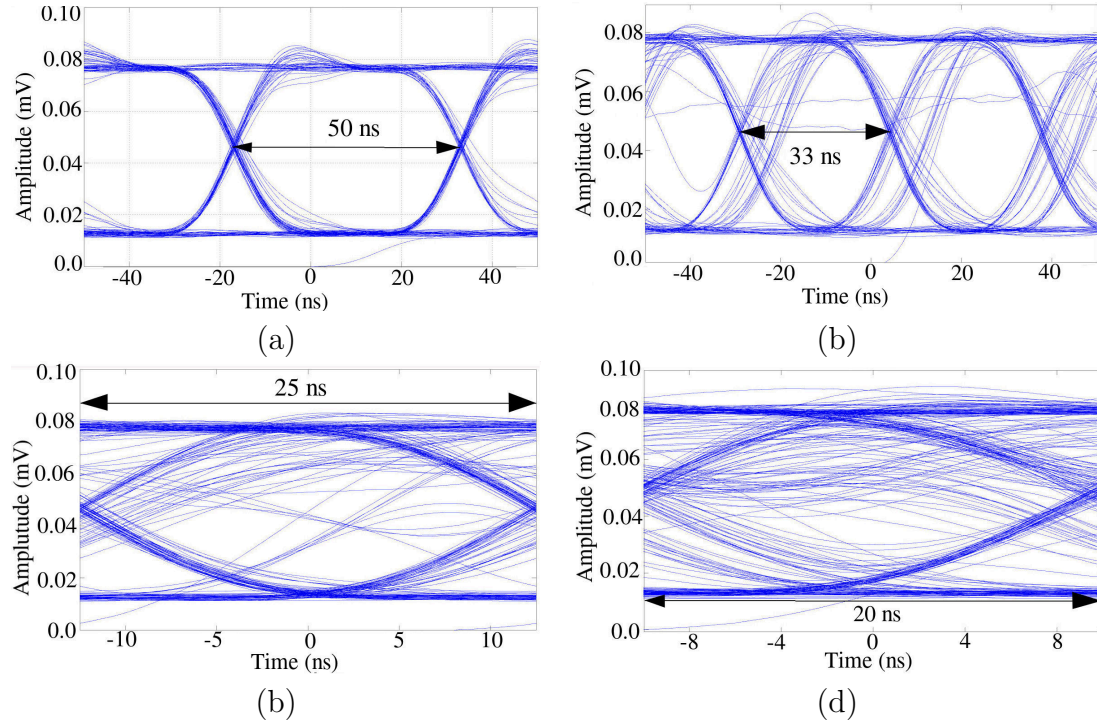


Figure 7.16: Eye diagrams of the demodulated baseband signal transmitted wireless at 33 GHz; (a) 20 Mbps, (b) 30 Mbps, (c) 40 Mbps, and (d) 50 Mbps.

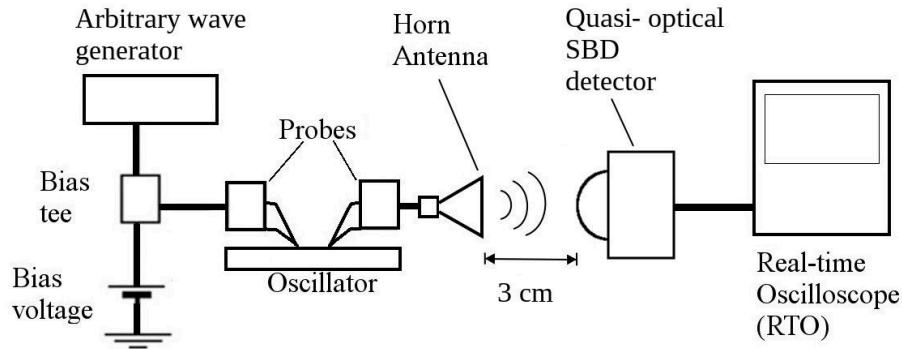


Figure 7.17: Schematic of air 240 GHz communications experimental set up using a quasi-optical Schottky barrier diode detector

in line of sight conditions with the horn antenna with a micro-positioner as shown in Figure 7.18. A schematic of the experiment set up is shown in Figure 7.17. The quasi-optical SBD detector performs non-coherent envelope detection of the modulated RF signal and gives the baseband signal with no requirement for further processing. The demodulated signal was observed on a real-time oscilloscope (RTO) with an input resistance of $1\text{ M}\Omega$ and eyediagrams of the recovered baseband signal at selected

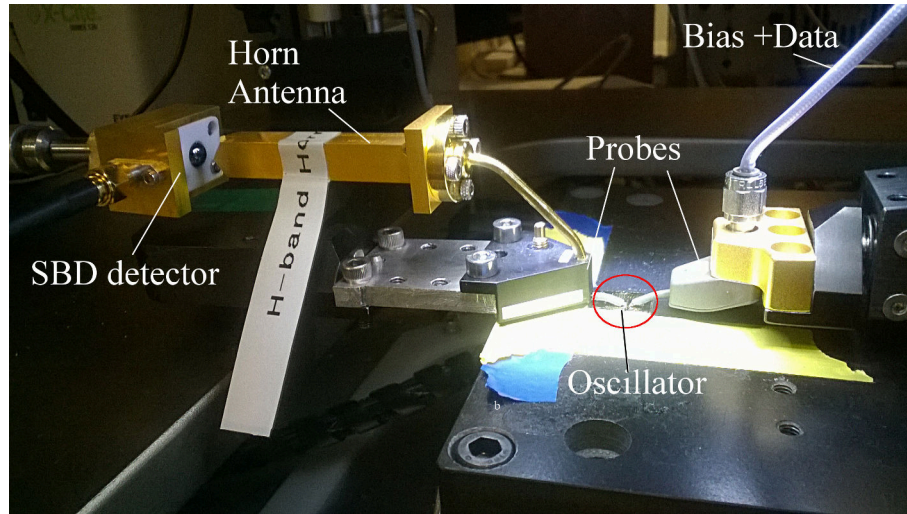


Figure 7.18: Air 240 GHz communications experimental set up using a quasi-optical Schottky barrier diode detector

datarates are shown Figure 7.19.

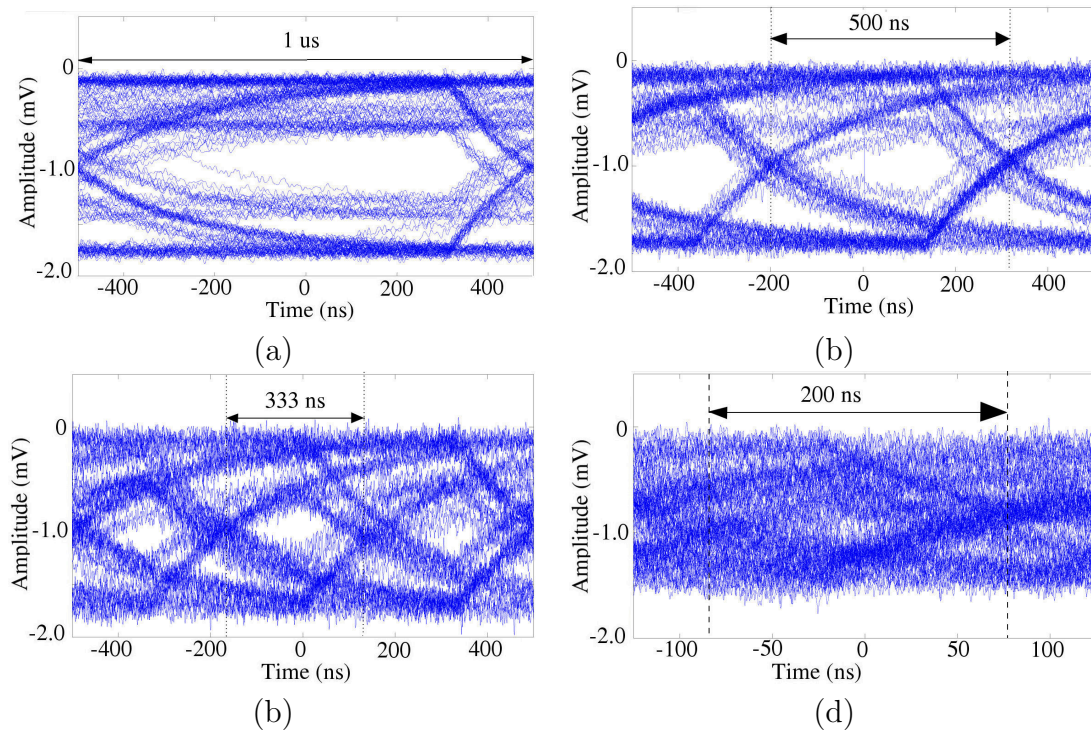


Figure 7.19: Eye diagrams of the filtered quasi-optical SBD detector output at selected datarates;(a) 1 Mbps, (b) 2 Mbps, (c) 3 Mbps, and (d) 5 Mbps.

The wireless transmission channel at 240 GHz introduces some noise into the system resulting in a noisy received signal. The SBD detector has bandwidth of above 40 GHz and thus records the fluctuations of the received signal due to noisy channel

up to those frequencies. A low-pass filter was used to remove the high frequency components noise and improve the fidelity of the signal by off-line processing in Matlab thus improving the eye diagrams of the SBD detector. The received signal at 1 Mbps as shown in Figure 7.19(a) shows distinct levels for each of the two symbols received shown by a well defined eye diagram. There is evidence of multiple levels for each symbol as shown by the thick line at the top and bottom of the eye which is not apparent in the eye diagrams shown in Figure 7.14. Figure 7.14(b) and (c) show the eye diagrams of the received signal at 2 and 3 Mbps, showing error free detection evidenced by open eye diagrams. The limit of the achievable data rate in this setup is 5 Mbps as shown in Figure 7.14(d) by an almost closed eye diagram. The lower data rates achieved in this experiments are attributed to the noise introduced by the wireless channel.

7.5 Chapter summary

In this Chapter, the modulation bandwidth of the high power resonant tunnelling diode oscillators fabricated for ubiquitous communications applications were characterised. Wireless transceiver systems at 28-40 GHz and 240 GHz were built using combinations of horn antennas and quasi-optical Schottky barrier diode detectors. The modulation bandwidth of the oscillators were found to be limited to 300 Mbps and 16 Mbps for the 28-40 GHz oscillators and 220-300 GHz oscillators respectively. The low modulation bandwidth of the oscillators was due to the fact that the oscillators were optimised for high RF output power as part of the initial study and process optimisation and not modulation bandwidth which forms part of future work. The suboptimal bias network features an oversized decoupling capacitor which effectively forms a low pass filter network that slows down the response of the overall transmitter system. Wireless millimetre-wave communications systems were built by a combination of horn antennas, quasi-optical Schottky barrier diode detectors and some offline signal processing using Matlab to recover the baseband signal. Error free wireless communications over short distances were achieved at low data rates. The 28-40 GHz oscillators managed to achieve up to 30 Mbps error-free wireless transmission over a distance of 5 cm using commercial horn antennae although the data rate was limited by the slow response of the mixer used in the receiver subsystem. The 220-325 GHz oscillators managed to achieve 3 Mbps error-free wireless transmission at a distance of 3 cm.

Chapter 8

Conclusions and Future Work

8.1 Conclusions

In this Thesis, low cost communication solutions to enable the next generation of mobile communications (5G) and/or Internet of Things (IoT) devices are presented and studied. The work was divided into three different fields all aimed at low-cost solutions of enabling 5G and IoT. The first part of the study involves study of low-cost fabrication of antennas and radio frequency (RF) guided wave structures up to 10 GHz using the thermal transfer printing technique on renewable, light weight, flexible and low-cost substrates. The second part involves design and optimisation of a multi-port driven slot antenna for purposes of integration with resonant tunnelling diode (RTD) oscillators for high data rate millimetre-wave communications. The third part is an experimental study of modulating RTD oscillators to determine and improve achievable modulation bandwidth to meet 5G demands. Significant academic contribution was made with the publications that resulted from this study and future work recommendations are made subsequently in this Chapter.

The main achievements of this study are:

1. Successful demonstration and characterisation of the thermal transfer printing method as a viable electronics fabrication method for low-cost, lightweight and flexible large area electronics (LAE) on renewable substrates from DC to 10 GHz for IoT applications. Academic contribution was made through publications resulting from the study in the area of low-cost, flexible printed large area electronics for IoT applications [106, 110]
2. First known benchmarking of the performance of the thermal transfer print-

ing method to inkjet printing, which is an established method of low-cost, lightweight and flexible printed electronics. Thermal transfer printing has been shown to achieve similar or better read range in RFID applications. The results of which show that the metal thickness limitation is offset by the higher conductivity, making the thermal transfer printing actually an equally good choice for performance and advantageous in terms of convenience. Contribution to the field was made through publication in [61,133]

3. A multi-port driven slot-ring antenna was optimised for purposes of integration with resonant tunnelling diode oscillators with emphasis on air-side radiation. Modifications to the original slot-ring antenna were made to include a backing ground plane to reflect the energy travelling into the substrate airside, eliminating the requirement to use bulky lenses. A design criteria for the modified slot-ring multiport driven antenna geometry is established and verified by a fabricated slot-ring antenna at 5 GHz. The optimised fabricated slot-ring antenna achieves directivity of 10.2 dBi compared to the simulated directivity of 11.7 dBi due to the feeding structure. Contribution in this area was made with publication in a major peer-reviewed conference publication [123].
4. Millimetre-wave communication transceiver systems using resonant tunnelling diodes were built demonstrating that RTD oscillators as an enabling technology for ubiquitous communications and IoT. The modulation bandwidth of high output power resonant tunnelling diode oscillators was determined and they were used to send data over a wireless link. This demonstrated that high power RTD oscillators can be modulated, with a tradeoff in terms of the datarate achievable due to the biasing network. The achievable datarates with the oscillators, which were optimised for high high RF power were 200 Mbps at 33 GHz and 16 Mbps at 300 GHz. Recommendations to improve the achievable datarates by optimising the oscillator bias network are made subsequently in the Future Work section to meet the datarate targets for 5G.

8.2 Future Work

The work done in this Thesis has potential to play a major role in the next generation communications. However there are some challenges and/or improvements that should be met to enable pervasive adoption of these technologies in IoT devices, systems and applications. This section provides future work to improve the ther-

mal transfer printing technique, integrating the slot-ring antenna into oscillators and optimising the oscillators for high data rate throughput wireless communications.

8.2.1 Thermal transfer printed antennas and electronics

Thermal transfer printing is an attractive alternative to the pervasive printing techniques used for electronics because it does not require sintering, thus eliminating an additional step from the tag fabrication process, saving time and money. There are opportunities for future work in the area of multiple-pass thermal transfer printing, establishing the fine resolution printing limits, and automating the assembly of printed structures that incorporate passive and active electronic elements, such as switching elements that permit antenna reconfigurability [110] or other circuit applications up to 10 GHz.

1. *Higher resolution printheads and ribbon development:* The printer used in this thesis is an off-the-shelf thermal printer designed for printing bar-codes and label where the micrometre resolution was sufficient. The 300 dpi printhead was able to achieve printing resolution of $200\ \mu\text{m}$. This printing resolution is orders of magnitude larger than that of gravure ($30\ \mu\text{m}$ [134]) and inkjet ($10\ \mu\text{m}$ [134]) printed electronics. There are printheads of 600 dpi (double the resolution of the printer used in this Thesis) available on the market, these should be used in future work to establish the advantage of higher resolution. Printheads above 1200 dpi should theoretically allow resolutions around tens of micrometres as opposed to hundreds of microns of a 300 dpi printer. Improving the printing resolution by investigating and developing higher resolution printheads is expected to improve the achievable feature size, surface and edge roughness and overall print quality. This should allow more compact designs, lower scattering losses and possible application of TTP in millimetre-wave RF circuits where higher resolution is required. The thin metallisation, surface and edge roughness, and crack formation of the available conductive thermal transfer ribbons (CTTR) requires further development to eliminate such printing artefacts so as to improve the performance of TTP printed electronics.
2. *Higher printing speeds:* Although TTP can achieve printing speeds of up to 20 cm/s, it is still slower than the state of art print speeds achieved by gravure and offset printing (up to 15 cm/s [134]). In this Thesis the printing speeds were kept at 5 cm/s due to the compatibility of the substrate and the limited thermal

intensity produced by the printhead. In the preliminary print tests, it was observed that the printing quality is inversely proportional to print speed and proportional to the heat intensity (darkness) which was kept at its maximum. The tradeoff of printing speed on print quality and from optimal settings should be investigated as well as the limit of the fastest achievable printspeeds using more powerful thermal printheads and/or other thermal energy delivery systems (e.g. lasers) should be investigated to improve the printspeeds and throughput of TTP.

3. *Multi-layer and double-sided printing:* Thermal transfer prints are receptive to subsequent re-prints. Multi-layer printing has been used in inkjet and screen printed electronics to improve metallisation thickness and thus reducing the ohmic losses that thin-films suffer from when the metallisation is much smaller than the skin depth. For radio frequency identification (RFID) the skin depth of pure copper at 1 GHz is approximately $1\ \mu\text{m}$. The metallisation of the copper CTTR is $0.34\ \mu\text{m}$, thus the metallisation is a fraction of the skin-depth which leads to significant ohmic losses which increase exponentially as the metallisation drops below 3 times the skin depth [108]. Figure 8.1(a) shows the improvement of the sheet resistance with multi-pass thermal transfer printing. However, there is an alignment problem with multi-pass printing as the substrate needs to be positioned with high degree of precision for successive prints to align. Modifying the printer or building a custom set-up that can achieve micrometre precision alignment or better is an area of future work.

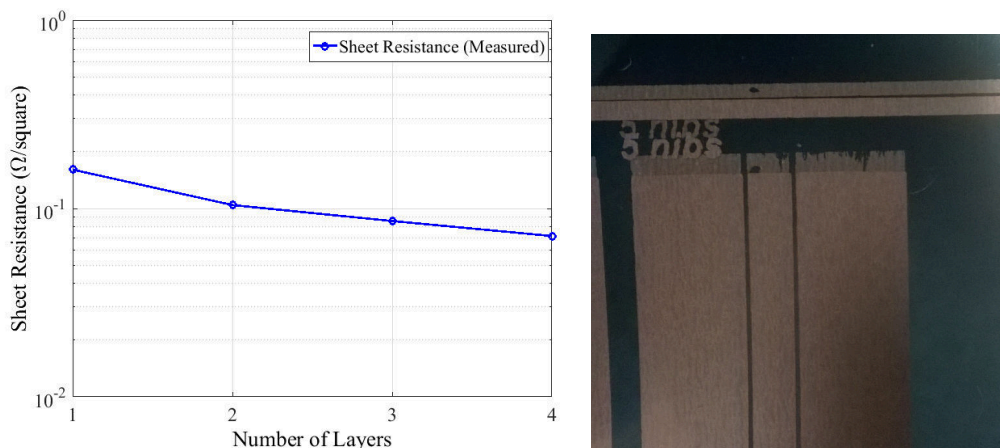


Figure 8.1: Multi-layer and double sided printing; (a) sheet resistance improvement from multilayer thermal transfer printing and (b) misalignment of successive prints

4. *Automated high volume roll-to-roll manufacturing:* Since thermal transfer printing produces dry prints, the prints can immediately be passed through another processing step without risk of smudged prints unlike wet techniques such as inkjet, gravure and screen printing. Figure 8.2 shows a high volume roll-to-roll manufacturing scenario utilising multiple printheads arranged to perform multi-layer and double sided printing.

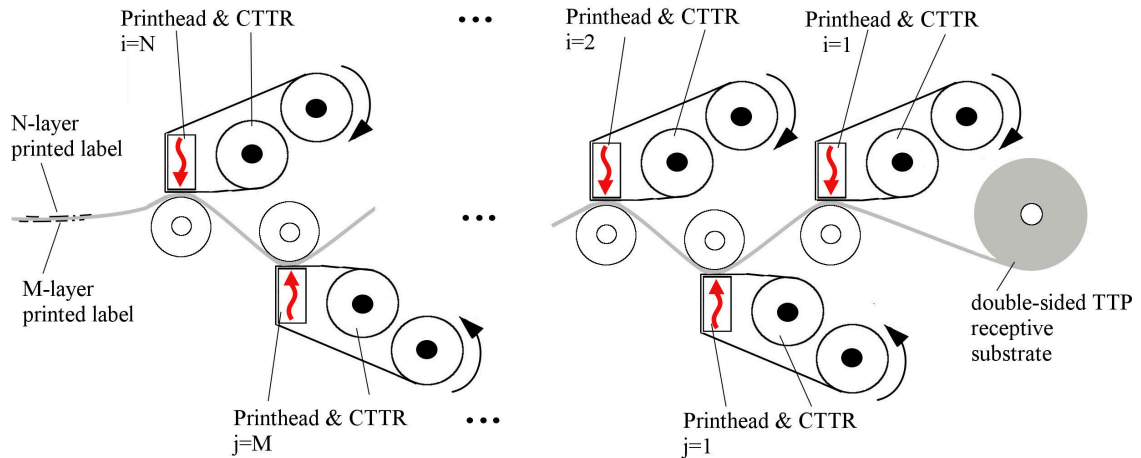


Figure 8.2: Multilayer and double-sided thermal transfer printing in a high volume roll-to-roll manufacturing scenario

5. *Diversify thermal transfer printing receptive substrates:* Thermal transfer printing has thus far been successfully demonstrated on a few substrates (161107-KR-100 and 161107-KR-200 from Polyonics and Thermfilm 21940, Thermfilm 21944E and clear polyethylene terephthalate (PET) from Flexcon due to incompatibility issues of the conductive thermal transfer ribbons (CTTR) with other substrates limiting the number of substrates that can be used with this technique. An area of future work is to investigate more substrates by treating them using similar techniques used for screen printing and inkjet printing [135] to diversify the substrates beyond plastic polymers to fabrics and/or paper.
6. *Repetitive bending and reliability tests:* In this Thesis, performance of coplanar waveguides and antennas under static mechanical bending were studied. However, it is conceivable that TTP electronics will be subjected to repetitive bending if deployed in highly dynamic systems. The performance of TTP electronics after multiple bending cycles is therefore should be established as part

of the future work to characterise how the performance is affected by repetitive bending and possibly improve the reliability and/or robustness of electronics fabricated using this printing technique.

8.2.2 Integrated slot-ring antenna

Based on the findings of the study and optimisation of the multi-port driven (MPD) slot-ring antenna, a self oscillating integrated MPD slot-ring transmitter system composed of several individually biased oscillators for the purposes of power combining is an area of future work. An integrated design with four mutually locked oscillators is proposed as shown in Figure 8.3. Such a design requires modifications to the MPD slot-ring to incorporate bias pads, and to electrically decouple the oscillators to allow independent bias of each oscillator. A potential solution could be realised as shown in Figure 8.3 which shows four individually biased oscillators are arranged in a ring. More oscillators could be integrated using optimal components sizes for power combination and high datarate modulation.

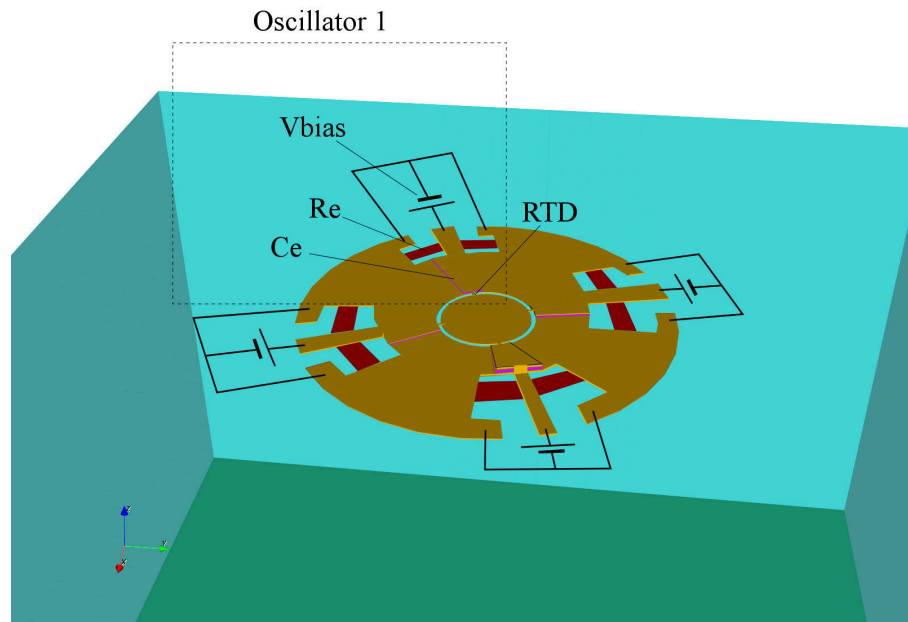


Figure 8.3: Integrated slot-ring antenna with four individually biased and mutually locking oscillators

8.2.3 High datarate millimetre-wave communications using RTD oscillators

The resonant tunnelling diode oscillators used in this Thesis were optimised for high radio frequency (RF) output thus maximising the communication range achievable by RTD oscillators. These oscillators were not optimised for high datarate transmission and the next evolutionary step is to optimise these oscillators for datarates or around 10 Gbps.

1. *Optimisation of bias network:* The decoupling capacitor in the bias network was over-specified leading to low cut-off frequency of 200 MHz. A large decoupling capacitor in the bias network results in a slow response as the capacitor charges/discharges when a data signal is applied across it. The modulation bandwidth is limited by the bias network and decoupling capacitor C_e which forms a low-pass filter. The modulation bandwidth for the 43 GHz oscillator can be approximated by the -3 dB cut-off frequency of the lowpass network of the bias circuitry;

$$BW = \frac{1}{2\pi R_b C_e} = 200 \text{ MHz} \quad (8.1)$$

With the bias cable resistance $R_b = 50 \Omega$ and $C_e = 16 \text{ pF}$. A spice circuit simulation of the bias network for both the 43 GHz is shown in Figure 8.4 along with the expected datarates for optimised oscillator designs. Reducing the decoupling capacitor from 16 pF to 1 pF is expected to allow modulation rates in the order of gigabit per second which would allow these oscillators to meet 5G targets. To obtain datarates in the order of 40 Gbps, the decoupling capacitor should be around 0.1 pF which would allow modulation rates equal to the state of the art [37].

2. *Improved phase noise:* The oscillators used in this Thesis were free running and showed drift of the oscillation frequency. The drift of the oscillation frequency makes coherent detection difficult due to the requirement of a fixed local oscillator (LO) as shown in the experiment in Chapter 7 (see Figure 7.15). Moreover, the phase noise introduces jitter which is shown in Figures 7.19 and 7.16 which is expected to be a significant limitation at very high datarate transmission (i.e. 10 Gbps) as the jitter becomes significant in comparison to the short bit duration at high datarates. The oscillators can be injection-locked and this was demonstrated experimentally improving the phase noise as shown in Figure 8.5.

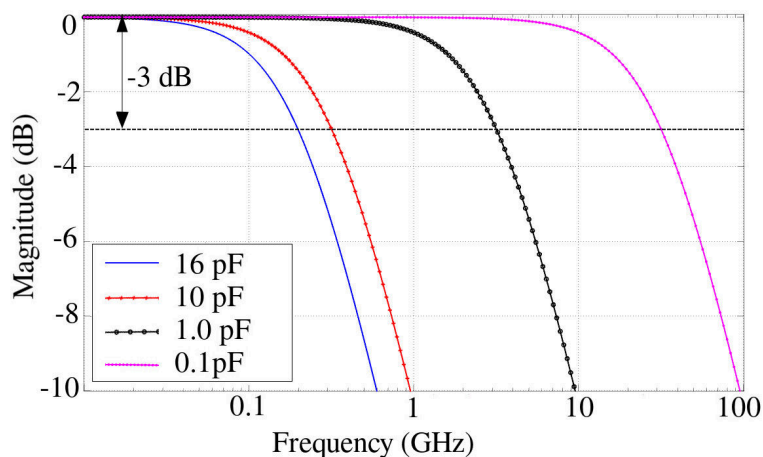


Figure 8.4: Expected modulation bandwidth limits for topology 1 oscillators

The free-running oscillator has -60 dBc/Hz phase noise at 1 MHz offset while under locking with a -10 dBm signal the phase noise reduces by 30 dBc/Hz. The injection locking experiment demonstrate that these oscillators can be stabilised by mutual locking as already demonstrated in Chapter 7 where the oscillation frequency was independent of bias voltage as a result of oscillators injection locking each other. This allows for coherent detection where the phase/frequency of the oscillator can be detected by the receiver facilitating more noise robust modulation techniques.

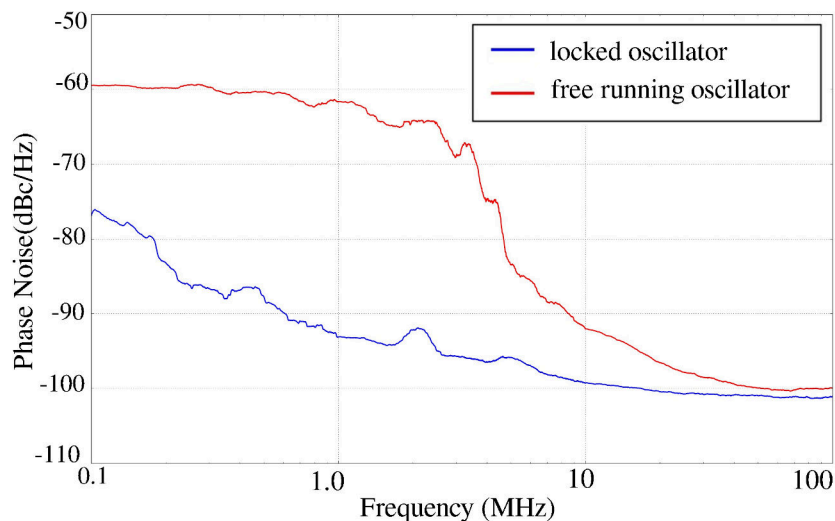


Figure 8.5: Phase noise of 43 GHz oscillator in free running and locked conditions

Bibliography

- [1] R. R. Harmon, E. G. Castro-Leon, and S. Bhide, “Smart Cities and the Internet of Things,” in *Management of Engineering and Technology (PICMET), 2015 Portland International Conference on*, pp. 485–494, Aug 2015.
- [2] D. Miorandi, S. Sicari, F. D. Pellegrini, and I. Chlamtac, “Internet of things: Vision, applications and research challenges,” *Ad Hoc Networks*, vol. 10, no. 7, pp. 1497 – 1516, 2012.
- [3] J. A. Stankovic, “Research Directions for the Internet of Things,” *IEEE Internet of Things Journal*, vol. 1, pp. 3–9, Feb 2014.
- [4] J. Gubbi, R. Buyya, S. Marusic, and M. Palaniswami, “Internet of Things (IoT): A vision, architectural elements, and future directions ,” *Future Generation Computer Systems* , vol. 29, no. 7, pp. 1645 – 1660, 2013.
- [5] G. Zhou, J. A. Stankovic, and S. H. Son, “Crowded Spectrum in Wireless Sensor Networks,” *IEEE EmNets*, vol. 6, 2006.
- [6] J. Ren, Y. Zhang, N. Zhang, D. Zhang, and X. Shen, “Dynamic Channel Access to Improve Energy Efficiency in Cognitive Radio Sensor Networks,” *IEEE Transactions on Wireless Communications*, vol. 15, pp. 3143–3156, May 2016.
- [7] M. H. Islam, C. L. Koh, S. W. Oh, X. Qing, Y. Y. Lai, C. Wang, Y. C. Liang, B. E. Toh, F. Chin, G. L. Tan, and W. Toh, “Spectrum Survey in Singapore: Occupancy Measurements and Analyses,” in *2008 3rd International Conference on Cognitive Radio Oriented Wireless Networks and Communications (Crown-Com 2008)*, pp. 1–7, May 2008.
- [8] G. P. Hancke and C. F. Mbuya, “Dynamic Spectrum Allocation for Smart Meter Networks and WSNs in the Presence of Household Consumer Networks,” in *2014 IEEE 23rd International Symposium on Industrial Electronics (ISIE)*, pp. 1459–1462, June 2014.

- [9] J. Zhu, Y. Song, D. Jiang, and H. Song, "Multi-Armed Bandit Channel Access Scheme with Cognitive Radio Technology in Wireless Sensor Networks for the Internet of Things," *IEEE Access*, vol. PP, no. 99, pp. 1–1, 2016.
- [10] R. N. Clarke, "Expanding Mobile Wireless Capacity: The Challenges Presented by Technology and Economics ," *Telecommunications Policy*, vol. 38, no. 89, pp. 693 – 708, 2014. Special issue on Moving Forward with Future Technologies: Opening a Platform for AllSpecial issue on Papers from the 41st Research Conference on Communication, Information and Internet Policy (TPRC 2013).
- [11] B. Raaf, W. Zirwas, K. J. Friederichs, E. Tiirola, M. Laitila, P. Marsch, and R. Wichman, "Vision for beyond 4g broadband radio systems," in *2011 IEEE 22nd International Symposium on Personal, Indoor and Mobile Radio Communications*, pp. 2369–2373, Sept 2011.
- [12] A. Agarwal, G. Misra, and K. Agarwal, "The 5th Generation Mobile Wireless Networks- Key Concepts, Network Architecture and Challenges," *American Journal of Electrical and Electronic Engineering*, vol. 3, no. 2, pp. 22–28, 2015.
- [13] Ofcom, "TV white spaces: approach to coexistence." [online], available: <http://stakeholders.ofcom.org.uk/binaries/consultations/white-space-coexistence/summary/white-spaces.pdf>, September 2013. [accessed 28 May 2014].
- [14] I. Nasr, R. Jungmaier, A. Baheti, D. Noppeney, J. S. Bal, M. Wojnowski, E. Karagozler, H. Raja, J. Lien, I. Poupyrev, and S. Trotta, "A Highly Integrated 60 GHz 6-Channel Transceiver With Antenna in Package for Smart Sensing and Short-Range Communications," *IEEE Journal of Solid-State Circuits*, vol. PP, no. 99, pp. 1–11, 2016.
- [15] K. S. Yang, S. T. Choi, Y. H. Kim, S. Nishi, S. Shimizu, and K. Tokuda, "60 GHz Highly Integrated Small Mobile Terminal for Radio-on-Fibre Millimetre-wave Communication System," *Electronics Letters*, vol. 40, pp. 1456–1457, Oct 2004.
- [16] D. M. Britz, "Wireless big data are our wireless edge networks ready?," in *2014 39th International Conference on Infrared, Millimeter, and Terahertz waves (IRMMW-THz)*, pp. 1–4, Sept 2014.

- [17] I. Hosako, N. Sekine, M. Patrashin, S. Saito, K. Fukunaga, Y. Kasai, P. Baron, T. Seta, J. Mendrok, S. Ochiai, and H. Yasuda, “At the Dawn of a New Era in Terahertz Technology,” *Proceedings of the IEEE*, vol. 95, pp. 1611–1623, Aug 2007.
- [18] G. Wu, S. Talwar, K. Johnsson, N. Himayat, and K. D. Johnson, “M2M: From Mobile to Embedded Internet,” *IEEE Communications Magazine*, vol. 49, pp. 36–43, April 2011.
- [19] L. Tan and N. Wang, “Future Internet: The Internet of Things,” in *Advanced Computer Theory and Engineering (ICACTE), 2010 3rd International Conference on*, vol. 5, pp. V5–376–V5–380, Aug 2010.
- [20] J. Virtanen, J. Virkki, L. Ukkonen, and L. Sydanheimo, “Inkjet-Printed UHF RFID Tags on Renewable Materials,” *Advances in Internet of Things*, 2012.
- [21] M. Mäntysalo and P. Mansikkamäki, “An inkjet-deposited antenna for 2.4 GHz applications,” *AEU - International Journal of Electronics and Communications*, vol. 63, no. 1, pp. 31 – 35, 2009.
- [22] J. C. Batchelor, E. A. Parker, J. A. Miller, V. Sanchez-Romaguera, and S. G. Yeates, “Inkjet printing of frequency selective surfaces,” *Electronics Letters*, vol. 45, pp. 7–8, January 2009.
- [23] D. Redinger, S. Molesa, S. Yin, R. Farschi, and V. Subramanian, “An Ink-Jet-Deposited Passive Component Process for RFID,” *IEEE Transactions on Electron Devices*, vol. 51, pp. 1978–1983, Dec 2004.
- [24] G. Orecchini, F. Alimenti, V. Palazzari, A. Rida, M. M. Tentzeris, and L. Roselli, “Design and fabrication of ultra-low cost radio frequency identification antennas and tags exploiting paper substrates and inkjet printing technology,” *IET Microwaves, Antennas Propagation*, vol. 5, pp. 993–1001, June 2011.
- [25] S. Kim, B. Cook, T. Le, J. Cooper, H. Lee, V. Lakafosis, R. Vyas, R. Moro, M. Bozzi, A. Georgiadis, A. Collado, and M. M. Tentzeris, “Inkjet-Printed Antennas, Sensors and Circuits on Paper Substrate,” *IET Microwaves, Antennas Propagation*, vol. 7, pp. 858–868, July 2013.

- [26] J. Kim, T. Hassinen, W. H. Lee, and S. Ko, “Fully solution-processed organic thin-film transistors by consecutive roll-to-roll gravure printing,” *Organic Electronics*, vol. 42, pp. 361 – 366, 2017.
- [27] H. A. D. Nguyen, C. Lee, and K.-H. Shin, “Approach to optimizing printed conductive lines in high-resolution roll-to-roll gravure printing,” *Robotics and Computer-Integrated Manufacturing*, vol. 46, pp. 122 – 129, 2017.
- [28] J. Zhou, T. Ge, E. Ng, and J. S. Chang, “Fully Additive Low-Cost Printed Electronics With Very Low Process Variations,” *IEEE Transactions on Electron Devices*, vol. 63, pp. 793–799, Feb 2016.
- [29] S. Merilampi, T. Bjrninen, L. Ukkonen, P. Ruuskanen, and L. Sydnheimo, “Embedded Wireless Strain Sensors Based on Printed RFID Tag,” *Sensor Review*, vol. 31, no. 1, pp. 32–40, 2011.
- [30] J. B. Liu, J. Chen, L. F. Zhu, J. C. She, S. Z. Deng, and N. S. Xu, “Conductivity of Screen-Printed Carbon Nanotube Composite Film and its Sensitivity to Organic Gas,” in *2008 2nd IEEE International Nanoelectronics Conference*, pp. 248–251, March 2008.
- [31] T. Kürner and S. Priebe, “Towards THz Communications - Status in Research, Standardization and Regulation,” *Journal of Infrared, Millimeter, and Terahertz Waves*, vol. 35, no. 1, pp. 53–62, 2014.
- [32] R. Appleby and H. B. Wallace, “Standoff Detection of Weapons and Contraband in the 100 GHz to 1 THz Region,” *IEEE Transactions on Antennas and Propagation*, vol. 55, pp. 2944–2956, Nov 2007.
- [33] H. Claussen, L. T. W. Ho, and L. G. Samuel, “Financial Analysis of a Pico-Cellular Home Network Deployment,” in *2007 IEEE International Conference on Communications*, pp. 5604–5609, June 2007.
- [34] I. F. Akyildiz, J. M. Jornet, and C. Han, “Terahertz Band: Next Frontier for Wireless Communications ,” *Physical Communication*, vol. 12, pp. 16 – 32, 2014.
- [35] Y. Yoshimizu, S. Hisatake, S. Kuwano, J. Terada, N. Yoshimoto, and T. Nagatsuma, “Generation of Coherent Sub-terahertz Carrier with Phase Stabilization for Wireless Communications,” *Journal of Communications and Networks*, vol. 15, pp. 569–575, Dec 2013.

- [36] T. Kurner, D. M. Britz, and T. Nagatsuma, “Special Issue on THz Communications,” *Journal of Communications and Networks*, vol. 15, pp. 543–546, Dec 2013.
- [37] M. Asada, S. Suzuki, and N. Kishimoto, “Resonant Tunneling Diodes for Sub-Terahertz and Terahertz Oscillators,” *Japanese Journal of Applied Physics*, vol. 47, no. 6R, p. 4375, 2008.
- [38] A. Suminokura, K. Tsuruda, T. Mukai, M. Fujita, and T. Nagatsuma, “Integration of Resonant Tunneling Diode with Terahertz Photonic-Crystal Waveguide and its Application to Gigabit Terahertz-wave communications,” in *Microwave Photonics (MWP) and the 2014 9th Asia-Pacific Microwave Photonics Conference (APMP), 2014 International Topical Meeting on*, pp. 419–422, Oct 2014.
- [39] A. Shahvarpour, A. Alvarez Melcon, and C. Caloz, “Radiation Efficiency Issues in Planar Antennas on Electrically Thick Substrates and Solutions,” *Antennas and Propagation, IEEE Transactions on*, vol. 61, pp. 4013–4025, Aug 2013.
- [40] “IEEE Standard for Definitions of Terms for Antennas,” *IEEE Std 145-2013 (Revision of IEEE Std 145-1993)*, pp. 1–50, March 2014.
- [41] W. L. Stutzman and G. A. Thiele, *Antenna Theory and Design*. John Wiley and Sons, Inc., third ed., 2012.
- [42] M. H. Ho, C. C. Chiu, and S. H. Liao, “Optimisation of channel capacity for multiple-input multiple-output smart antenna using a particle swarm optimiser,” *IET Communications*, vol. 6, pp. 2645–2653, November 2012.
- [43] S. Bowers and A. Hajimiri, “Multi-Port Driven Radiators,” *Microwave Theory and Techniques, IEEE Transactions on*, vol. 61, pp. 4428–4441, Dec 2013.
- [44] S. Bowers, A. Safaripour, and A. Hajimiri, “An integrated traveling-wave slot radiator,” in *Radio Frequency Integrated Circuits Symposium, 2014 IEEE*, pp. 369–372, June 2014.
- [45] A. Russo, B. Y. Ahn, J. J. Adams, E. B. Duoss, J. T. Bernhard, and J. A. Lewis, “Pen-on-Paper Flexible Electronics,” *Advanced Materials*, vol. 23, no. 30, pp. 3426–3430, 2011.
- [46] F. C. Krebs, “Fabrication and Processing of Polymer Solar Cells: A Review of Printing and Coating Techniques,” *Solar Energy Materials and Solar Cells*,

- vol. 93, no. 4, pp. 394 – 412, 2009. Processing and Preparation of Polymer and Organic Solar Cells.
- [47] S. H. Ko, H. Pan, C. P. Grigoropoulos, C. K. Luscombe, J. M. J. Frchet, and D. Poulikakos, “All-Inkjet-Printed Flexible Electronics Fabrication on a Polymer Substrate by Low-Temperature High-Resolution Selective Laser Sintering of Metal Nanoparticles,” *Nanotechnology*, vol. 18, no. 34, p. 345202, 2007.
- [48] F. Alimenti, P. Mezzanotte, M. Dionigi, M. Virili, and L. Roselli, “Microwave Circuits in Paper Substrates Exploiting Conductive Adhesive Tapes,” *IEEE Microwave and Wireless Components Letters*, vol. 22, pp. 660–662, Dec 2012.
- [49] A. Rashidian, L. Shafai, M. Sobocinski, J. Perntie, J. Juuti, and H. Jantunen, “Printable Planar Dielectric Antennas,” *IEEE Transactions on Antennas and Propagation*, vol. 64, pp. 403–413, Feb 2016.
- [50] D. Zhang, W. Hu, C. Meggs, B. Su, T. Price, D. Iddles, M. J. Lancaster, and T. W. Button, “Fabrication and Characterisation of Barium Strontium Titanate Thick Film Device Structures for Microwave Applications,” *Journal of the European Ceramic Society*, vol. 27, no. 2, pp. 1047–1051, 2007.
- [51] S. Khan, L. Lorenzelli, and R. S. Dahiya, “Technologies for Printing Sensors and Electronics Over Large Flexible Substrates: A Review,” *IEEE Sensors Journal*, vol. 15, pp. 3164–3185, June 2015.
- [52] “Inkjet Printing Process for Kesterite Solar Cells.” [online], available:<http://www.sciencenewsline.com/news/2015050616470015.html>, May 2015. [accessed 01 November 2016].
- [53] D. Sung, A. de la Fuente Vornbrock, and V. Subramanian, “Scaling and Optimization of Gravure-Printed Silver Nanoparticle Lines for Printed Electronics,” *IEEE Transactions on Components and Packaging Technologies*, vol. 33, pp. 105–114, March 2010.
- [54] C. O. Phillips, D. G. Beynon, S. M. Hamblyn, G. R. Davies, D. T. Gethin, and T. C. Claypole, “A Study of the Abrasion of Squeegees Used in Screen Printing and Its Effect on Performance with Application in Printed Electronics,” *Coatings*, vol. 4, no. 2, p. 356, 2014.

- [55] “Thermal Transitions of Homopolymers: Glass Transition and Melting Point.” [online], <https://www.scribd.com/document/60272576/Thermal-Transitions-of-Homo-Polymers>. [26 October 2016].
- [56] S. Wunscher, R. Abbel, J. Perelaer, and U. S. Schubert, “Progress of Alternative Sintering Approaches of Inkjet-printed Metal Inks and their Application for Manufacturing of Flexible Electronic Devices,” *J. Mater. Chem. C*, vol. 2, pp. 10232–10261, 2014.
- [57] R. Todd, E. Zapata-Solvas, R. Bonilla, T. Sneddon, and P. Wilshaw, “Electrical Characteristics of Flash Sintering: Thermal Runaway of Joule Heating,” *Journal of the European Ceramic Society*, vol. 35, no. 6, pp. 1865 – 1877, 2015.
- [58] B. J. Perelaer, A. W. M. de Laat, C. E. Hendriks, and U. S. Schubert, “Inkjet-Printed Silver Tracks: Low Temperature Curing and Thermal Stability Investigation,” *J. Mater. Chem.*, vol. 18, pp. 3209–3215, 2008.
- [59] “Thermal Printheads.” [online], available: <http://global.kyocera.com/prdct/printing-devices/thermal-printheads/pdf/kctph201402.pdf>. [accessed 26 July 2016].
- [60] SPF-INC, “Conductive Thermal Transfer Ribbons for Printed Electronics and RFID Antennas .” [accessed 01 January 2017].
- [61] M. Kgwadi, M. Rizwan, A. A. Kutty, J. Virkki, L. Ukkonnen, and T. D. Drysdale, “Performance Comparison of Inkjet and Thermal Transfer Printed UHF RFID Tags,” *IET Microwave Antennas and Propagation*, accepted 21 June 2016.
- [62] J. G. Andrews, S. Buzzi, W. Choi, S. V. Hanly, A. Lozano, A. C. K. Soong, and J. C. Zhang, “What Will 5G Be?,” *IEEE Journal on Selected Areas in Communications*, vol. 32, pp. 1065–1082, June 2014.
- [63] T. S. Rappaport, S. Sun, R. Mayzus, H. Zhao, Y. Azar, K. Wang, G. N. Wong, J. K. Schulz, M. Samimi, and F. Gutierrez, “Millimeter Wave Mobile Communications for 5G Cellular: It Will Work!,” *IEEE Access*, vol. 1, pp. 335–349, 2013.
- [64] “Nomenclature of the Frequency and Wavelength Bands used in Telecommunications.” [online], https://www.itu.int/dms_pubrec/itu-r/rec/v/R-REC-V.431-8-201508-I!!PDF-E.pdf, August 2015. [accessed 01 November 2016].

- [65] “IEEE Standard Letter Designations for Radar-Frequency Bands,” *IEEE Std 521-2002 (Revision of IEEE Std 521-1984)*, pp. 1–3, 2003.
- [66] P. H. Siegel, “Terahertz Technology,” *IEEE Transactions on Microwave Theory and Techniques*, vol. 50, pp. 910–928, Mar 2002.
- [67] Z. Pi and F. Khan, “An Introduction to Millimeter-wave Mobile Broadband Systems,” *IEEE Communications Magazine*, vol. 49, pp. 101–107, June 2011.
- [68] S. Rangan, T. S. Rappaport, and E. Erkip, “Millimeter-wave cellular wireless networks: Potentials and challenges,” *Proceedings of the IEEE*, vol. 102, pp. 366–385, March 2014.
- [69] H. Li, L. Huang, and Y. Wang, “Scheduling schemes for interference suppression in millimeter-wave cellular network,” in *Personal, Indoor, and Mobile Radio Communications (PIMRC), 2015 IEEE 26th Annual International Symposium on*, pp. 2244–2248, Aug 2015.
- [70] J. Ruoskanen, P. Eskelinen, and H. Heikkila, “Millimeter wave radar with clutter measurements,” *IEEE Aerospace and Electronic Systems Magazine*, vol. 18, pp. 19–23, Oct 2003.
- [71] R. Appleby and R. N. Anderton, “Millimeter-wave and submillimeter-wave imaging for security and surveillance,” *Proceedings of the IEEE*, vol. 95, pp. 1683–1690, Aug 2007.
- [72] C. Wang and H. M. Wang, “Physical layer security in millimeter wave cellular networks,” *IEEE Transactions on Wireless Communications*, vol. 15, pp. 5569–5585, Aug 2016.
- [73] J. Wells, “Faster than Fiber: The Future of Multi-G/s Wireless,” *IEEE Microwave Magazine*, vol. 10, pp. 104–112, May 2009.
- [74] V. Tralli, A. Vaccari, R. Verdone, and O. Andrisano, “Adaptive time and frequency resource assignment with cofdm for lmds systems,” *IEEE Transactions on Communications*, vol. 49, pp. 235–238, Feb 2001.
- [75] A. Ghosh, T. A. Thomas, M. C. Cudak, R. Ratasuk, P. Moorut, F. W. Vook, T. S. Rappaport, G. R. MacCartney, S. Sun, and S. Nie, “Millimeter-wave enhanced local area systems: A high-data-rate approach for future wireless networks,” *IEEE Journal on Selected Areas in Communications*, vol. 32, pp. 1152–1163, June 2014.

- [76] L. Verma, M. Fakharzadeh, and S. Choi, “Backhaul Need for Speed: 60 GHz is the Solution,” *IEEE Wireless Communications*, vol. 22, pp. 114–121, December 2015.
- [77] H. Eisele, “State of the Art and Future of Electronic Sources at Terahertz Frequencies,” *Electronics Letters*, vol. 46, pp. s8–s11, December 2010.
- [78] J. Wang, L. Wang, C. Li, B. Romeira, and E. Wasige, “28 GHz MMIC Resonant Tunnelling Diode Oscillator of around 1mW Output Power,” *Electronics Letters*, vol. 49, pp. 816–818, June 2013.
- [79] J. Wang, L. Wang, C. Li, K. Alharbi, A. Khalid, and E. Wasige, “W-band InP-based Resonant Tunnelling Diode Oscillator with Milliwatt Output Power,” in *26th International Conference on Indium Phosphide and Related Materials (IPRM)*, pp. 1–2, May 2014.
- [80] J. Wang, A. Khalidi, K. Alharbi, A. Ofiare, H. Zhou, and E. Wasige, “G-Band MMIC Resonant Tunneling Diode Oscillators,” in *2016 Compound Semiconductor Week (CSW) [Includes 28th International Conference on Indium Phosphide Related Materials (IPRM) 43rd International Symposium on Compound Semiconductors (ISCS)*, pp. 1–2, June 2016.
- [81] S. Suzuki, M. Asada, A. Teranishi, H. Sugiyama, and H. Yokoyama, “Fundamental Oscillation of Resonant Tunneling Diodes above 1 THz at Room Temperature,” *Applied Physics Letters*, vol. 97, no. 24, pp. –, 2010.
- [82] K. H. Alharbi, *High Performance Terahertz Resonant Tunnelling Diode Sources and Broadband Antenna for Air-side Radiation*. PhD thesis, School of Engineering, University of Glasgow, 2016.
- [83] J. Lee, J. Lee, and K. Yang, “An On-Off Mode RTD Oscillator Operating at Extremely Low Power Consumption,” *IEEE Transactions on Nanotechnology*, vol. 11, pp. 863–865, Sept 2012.
- [84] K. Urayama, S. Aoki, S. Suzuki, M. Asada, H. Sugiyama, and H. Yokoyama, “Sub-terahertz resonant tunneling diode oscillators integrated with tapered slot antennas for horizontal radiation,” *Applied Physics Express*, vol. 2, no. 4, p. 044501, 2009.

- [85] K. Okada, S. Suzuki, and M. Asada, “Resonant-tunneling-diodeterahertz oscillator integrated with slot-coupled patch antenna,” in *26th International Conference on Indium Phosphide and Related Materials (IPRM)*, pp. 1–2, May 2014.
- [86] K. H. Alharbi, A. Khalid, A. Ofiare, J. Wang, and E. Wasige, “Diced and grounded broadband bow-tie antenna with tuning stub for resonant tunnelling diode terahertz oscillators,” in *IET Colloquium on Millimetre-Wave and Terahertz Engineering Technology 2016*, pp. 1–4, March 2016.
- [87] M. Reddy, S. C. Martin, A. C. Molnar, R. E. Muller, R. P. Smith, P. H. Siegel, M. J. Mondry, M. J. W. Rodwell, H. Kroemer, and S. J. Allen, “Monolithic schottky-collector resonant tunnel diode oscillator arrays to 650 ghz,” *IEEE Electron Device Letters*, vol. 18, pp. 218–221, May 1997.
- [88] J. Li, Y. Li, W. Shi, H. Jiang, and L. Mao, “Two-Element Tapered Slot Antenna Array for Terahertz Resonant Tunneling Diode Oscillators,” *International Journal of Antennas and Propagation*, vol. 2014, 2014.
- [89] A. Taflove and S. C. Hagness, *Computational Electrodynamics: The Finite-Difference Time-Domain Method*. Artech House, third ed., 2005.
- [90] K. Yee, “Numerical Solution of Initial Boundary Value Problems Involving Maxwell’s Equations in Isotropic Media,” *IEEE Transactions on Antennas and Propagation*, vol. 14, pp. 302–307, May 1966.
- [91] T. Liebig, A. Rennings, S. Held, and D. Erni, “openems a free and open source equivalent-circuit (ec) fdtd simulation platform supporting cylindrical coordinates suitable for the analysis of traveling wave mri applications,” *International Journal of Numerical Modelling: Electronic Networks, Devices and Fields*, vol. 26, no. 6, pp. 680–696, 2013.
- [92] Y. Wang and A. M. Abbosh, “Human head modelling at microwave frequencies using open-source electromagnetics solver,” in *2015 International Symposium on Antennas and Propagation (ISAP)*, pp. 1–2, Nov 2015.
- [93] Y. Zhang, M. H. Negm, and M. H. Bakr, “An adjoint variable method for wideband second-order sensitivity analysis through fdtd,” *IEEE Transactions on Antennas and Propagation*, vol. 64, pp. 675–686, Feb 2016.

- [94] J.-P. Berenger, "A Perfectly Matched Layer for the Absorption of Electromagnetic Waves," *Journal of Computational Physics*, vol. 114, no. 2, pp. 185–200, 1994.
- [95] D. S. Katz, E. T. Thiele, and A. Taflove, "Validation and Extension to Three Dimensions of the Berenger PML absorbing boundary condition for FD-TD meshes," *IEEE Microwave and Guided Wave Letters*, vol. 4, pp. 268–270, Aug 1994.
- [96] T. Liebig, "OpenEMS - Open Electromagnetic Field Solver."
- [97] G. Whyte, D. Harrison, D. Cumming, and T. Drysdale, "Direct printing of flexible metallic millimetre-wave frequency selective surfaces," in *Antennas and Propagation Society International Symposium (APSURSI), 2010 IEEE*, pp. 1–4, July 2010.
- [98] "Microwave Absorber Selection Guide." [online], available: www.ets-lindgren.com/pdf/absorber.pdf. [accessed 28 March 2016].
- [99] V. Timoshevskii, Y. Ke, H. Guo, and D. Gall, "The influence of surface roughness on electrical conductance of thin cu films: An ab initio study," *Journal of Applied Physics*, vol. 103, no. 11, 2008.
- [100] B. Curran, I. Ndip, S. Guttowski, and H. Reichl, "A Methodology for Combined Modeling of Skin, Proximity, Edge, and Surface Roughness Effects," *IEEE Transactions on Microwave Theory and Techniques*, vol. 58, pp. 2448–2455, Sept 2010.
- [101] "Harima NPS-JL silver nanoparticle ink." [online], available: <http://www.harima.co.jp/en/products/electronics/pdf/brochure14e.21.pdf>. [accessed 26 July 2016].
- [102] Y. Ren, J. Virkki, L. Sydänheimo, and L. Ukkonen, "Optimisation of manufacturing parameters for inkjet-printed and photonicly sintered metallic nanoparticle UHF RFID tags," *Electronics Letters*, vol. 50, pp. 1504–1505, October 2014.
- [103] J. F. Salmerón, F. Molina-Lopez, D. Briand, J. J. Ruan, A. Rivadeneyra, M. A. Carvajal, L. F. Capitán-Vallvey, N. F. de Rooij, and A. J. Palma, "Properties and Printability of Inkjet and Screen-Printed Silver Patterns for RFID Antennas," *Journal of Electronic Materials*, vol. 43, no. 2, pp. 604–617, 2014.

- [104] “ETSI TR 101 445 v1.1.1 (2002-04).” [online], available: http://www.etsi.org/deliver/etsi_tr/101400_101499/101445/01.01.01.60/tr_101445v010101p.pdf. [accessed 14 February 2016].
- [105] T. Björninen, L. Sydänheimo, and L. Ukkonen, “Development and Validation of an Equivalent Circuit Model for UHF RFID IC Based on Wireless Tag Measurements,” in *Proceedings of the 34th Annual Symposium of the Antenna Measurement Techniques Association AMTA 2012, October 21-26, Bellevue, WA, USA*, pp. 480–485, 2012.
- [106] M. Kgwadi, C. Vourch, D. Harrison, and T. Drysdale, “On-demand Printing of Antennas for TV White-Space Communications,” in *2014 Loughborough Antennas and Propagation Conference (LAPC) (LAPC 2014)*, pp. 553–556, nov 2014.
- [107] Ofcom, “Tv white spaces.” [online], available: stakeholders.ofcom.org.uk/spectrum/tv-white-spaces. [accessed] 6 June 2014.
- [108] C. Holloway and E. F. Kuester, “A Quasi-Closed Form Expression for the Conductor Loss of CPW Lines, With an Investigation of Edge Shape Effects,” *Microwave Theory and Techniques, IEEE Transactions on*, vol. 43, pp. 2695–2701, Dec 1995.
- [109] T. Fukusako, K. Ide, and S. Ijiguchi, “Gain Enhancement of Low-profile, Electrically Small Capacitive-fed Antennas Using Stacked Meander Lines,” in *Communications, Circuits and Systems (ICCCAS), 2010 International Conference on*, pp. 636–641, July 2010.
- [110] M. Kgwadi and T. D. Drysdale, “Diode-switched thermal-transfer printed antenna on flexible substrate,” *Electronics Letters*, vol. 52, no. 4, pp. 258–260, 2016.
- [111] A. Austin, M. Neve, G. Rowe, and R. Pirkl, “Modeling the Effects of Nearby Buildings on Inter-Floor Radio-Wave Propagation,” *Antennas and Propagation, IEEE Transactions on*, vol. 57, pp. 2155–2161, July 2009.
- [112] M. S. Alam and A. Abbosh, “Planar Pattern Reconfigurable Antenna with Eight Switchable Beams for WiMax and WLAN Applications,” *IET Microwaves, Antennas Propagation*, vol. 10, no. 10, pp. 1030–1035, 2016.

- [113] C. Christodoulou, L. Feldner, V. Zachou, and D. Anagnostou, “Planar reconfigurable antennas,” in *Antennas and Propagation, 2006. EuCAP 2006. First European Conference on*, pp. 1–7, Nov 2006.
- [114] Y. Cao, S. Cheung, and T. Yuk, “A Simple Planar Polarization Reconfigurable Monopole Antenna for GNSS/PCS,” *Antennas and Propagation, IEEE Transactions on*, vol. 63, pp. 500–507, Feb 2015.
- [115] N. Kingsley, D. Anagnostou, M. Tentzeris, and J. Papapolymerou, “RF MEMS Sequentially Reconfigurable Sierpinski Antenna on a Flexible Organic Substrate With Novel DC-Biasing Technique,” *Microelectromechanical Systems, Journal of*, vol. 16, pp. 1185–1192, Oct 2007.
- [116] “BAP50-03 General Purpose PIN Diode - Product data sheet.”
- [117] G. R. Aiello and G. D. Rogerson, “Ultra-wideband wireless systems,” *IEEE Microwave Magazine*, vol. 4, pp. 36–47, June 2003.
- [118] M. K. Chowdhury and C. Bose, “M-psk mb-ofdm ultra wideband communication system performance for 4g high-rate ieee 802.15.3a wireless personal area networks,” in *International Conference on Next Generation Networks*, pp. 1–6, Sept 2010.
- [119] “Revision of Part 15 of the Commission’s Rules Regarding Ultra-Wideband Transmission Systems.” [accessed 4 January 2017].
- [120] D. S. Kumar, I. S. Hinduja, V. V. Mani, and R. Bose, “Beamforming of ultra wideband signals in an ieee 802.15.3a channel environment,” in *2014 IEEE International Conference on Ultra-WideBand (ICUWB)*, pp. 41–46, Sept 2014.
- [121] H. U. Li and T. N. Jackson, “Flexibility testing strategies and apparatus for flexible electronics,” *IEEE Transactions on Electron Devices*, vol. 63, pp. 1934–1939, May 2016.
- [122] G. Shaker, S. Safavi-Naeini, N. Sangary, and M. Tentzeris, “Inkjet printing of ultrawideband (uwb) antennas on paper-based substrates,” *Antennas and Wireless Propagation Letters, IEEE*, vol. 10, pp. 111–114, 2011.
- [123] M. Kgwadi, K. Alharbi, J. Wang, and E. Wasige, “Slot-ring multiport driven antenna with improved airside radiation for terahertz communications,” in *2016 46th European Microwave Conference (EuMC)*, pp. 1247–1250, Oct 2016.

- [124] W. Chew, "A broad-band annular-ring microstrip antenna," *IEEE Transactions on Antennas and Propagation*, vol. 30, pp. 918–922, September 1982.
- [125] J. Dahele, K. Lee, and D. Wong, "Dual-frequency stacked annular-ring microstrip antenna," *IEEE Transactions on Antennas and Propagation*, vol. 35, pp. 1281–1285, Nov 1987.
- [126] S. Ali, W. Chew, and J. Kong, "Vector hankel transform analysis of annular-ring microstrip antenna," *IEEE Transactions on Antennas and Propagation*, vol. 30, pp. 637–644, July 1982.
- [127] J. C. Batchelor and R. J. Langley, "Microstrip ring antennas operating at higher order modes for mobile communications," *IEE Proceedings - Microwaves, Antennas and Propagation*, vol. 142, pp. 151–155, Apr 1995.
- [128] S. Raman and G. M. Rebeiz, "Single- and dual-polarized millimeter-wave slot-ring antennas," *IEEE Transactions on Antennas and Propagation*, vol. 44, pp. 1438–1444, Nov 1996.
- [129] C. E. Tong and R. Blundell, "An annular slot antenna on a dielectric half-space," *IEEE Transactions on Antennas and Propagation*, vol. 42, pp. 967–974, Jul 1994.
- [130] A. Ofiare, J. Wang, K. Alharbi, A. Khalid, E. Wasige, and L. Wang, "Novel tunnel diode oscillator power combining circuit topology based on synchronisation," in *2015 Asia-Pacific Microwave Conference (APMC)*, vol. 3, pp. 1–3, Dec 2015.
- [131] J. Wang, *Monolithic Microwave/Millimetrewave Integrated Circuit Resonant Tunnelling Diode Sources with around a Milliwatt Output Power*. PhD thesis, School of Engineering, University of Glasgow, 2013.
- [132] Viginia Diodes, Inc., 979 Second Street SE, Suite 309 Charlottesville, VA 22902-6172 (USA), *Zero-Bias Detector Operational Manual*, November 2016.
- [133] M. Rizwan, A. A. Kuttty, M. Kgwadi, T. D. Drysdale, L. Sydanheimo, L. Ukkonen, and J. Virkki, "Possibilities of fabricating copper-based rfid tags with photonic-sintered inkjet printing and thermal transfer printing," *IEEE Antennas and Wireless Propagation Letters*, vol. PP, no. 99, pp. 1–1, 2017.

- [134] J. Lee, J. Park, H. Jeong, K.-H. Shin, and D. Lee, “Optimization of printing conditions for microscale multiline printing in continuous roll-to-roll gravure printing,” *Journal of Industrial and Engineering Chemistry*, vol. 42, pp. 131 – 141, 2016.
- [135] W. G. Whittow, A. Chauraya, J. C. Vardaxoglou, Y. Li, R. Torah, K. Yang, S. Beeby, and J. Tudor, “Inkjet-printed microstrip patch antennas realized on textile for wearable applications,” *IEEE Antennas and Wireless Propagation Letters*, vol. 13, pp. 71–74, 2014.